

## INFORMATION TO USERS

This manuscript has been reproduced from the microfilm master. UMI films the text directly from the original or copy submitted. Thus, some thesis and dissertation copies are in typewriter face, while others may be from any type of computer printer.

**The quality of this reproduction is dependent upon the quality of the copy submitted.** Broken or indistinct print, colored or poor quality illustrations and photographs, print bleedthrough, substandard margins, and improper alignment can adversely affect reproduction.

In the unlikely event that the author did not send UMI a complete manuscript and there are missing pages, these will be noted. Also, if unauthorized copyright material had to be removed, a note will indicate the deletion.

Oversize materials (e.g., maps, drawings, charts) are reproduced by sectioning the original, beginning at the upper left-hand corner and continuing from left to right in equal sections with small overlaps. Each original is also photographed in one exposure and is included in reduced form at the back of the book.

Photographs included in the original manuscript have been reproduced xerographically in this copy. Higher quality 6" x 9" black and white photographic prints are available for any photographs or illustrations appearing in this copy for an additional charge. Contact UMI directly to order.

# U·M·I

University Microfilms International  
A Bell & Howell Information Company  
300 North Zeeb Road, Ann Arbor, MI 48106-1346 USA  
313/761-4700 800/521-0600



**Order Number 9312216**

**The morphologies of distant radio galaxies**

**Rigler, Michael Anthony, Ph.D.**

**University of Hawaii, 1992**

**U·M·I**  
300 N. Zeeb Rd.  
Ann Arbor, MI 48106



**THE MORPHOLOGIES OF DISTANT RADIO GALAXIES**

A DISSERTATION SUBMITTED TO THE GRADUATE DIVISION OF THE  
UNIVERSITY OF HAWAII IN PARTIAL FULFILLMENT OF THE  
REQUIREMENTS FOR THE DEGREE OF

DOCTOR OF PHILOSOPHY

IN

ASTRONOMY

DECEMBER 1992

By

Michael Anthony Rigler

Dissertation Committee:

Simon J. Lilly, Chairperson  
Lennox L. Cowie  
Ann M. Boesgaard  
Alan S. Stockton  
Xerxes Tata

## ACKNOWLEDGEMENTS

This dissertation is dedicated with aloha to my parents, John and Marilyn, and to my sister, Lorry, who have continuously sent me their love and support from across the ocean.

For past three years, my greatest source of inspiration has been my advisor, Simon Lilly. From the day I first stepped into his office he has shown me a seemingly boundless supply of patience and encouragement. Simon excels as a teacher, both because he is highly enthusiastic about his work, and because he carries a deep sense of his duty to the next generation. In his presence, a student is continually reminded of the depth and glory of our profession. It has been a pleasure for this student to work closely with him and watch his keen mind in action.

I have also benefited greatly from my association with the other members of my dissertation committee. Len Cowie and Alan Stockton have contributed greatly to my scientific development, and have also assisted me in obtaining support during the lean times. Esther deserves special thanks for kindly agreeing to serve as a proxy on my committee. Finally, I must extend my warmest thanks to Ann Boesgaard for serving as my guardian angel through thick and thin.

Before I began work on my dissertation, I had the good fortune to work with three other IFA faculty members who taught me very useful skills. Dale Cruikshank gave me my first lessons on the use of the UH 2.2 m and CCD cameras for imaging, Eric Becklin taught me how to use the IRTF, and Gareth Wynn-Williams allowed me to participate in his work with IRAS galaxy data. I wish the best of luck to these three astronomers and to their families.

For me, the most exciting part of my graduate career has been observing at the Mauna Kea summit. I particularly enjoy using the UH 2.2 m, which has simply the finest telescope operators, Dave Woodworth and Frank Cheigh, and the most outstanding day crew to be found. These people have gone way beyond the call for me on several occasions when I was experiencing some problem, and they always got things fixed. They're also a fun bunch to hang out with.

My best friends for the past six years have been my fellow students: Jon Gardner, James Annis, Matt Penn and Dave Wall. Sharing the grad school experience with these guys made it almost fun, and I'm not sure I could have done it without them. There are many other IFA students I'm proud to have known, including Joe Piscitelli, Aaron Evans, Jim Deane, Susan Ridgway, Kevin Jim, Gary Hill, Mike Pierce, Russ Lavery, Ed Rosenthal, Doug Simons, Ken Gayley, Mike Ressler, Hua Chen, Jane Luu and Rob Ronan. I wish all of the IFA students, past, present and future, the best of luck in their lives and careers. Many of the IFA postdocs also contributed to my enjoyment of life. We were fortunate to experience an influx of interesting postdocs and young faculty from the UK, who were the driving force behind many organized activities including the underwater excursions of HUAC, the Czar's volleyball, and the soccer matches.

There are two staff members who deserve recognition for their effort to brighten my existence at the IFA: George Miyashiro and Georgette Albert. George kept the computers in top form and saved my bacon more times than I can remember. He also made great strides toward improving the working environment, so that today IFA is a better place for a student to live. Georgette Albert is a

secretary beyond compare, being only person I've ever known who can solve problems as fast as I can generate them. She can also be a good friend when you need one.

Though far from my own family, I was fortunate to be able to enjoy the hospitality of the families of my friends, Nathan Inada and Steve Hawes. I would also like to thank Amy and friends for having me over to Kauai often. My warmest sense of ohana came from living at the Akalani house with Ken and Kathy Beal, Andrew Murboch, Matt Medeiros, and Ikaika. Of all of the friends I have made in the islands, I believe I will miss my Akalani house mates the most.

My sole enduring hobby throughout grad school was the wonderful sport of ultimate. I would like to thank all of the players in the Hawaiian Ultimate League Association for the many enriching experiences we shared. Captain Ken Gayley deserves recognition for uplifting our team, the Hulaguns, to the level of mainland tournament competition. My Hawaiian experience was made complete by the outer-island excursions I took with team mates Doug Bergerson, Fred Ballerini and Grant Wise, otherwise known as "Team Haleakala." I'm confident that we will not soon forget the elusive ten foot tiger shark of the Na Pali coast, or the savage feral pigs of Waimanu Valley. Finally, I offer my deepest thanks to Dr. Uhr and the orthopedic staff at Kaiser for putting me back together time and again.

## ABSTRACT

Multicolor line and continuum images of a complete sample of 13 3C radio galaxies at  $0.8 < z < 1.3$ , spanning the range  $2500 \text{ \AA}$  to  $1 \text{ }\mu\text{m}$  in the rest frame, are presented and analyzed. Quantitative analysis of these images shows that the infrared images are less elongated than those at optical wavelengths and show only a much weaker "alignment effect" with the radio source axis. The quadrupole moments show a progressive reduction from short to long wavelengths, as expected if a symmetric component dominates at infrared wavelengths. A spectral decomposition based on these moments suggests that the aligned component probably has a roughly flat spectral energy distribution ( $f_{\nu} \approx 0$  to  $-1$ ) while the symmetric red component that dominates in the infrared probably has a spectral energy distribution similar to that of a gE galaxy. In two cases where the aligned component is detached from the main galaxy, the spectral energy distribution is directly measured within small apertures and found to have  $f_{\nu} \approx -1$ . In typical 3C galaxies at  $z \approx 1$ , the active aligned component contributes 10% of the infrared light. While more active objects have a larger contamination, these generally modest components are insufficient to perturb significantly either the scatter in, or the continuity of, the observed  $K-z$  relation. The conventional interpretation of the  $K-z$  diagram in terms of a uniform population of mature host galaxies is thus still likely to be correct, at least at  $z \approx 1$ . As far as can be determined from the data, the scale sizes of the radio galaxy images at infrared wavelengths are consistent with the sizes of the giant ellipticals associated with powerful radio galaxies at low redshift. A model surface fitting analysis of the reddest member of the sample, 3C 65, and of another red galaxy, 3C 437

( $z = 1.480$ ), shows that the infrared surface brightness profiles are well fit by a deVaucouleurs  $r^{1/4}$  law characteristic of giant ellipticals, with characteristic photometric parameters comparable to those of brightest cluster members and low-redshift radio galaxies for standard cosmologies. The small displacement of these galaxies from low-redshift brightest cluster members and radio galaxies on the  $\mu_e - \log r_e$  plane suggests that little or no stellar evolution is required in a cosmology with  $q_0 = 0.5$  ( $\Lambda = 0$ ), while a modest degree of stellar evolution is implied in a model with  $q_0 = 0$  ( $\Lambda = 0$ ), or models with  $\Lambda > 0$ . A non-expanding cosmology would require the high-redshift systems to lie at the extreme end of the distribution of properties of local gE galaxies, and the effects of stellar and/or dynamical evolution would be to make the objects more extreme. Several of these radio galaxies are accompanied by small red companion galaxies that are prominent on our infrared images at random position angles relative to the radio axis. These are interpreted as representing a conventional trigger for the radio sources. There is a preference for these companions to be associated with the bluest, most aligned, and generally most active objects.

## TABLE OF CONTENTS

Acknowledgements .....	iii
Abstract .....	vi
List of Tables .....	xi
List of Figures .....	xii
Chapter 1: Introduction .....	1
References for Chapter 1 .....	13
Chapter 2: Observations and Data Reduction .....	16
2.1 Rationale Behind the Sample Selection .....	16
2.2 Rationale Behind the Proposed Observations .....	17
2.3 Review of the Observations .....	18
2.3.1 Optical Observations .....	18
2.3.2 Infrared Observations .....	19
2.4 Methods of Data Acquisition and Reduction .....	20
2.4.1 Optical Imaging .....	20
2.4.1.1 The Narrow Band Images .....	21
2.4.1.2 Broad Band Imaging .....	23
2.4.2 Infrared Imaging .....	24
2.5 Combining and Displaying the Data .....	30
References for Chapter 2 .....	32
Chapter 3: Morphologies of $z \cong 1$ Radio Galaxies .....	35
3.1 Introduction .....	35
3.2 The Images .....	36
3.3 Qualitative Overview of the Morphologies .....	38
3.4 Quantitative Morphological Analysis .....	39
3.4.1 A Quantitative Measure of Asymmetry .....	40
3.4.1.1 The Galaxy 3C 217 .....	49
3.4.1.2 The Galaxy 3C 267 .....	50
3.4.1.3 The Galaxy 3C 368 .....	50
3.4.1.4 The Galaxy 3C 356 .....	54
3.5 Sizes of the Galaxies .....	56
3.6 Red Companion Galaxies .....	57
3.7 Global Correlations with Color .....	60
3.7.1 The Color-Magnitude Relation .....	61
3.7.2 Elongation as a Function of Color .....	64

3.8 The Aligned Component .....	65
3.9 Summary .....	67
Appendix A: An Improved Infrared Image of 3C 267 .....	70
References for Chapter 3 .....	71
Chapter 4: Surface Photometry of Quiescent Radio Galaxies .....	106
4.1 Preface .....	106
4.2 Abstract .....	106
4.3 Introduction .....	107
4.4 Observations and Reductions .....	108
4.5 Morphological Analysis .....	110
4.5.1 Gross Morphological Features .....	110
4.5.2 Surface Fitting Procedure .....	111
4.6 Discussion .....	113
4.6.1 Quality of Fit of gE Models .....	113
4.6.2 Comparison with Lower Redshift Systems .....	114
4.6.2.1 Stellar Evolution and $q_0$ .....	114
4.6.2.2 Tolman Test for Universal Expansion .....	115
4.7 Conclusions .....	116
References for Chapter 4 .....	118
Chapter 5: Detached Aligned Regions of Emission .....	124
5.1 The Blue Object Near 3C 65 .....	126
5.2 The Detached Aligned Component of 3C 326.1 .....	127
5.3 Conclusions .....	129
References for Chapter 5 .....	131
Chapter 6: Conclusions and Future Work .....	137
6.1 Summary of Results .....	137
6.1.1 Decomposition into Symmetric and Aligned Components .....	137
6.1.2 Spectral Energy Distribution of the Symmetric Component .....	138
6.1.3 Spectral Energy Distribution of the Aligned Component .....	138
6.1.4 Properties of the Most Quiescent Systems .....	139
6.1.5 Detached Aligned Regions of Emission .....	139
6.1.6 Red Companions .....	140
6.2 Future Work .....	140
6.2.1 Extending to Higher Redshifts .....	141
6.2.2 Quiescent Radio Galaxies .....	142

6.2.3 Future Studies of the Alignment Effect .....	144
6.2.4 The Environments of High-Redshift Radio Galaxies .....	145
References for Chapter 6 .....	148

## LIST OF TABLES

Table 2.1: Log of Observations .....	33
Table 3.1: Spectral Energy Distributions .....	73
Table 3.2: Alignment Parameters .....	74
Table 3.3: Moment Analysis .....	75
Table 3.4: Red Companions .....	76
Table 4.1: Surface Photometry .....	120

## LIST OF FIGURES

Figure 1.1: Simulations of superposed morphological components .....	15
Figure 3.1a: Montage of multicolor images for 3C 65 .....	77
Figure 3.1b: Montage of multicolor images for 3C 217 .....	78
Figure 3.1c: Montage of multicolor images for 3C 226 .....	79
Figure 3.1d: Montage of multicolor images for 3C 252 .....	80
Figure 3.1e: Montage of multicolor images for 3C 265 .....	81
Figure 3.1f: Montage of multicolor images for 3C 266 .....	82
Figure 3.1g: Montage of multicolor images for 3C 267 .....	83
Figure 3.1h: Montage of multicolor images for 3C 180 .....	84
Figure 3.1i: Montage of multicolor images for 3C 289 .....	85
Figure 3.1j: Montage of multicolor images for 3C 324 .....	86
Figure 3.1k: Montage of multicolor images for 3C 352 .....	87
Figure 3.1l: Montage of multicolor images for 3C 356 .....	88
Figure 3.1m: Montage of multicolor images for 3C 368 .....	89
Figure 3.2: Comparison of photometry past and present .....	90
Figure 3.3: The alignment effect in the sample .....	91
Figure 3.4a: Spectral energy decomposition of 3C 65 .....	92
Figure 3.4b: Spectral energy decomposition of 3C 265 .....	93
Figure 3.4c: Spectral energy decomposition of 3C 280 .....	94
Figure 3.4d: Spectral energy decomposition of 3C 324 .....	95
Figure 3.4e: Spectral energy decomposition of 3C 352 .....	96
Figure 3.5: Comparison of alignment at 2500A to $1\mu$ in the sample .....	97
Figure 3.6: Detailed montage of 3C 368 .....	98
Figure 3.7: Color-color diagram for 3C 368 field .....	99
Figure 3.8a: Color vs. 2500A magnitude for the sample .....	100
Figure 3.8b: Color vs. $1\mu$ magnitude for the sample .....	101
Figure 3.9a: Alignment at 2500A vs. color for the sample .....	102
Figure 3.9b: Alignment at $1\mu$ vs. color for the sample .....	103
Figure 3.10: Alignment vs radio source size for the sample .....	104
Figure 3.11: Improved K' image of 3C 267 .....	105
Figure 4.1: Images of 3C 65 and 3C 437 and residuals .....	121
Figure 4.2: Montage of the model fitting analysis .....	122
Figure 4.3: The $\mu_e$ - $\log r_e$ diagram .....	123
Figure 5.1: Montage of multicolor 3C 65 images .....	133
Figure 5.2: Spectral energy distribution of the 3C 65 components .....	134
Figure 5.3: Montage of multicolor 3C 326.1 images .....	135

Figure 5.4: Spectral energy distribution of the 3C 326.1 component ..... 136

## CHAPTER 1: INTRODUCTION

The increasing number of radio galaxies that have been found at  $z \gg 1$ , including several examples with  $z > 3$  (Lilly 1988; Rawlings, Eales, & Warren 1990; Chambers, Miley, & van Breugel 1990; McCarthy et al. 1991; H. Spinrad 1990, private communication) has led to increased interest in the evolutionary status of these remote galaxies. At present, radio galaxies offer an unparalleled opportunity to study stellar populations at early epochs in the Universe.

The basic optical-infrared photometric properties of powerful radio galaxies at  $z > 1$  were established some time ago (Lilly & Longair 1984; Eisenhardt & Lebofsky 1987; Dunlop et al. 1989; Lilly 1989). In the near-infrared  $K$ -band, which samples a rest wavelength of around  $1 \mu\text{m}$  at  $z = 1$ , the radio galaxies appear to be remarkable homogeneous. Single-element photometry with large 8"-12" apertures of complete 3C and "1 jansky" samples (Lilly & Longair 1984; Lilly, Longair, & Allington-Smith 1985; Lilly 1989) shows, from very low redshifts to at least  $z = 2$ : (a) a small dispersion in the  $K$ -band absolute magnitude of only 0.4-0.5 mag (at a given redshift) and (b) a striking continuity in mean absolute magnitude with redshift. In contrast, a wide range of optical-infrared colors is observed, indicating a large variation in ultraviolet luminosities at  $\lambda < 3000 \text{ \AA}$ . Some radio galaxies at  $z > 1$ , such as 3C 65, have optical-infrared colors that are not much bluer than those of unevolving elliptical galaxies, while others, like 3C 368, have the colors of Irr galaxies. This uniformity in the rest-frame red/visual and the wide variation in the rest-frame ultraviolet have generally been interpreted (Lilly & Longair 1984; Lilly

1989) in terms of a homogeneous populations of host galaxies, selected by a mass-selection function that works in a similar fashion over the whole interval  $0 < z < 3$  and selects from a population of massive galaxies of roughly uniform age at a given epoch, so that the mass-to-light ratio smoothly varies with redshift. In this picture, a blue galaxy such as 3C 368 is interpreted as being as old as the much redder 3C 65, but with a much stronger active blue component, rather than as an intrinsically young system. In this interpretation, the light from this older population dominates the long-wavelength continuum emission and is responsible for the small scatter in the  $K$ -band. The ultraviolet light, which shows the large variations from galaxy to galaxy, has generally been ascribed to a very young stellar population produced in a vigorous burst of star formation, possibly associated with the radio activity (see, e.g. Lilly & Longair 1984), though other forms of ultraviolet activity cannot be ruled out at this time (see below).

We will henceforth refer to this interpretation as the "old galaxy hypothesis." The key element of this idea is that the small dispersion in the  $K-z$  relation arises because of the dominance in the infrared wave band of a homogeneous population of host galaxies. Consequently, in this view, the age of all the radio galaxies at a given redshift is constrained by the colors of the reddest object in the sample: At  $z = 1$ , this is 3C 65, which has an implied minimum age of  $2 \times 10^9$  yr (Chambers & Charlot 1990), suggesting  $z_F > 2.2$  (for  $\Omega_o = 1$  and  $H_o = 50 \text{ km s}^{-1} \text{ Mpc}^{-1}$ ). If the *continuity* of the  $K-z$  relation is taken seriously as indicating a steady evolution in luminosity, then we can infer that the radio galaxies at  $z = 1$  formed at even higher redshifts, i.e.,  $z_F > 5$  as inferred from the  $3-4 \times 10^8$  yr ages of the radio galaxies at

$z \sim 3.5$  (Lilly 1988; Chambers & Charlot 1990). It should be noted that the old galaxy hypothesis makes no statement per se about the nature of the ultraviolet continuum. If it is correct, the old galaxy hypothesis has important ramifications for our understanding of galaxy formation, for two reasons. First, it provides one of the strongest indications that the Universe at  $z > 1$  is basically similar to the local Universe—at least one class of galaxies has very similar properties at very high redshifts (at least at long wavelengths) compared with nearby galaxies selected in a similar way. Second, if it can be extended to the newly found systems at  $z > 3$ , then it demonstrates that at least some massive galaxies formed at very early times in the Universe.

Since 1985, detailed observations of the morphologies and spectra of the ever-increasing number of radio galaxies identified at  $z \gg 1$  have led to both refinements of, and challenges to, this basic picture. First, McCarthy et al. (1987b) and Chambers, Miley, & van Breugel (1987) discovered that the optical continuum (i.e., the rest-frame ultraviolet) and the [O II]  $\lambda 3727$  emission of a large fraction of radio galaxies at  $z > 0.8$  are aligned with the axis of the radio source in a way not encountered at low redshift. These authors interpreted this "alignment effect" in terms of the jet inducing star formation, and several theoretical explorations of this effect have been made (de Young 1989; Rees 1989; Daly 1990; Begelman & Cioffi 1989; Bithel & Rees 1990).

To date, the mechanism or mechanisms responsible for the alignment effect have not been established. Chambers & McCarthy (1990) have presented evidence that young stars are indeed responsible for the ultraviolet emission by co-adding the

spectra of different radio galaxies, and have claimed to discern in the integrated spectrum "stellar" absorption lines. On the other hand, de Serego Alighieri et al. (1989), Scarrott, Rolph, & Tadhunter (1990), and Jannuzi & Elston (1991) have detected significant polarization in 3C 368, 3C 277.3 and 3C 265. These observations support the idea that the aligned continuum emission is scattered light from an anisotropically emitting nucleus (see Fabian 1989), as might be produced in the hypothesis recently revived by Barthel (1989) that unifies radio galaxies and quasars through orientation effects. In the case of the line emission, van Breugel & McCarthy (1990) have also argued that the line ratios favor a relatively hard ionizing spectrum and that the required ionizing flux necessitates an obscured nucleus, given the absence of a bright nuclear source of ultraviolet emission. Other alternatives include a model proposed by Daly (1992b) in which the emission is caused by inverse Compton scattering of cosmic microwave background photons by relativistic electrons. This model is attractive because it predicts the observed correlations between (a) color and radio spectral index (Lilly 1989), and (b) emission line luminosity and radio power. It must be noted that the spectral and polarization observations have generally included light from the entire galaxy and might therefore include a substantial contribution from a central nuclear source and the stellar population even if a different mechanism is responsible for the emission in the outer regions. Thus, there is a continuing debate on the origin of the ultraviolet continuum, the cause of the ultraviolet alignment effect, and the relative importance of stellar and nonstellar emission at short wavelengths. Of course, several different phenomena may well be occurring in practice.

In parallel with these studies, there has also been considerable attention paid to the so-called Lyman- $\alpha$  galaxies, and in particular to objects such as 3C 326.1 at  $z = 1.8$ , which was claimed by McCarthy et al. (1987b) to represent a new class of gaseous radio galaxy in which the bulk of the stellar population had yet to form. However, infrared observations of this object (Lilly & Maclean 1989) reveal a compact component coincident with one of McCarthy et al.'s "knots." This object is located between the radio lobes and has similar photometric properties to other radio galaxies. This suggests that it contains a substantial stellar population of moderate age and hence that it should not be considered a forming protogalaxy. This object therefore now fits in with the old galaxy hypothesis, at least with respect to its broad photometric properties.

In 1988, a more direct challenge to the old galaxy model came from early infrared images of  $z > 1$  radio galaxies taken with newly implemented infrared array detectors. These infrared images included examples of elongated morphologies and alignment with the optical and radio jet axes (Eisenhart et al. 1990; Chambers, Miley, & Joyce 1988a; Djorgovski et al. 1991; Eales and Rawlings 1990). Because the "old galaxy hypothesis" predicts that the infrared light is dominated by dynamically relaxed, and hence, generally round stellar populations, these examples of infrared alignment were generally considered to be in contradiction to the "old galaxy hypothesis," and prompted a renewed interest in developing alternate explanations for the small dispersion in the  $K-z$  relation. Alternative models have been advanced, and two, which involve young stellar populations, merit particular attention.

In the first model, Chambers & Charlot (1990) have argued that the bluer radio galaxies may in fact be much younger systems than the redder ones, and that within the sample at  $z \approx 1$ , the galaxies span a wide range of ages. We will refer to this as the "range of ages model." They showed that, for a particular choice of the initial mass function, the evolution in the red/visual luminosity with age may be made small enough that the small dispersion in  $K$  may be preserved even with a large range in age within the radio galaxy sample (e.g.,  $3 \times 10^8$  yr for 3C 368 to  $2 \times 10^9$  yr for 3C 65, both at  $z = 1.1$  and both with observed  $K = 17$ ). Of course, a tight mass-selection effect must still operate, and this may be difficult to explain over the wide range of dynamical ages represented by the systems in this picture (from  $\sim 1$  dynamical time scale for 3C 368 to  $\sim 100$  times longer for radio galaxies at low redshifts). This range-of-ages interpretation had always been considered as a possible explanation for the range of colors (the stellar population models have not changed substantially over the last few years) but was originally rejected by Lilly & Longair (1984) because it was believed that it would lead to an unacceptably high dispersion in the  $K-z$  relation. Indeed, Lilly (1989), making the assumption that the run of absolute magnitude with redshift in the  $K-z$  diagram was entirely due to an evolving mass-to-light ratio argued that the spread in age within the radio galaxy population at  $z = 1.5$  could be no more than  $\Delta\tau/\tau \approx 25\%$  and was in all likelihood somewhat less. Chambers & Charlot's (1990) conclusion is dependent on the choice of the initial mass function, and, to a lesser extent, the star formation history, although the requirements are not unreasonable. In passing, it should be noted that the reduction in the minimum age of the  $z = 3.4$  radio galaxy 0902+34 to  $4 \times 10^8$  yr

(Chambers & Charlot 1990) from the 1 Gyr age proposed earlier (see Lilly 1988) was primarily due to a reduction in the  $K$  brightness by about 1 mag (Lilly 1990) rather than to any particular feature of the evolutionary models used.

Noting that the blue radio galaxies such as 3C 368 may, on the basis of their broad-band colors, be only  $3 \times 10^8$  yr old, Chambers & Charlot (1990) have suggested that the interaction of radio jets with the ambient gaseous medium may be a dominant process in the formation of massive galaxies. On the other hand, Daly (1992a) and Leahy (1990) have both pointed out time-scale difficulties with this scheme based on the radio source lifetimes, which they estimated to be of order a few times  $10^7$  years for typical 3C sources at  $z = 1$  (see also Alexander & Leahy 1987). Hence, even in the case of 3C 368, which is inferred to have a minimum age of  $3 \times 10^8$  yr (Chambers & Charlot 1990), the bulk of the galaxy must have been formed in previous, more vigorous, episodes of the radio source, and this removes some of the appeal of this model.

In the second model, Bithel & Rees (1990) have advocated a quite different scheme in which the  $K$ -band light comes from extremely young populations ( $10^7$  yr) of red supergiants. The attraction of this is that the ages of these populations are then fully consistent with the lifetime of a single outburst of the radio source. These authors suggested that the observed range of colors could represent different phases of rapidly evolving stellar populations of extreme youth. Given that an individual massive star produces most of its bolometric luminosity as a blue supergiant (Chiosi & Maeder 1986), the circumstances for domination by red supergiants to occur are very contrived—requiring a very narrow range of stellar masses and ages (see Lilly

1990). The rapid evolution of this population would certainly produce a wide range in mass-to-light ratios and hence an unacceptably large scatter in the  $K-z$  diagram.

In attempting to distinguish experimentally between the old galaxy model and the range-of-ages model, it should be realized that, as defined above, they represent extreme positions. Indeed the definition of the age of a stellar population is clearly somewhat ambiguous in the face of what may be quite large bursts of star formation. Assuming that the blue light is coming from young stars, then few would deny that 3C 368 is younger than 3C 65 if a *luminosity-weighted* average of the stellar population is taken, but a *mass-weighted* average would produce comparable ages if the old galaxy model is correct. While the true situation may be somewhat blurred between these extremes, the conceptual distinction is clear, and the question of whether the bluest galaxies contain an old stellar population similar to that in the reddest galaxies is clearly of great importance to our view of the formation of massive galaxies.

Much of the motivation for the theoretical work described above has come from the early infrared imaging observations, and indeed, the morphology at infrared wavelengths clearly offers a test of the old galaxy hypothesis. The mature galaxy component that is assumed to underlie the aligned active component should be dynamically relaxed and should not display significant morphological peculiarities. If peculiarities are seen, then this is a strong argument for either much younger stellar ages, i.e., shorter than the dynamical time scale for the system, or for a nonstellar origin for the infrared light. We stress that the old galaxy hypothesis is *not necessarily* invalidated by the presence of an aligned component in infrared images, regardless of its color. The test, rather is to *determine whether these*

*morphologically peculiar components produce so much of the large-aperture integrated light that the conventional interpretation of the small scatter in the infrared Hubble diagram in terms of mature underlying host galaxies can be ruled out.*

The original studies of the infrared morphologies were carried out on limited samples of objects—3C 368 (Chambers, Miley, & Joyce 1983a; Djorgovski et al. 1991), 3C 356 (Eales & Rawlings 1990), and a sample of eight 3C radio galaxies with  $0.7 < z < 1.8$  (Eisenhardt & Chokshi 1990). These authors all found some "infrared alignment" in the radio galaxies and concluded with varying degrees of conviction that the infrared light could not be dominated by old stars to the degree required to produce the small scatter in the  $K$ - $z$  relation. Two criticisms may, however, be applied to these early papers. First, there was very little attempt at quantitative analysis. Clearly, unless the aligned component is implausibly blue, it must contribute some significant fraction of the  $K$ -band light. If the aligned component has high surface brightness relative to the more diffuse outer regions of an extended underlying galaxy, it may produce dramatic morphological peculiarities and yet contribute a relatively small fraction of the total light. As an example, Lilly (1989) decomposed the overall spectral energy distributions of high- $z$  radio galaxies into the sum of an Irr plus a gE galaxy. In this heuristic exercise, the fraction of the  $K$ -band light that came from the blue, potentially aligned, Irr component was designated  $f_K$ . In the 3C sample at high redshifts, the average value of  $f_K$  was 20%, with a dispersion within the sample of 10% and a maximum of about 40% in the case of very blue objects like 3C 368. Clearly, a  $20\% \pm 10\%$  contribution from an active

component would not significantly perturb the scatter in the  $K-z$  relation which will have an intrinsic dispersion of order 0.4 mag. Of course, the aligned component could in reality have a different spectral energy distribution than that of an Irr galaxy, which would lead to different levels of contamination.

The potentially large morphological effects of components with relatively minor contributions to the total light are illustrated in Figure 1.1 (*upper panel*). We have constructed model radio galaxies bin which we have combined a round component with a de Vaucouleurs profile ( $r_e = 2''$ ) and an aligned component, assumed to be one-dimensional and of length  $4''$ . These have been smoothed with a Gaussian point-spread function of  $1''$  FWHM. Models in which 0%, 20%, and 50% of the light within a  $4''$  aperture is contributed by the aligned component are shown in Figure 1. It can be seen that a 20% linear contribution can produce a strikingly aligned image, yet will not perturb the scatter in the  $K-z$  relation. An aligned component that was more concentrated toward the outer regions would have a correspondingly larger morphological effect. We return to these models later when a quantitative measure of asymmetry is developed.

The likely contamination from the aligned component makes a quantitative analysis absolutely essential in order to see whether the morphological peculiarities are due to this contamination alone.

The second criticism is that only a few generally nonrepresentative objects were observed, although the conclusions drawn from them have frequently been applied to the population as a whole. For instance, 3C 368 has often been taken as a prototype for high-redshift radio galaxies. In fact, as noted above, it is a very

*extreme* object. It has the bluest ( $r-K$ ) color, and among the strongest emission lines, in the Lilly & Longair (1984) sample. In addition, there is recent evidence for a superposed M star in this system (Hammer, Le Fèvre, & Proust 1991; see also Chapter 3). In the case of 3C 356, another well-studied object (Eales and Rawlings 1990; Eisenhardt & Chokshi 1990), it is clear that the "alignment effect" is morphologically distinct from that seen in most other radio galaxies, with a detached red lump several arcseconds away rather than a continuous smooth component extending out from the central object. The dynamical argument for this detached component not being a mature stellar population is correspondingly weaker. Even the more broadly based Eisenhardt & Chokshi (1990) study was nevertheless, in their words, "biased towards galaxies known to have extended asymmetric  $R$ -band and [O II]  $\lambda 3727$  or Lyman  $\alpha$  emission."

The present study was undertaken to examine the optical and infrared morphologies of distant radio galaxies in a systematic way. In this initial investigation we decided to limit our attention to moderate redshifts ( $z \approx 1$ ) so that (a) the objects are relatively bright and (b) a "statistically complete" sample could be observed. Our sample lies above the apparent onset of the alignment effect at  $z = 0.8$  (McCarthy et al. 1987a), and we suspect that the radio galaxies at higher redshifts  $z > 2$  are qualitatively similar to those in the present sample at  $z = 1$ , though this is at present a conjecture. We have used a homogeneous set of optical and infrared line and continuum images of a well-defined sample of 13 3C radio galaxies with  $0.8 < z < 1.3$  that should be *unbiased with respect to the properties of powerful radio galaxies* as found in the 3C catalog at  $z \approx 1$ . Furthermore, we have attempted to carry out a

quantitative and objective analysis of the morphologies of these galaxies as a function of wavelength in order to constrain the spectral energy distributions of the various morphological components and, in particular, to determine the contribution in the infrared of the "aligned" component that dominates at short wavelengths. We find that the observations generally provide strong support for the basic old galaxy interpretation of high-redshift radio galaxies. Furthermore, the study turned up two classes of objects which merited further study: The first are extremely quiescent radio galaxies that appear as evolved galaxies in the infrared, thereby offering an unparalleled opportunity to study ellipticals at high-redshifts. The second are rare examples of the alignment effect in which the aligned emission is detached from the main galaxy (rather than extending continuously from the main galaxy), which offer the potential of studying the alignment effect in an aperture free from contamination by the nuclear source and old stellar population of the main galaxy.

The organization of this dissertation is as follows: In the second chapter we review the rationale behind the sample selection and the observations that were taken, as well as the methods of data acquisition and reduction. In the third chapter we present the morphological analysis of the  $z \approx 1$  3C sample. In the fourth chapter, we present a detailed analysis of the infrared morphologies of two quiescent 3C galaxies, which appear to be similar to low redshift gE galaxies associated with powerful radio sources. In the fifth chapter, we discuss examples of detached aligned morphological components and argue that these are the same phenomenon as the alignment effect seen in the sample as a whole. In the final chapter we summarize the results and discuss promising directions for future research.

## References for Chapter 1

- Alexander, P., & Leahy, P.J. 1987, MNRAS, **225**, 1P
- Barthel, P.D. 1989, ApJ, **336**, 606
- Begelman, M.C., & Cioffi, D. 1989, ApJ, **345**, L21
- Bithel, M., & Rees, M.J. 1990, MNRAS, **242**, 570
- Chambers, K.C., & Charlot, S. 1990, ApJ, **348**, L1
- Chambers, K.C., & McCarthy, P.J. 1990, ApJ, **354**, L9
- Chambers, K.C., Miley, G., & Joyce, R.R. 1988a, ApJ, **329**, L75
- Chambers, K.C., Miley, G., & van Breugel, W. 1987, Nature, **329**, 609
- Chiosi, C., & Maeder, A. 1986, ARA&A, **24**, 329
- Daly, R.A. 1990, ApJ, **355**, L59
- Daly, R.A. 1992a, ApJ, **386**, L9.
- Daly, R.A. 1992b, ApJ, in press
- de Young, D.S. 1989, ApJ, **342**, L59
- di Serego Alighieri, S., Fosbury, R.A.E., Quinn, P.J., & Tadhunter, C.N. 1989, Nature, **341**, 307
- Djorgovski, S., Wier, N., Matthews, K., & Graham, J. 1991, in ASP Conf. Ser. 14, with Infrared Arrays, ed. R. Elston (San Francisco: ASP), 112
- Dunlop, J.S., Guiderdoni, B., Rocca-Volmerange, B., Peacock, J.A., & Longair, M.S. 1989, MNRAS, **240**, 257
- Eales, S.A., & Rawlings, S. 1990, MNRAS, **243**, 1P
- Eisenhardt, P., & Chokshi, A., Dickenson, M., Spinrad, H., Djorgovski, S.G., & McCarthy, P. 1991, in ASP Conf. Ser. 14, with Infrared Arrays, ed. R. Elston (San Francisco: ASP), 100
- Eisenhardt, P., & Chokshi, A. 1990, ApJ, **351**, L9

- Eisenhardt, P., & Lebofsky, M.J. 1987, ApJ, **316**, 70
- Fabian, A.C. 1989, MNRAS, **238**, 41P
- Hammer, F., & Le Fèvre, O., Proust, D. 1991, ApJ, **374**, 91
- Jannuzi, B.T., & Elston, R. 1991, ApJ, **366**, L69
- Leahy, P.J. 1990, private communication
- Lilly, S.J. 1988, ApJ, **333**, 161
- Lilly, S.J. 1989, ApJ, **340**, 77
- Lilly, S.J. 1990, in ASP Conf. Ser. 9, The Evolution of the Universe of Galaxies, ed. R.G. Kron (Dordrecht: Kluwer), 344
- Lilly, S.J., & Longair, M.S. 1984, MNRAS, **211**, 833
- Lilly, S.J., & Longair, M.S., & Allington-Smith, J.R. 1985, MNRAS, **215**, 37
- Lilly, S.J., & McClean, I.S. 1989, ApJ, **346**, L65
- McCarthy, P.J., Spinrad, H., Djorgovski, S., Strauss, M.A., van Breugel, W., & Liebert, J. 1987a, ApJ, **319**, L39
- McCarthy, P.J., van Breugel, W., Kapahi, V.K., & Subrahmanya, C.R. 1991, ApJ, **371**, 478
- McCarthy, P.J., van Breugel, W., Spinrad, H., & Djorgovski, S. 1987b, ApJ, **321**, L29
- Rawlings, S., Eales, S.A., & Warren, S. 1990, MNRAS, **243**, 14P
- Rees, M.J. 1989, MNRAS, **428**, 1P
- Scarrot, S.M., Rolph, C.D., & Tadhunter, C.N. 1990, MNRAS, **243**, 5P
- van Breugel, W.J.M., & McCarthy, P.K., 1990, in ASP Conf. Ser. 9., The Evolution of the Universe of Galaxies ed R.G. Kron (Dordrecht: Kluwer), 359

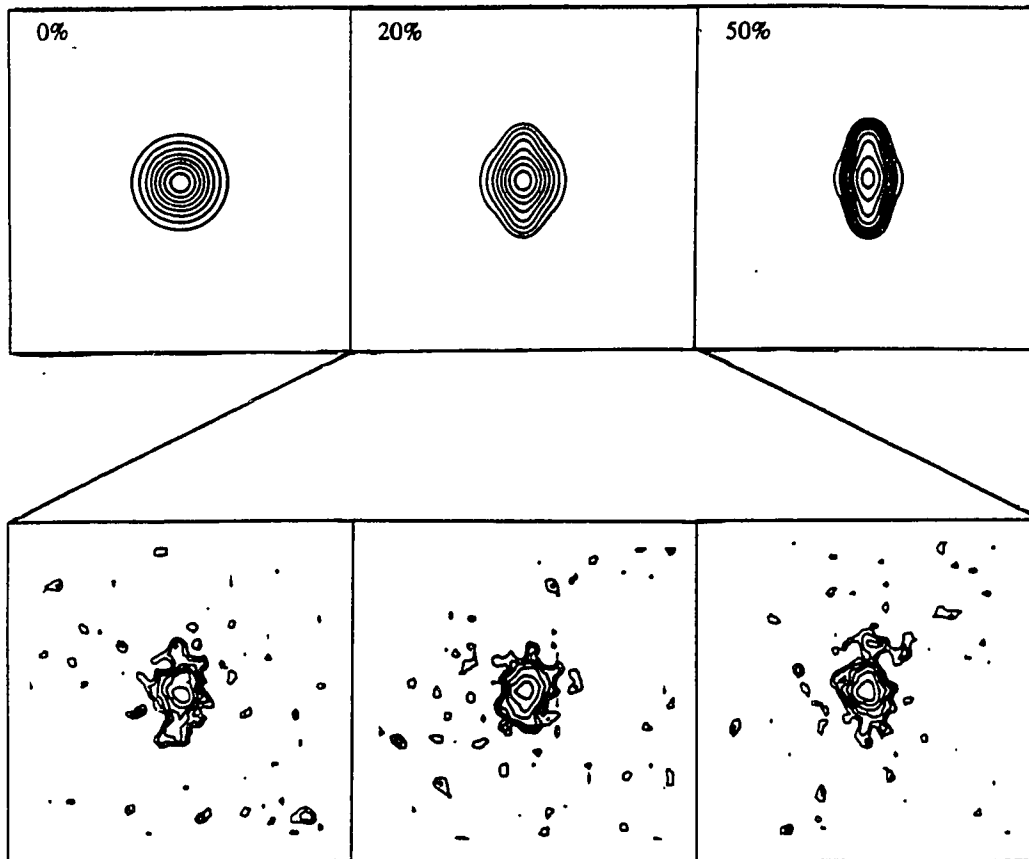


**Figure 1.1**—Effects of adding a linear component to a symmetric host galaxy with a de Vaucouleurs profile. Each image is 15" square and has been smoothed with a Gaussian of 1" FWHM. The upper panels show composite galaxies in which the linear component contributes 0%, 20%, and 50% of the total flux in a 4" aperture. The lower panels show the effect of adding noise to the 20% simulation. The noise has similar characteristics to that in our real data.

## CHAPTER 2: OBSERVATIONS AND DATA REDUCTION

In this chapter we review the rationale behind the sample selection and the observations, as well as the methods of data acquisition and reduction. This dissertation primarily involved deep high-resolution imaging at optical and near-infrared wavelengths of a sample of  $z \approx 1$  3C radio galaxies as well as selected radio galaxies at higher-redshift. As astronomical targets go, these galaxies are faint (typically  $V > 22$  and  $K > 17$ ) and small (a few arcseconds in size, with morphological structure on sub-arcsecond scales). To acquire images of sufficient depth and resolution, fairly conventional methods of imaging with optical CCD's were employed, as well as newly developed techniques for deep infrared imaging designed to take advantage of the recent advances in infrared array technology. During the course of the project, all of the major optical and infrared telescopes at Mauna Kea Observatories were used.

### 2.1 Rationale Behind the Sample Selection

For this project, a subsample of 13 radio galaxies from were selected from the Laing et al. (1983) revised 3C extragalactic catalog having  $0.8 < z < 1.3$  and  $\delta > 55^\circ$ . The motivations for choosing to use this particular sample were threefold: First, at these redshifts, radio galaxies begin to display the alignment effect (McCarthy et al 1987; Chambers et al 1987), yet are still bright enough ( $V \approx 22$  and  $K \approx 17$ ) to be imaged in a few hours integration using 2-4 meter class telescopes at

Mauna Kea, thereby allowing the project to be completed in roughly 10 nights observing. Second, it is possible to construct a statistically complete subsample of  $z \approx 1$  radio galaxies from the 3C source catalog, which has been completely identified with redshifts (e.g., Spinrad et al. 1985). The sample used here is "complete" in the sense that it is selected purely on the basis of radio luminosity and having been identified as radio galaxies (as opposed to quasars). One source, 3C 263.1, was later found out to have been accidentally missed because of an erroneous cataloged redshift. The third motivation for choosing this sample was that, at the time that this dissertation was begun, a set of narrow-band optical images had already been obtained for these 13 objects (Stockton and Lilly 1988).

## 2.2 Rationale Behind the Proposed Observations

For this sample, we required a set of high-resolution images spanning a range in rest-frame wavelengths from the UV to near-infrared, including both continua and emission line data. Lilly and Stockton had already obtained narrow band images which sampled the rest-frame continua near  $4000 \text{ \AA}$  as well as the prominent [OII]  $\lambda 3727$  emission-line feature. We decided to obtain at least two additional images for each galaxy in both (1) B or V, corresponding to the rest-frame region near  $2500 \text{ \AA}$ , and (2) H or K, corresponding to the rest frame region near  $1 \mu m$ . The exact choice of filter reflected a desire to sample uniform parts of the restframe continua from galaxy to galaxy, while minimizing or avoiding contamination by prominent emission lines such as CII]  $\lambda 2326$ , [NeIV]  $\lambda 2423$ , MgII  $\lambda 2798$ , [NeIII]  $\lambda 3967$ , [NeIV]  $\lambda 4720$ ,

[OIII]  $\lambda$ 5007, H $\alpha$   $\lambda$ 6563, [SII]  $\lambda\lambda$  6716,6731, [SIII]  $\lambda\lambda$  9069,9531, and [SIV]  $\lambda$ 1.52 $\mu$ m. These and other emission lines have been detected in the spectra of high-redshift radio galaxies, with equivalent widths comparable to those of Ly $\alpha$  and [OII]  $\lambda$ 3727. The Ly $\alpha$  emission and [OII]  $\lambda$ 3727 of high-redshift radio galaxies shows a tendency to be aligned with the radio axis. These other lines are also expected to trace the aligned component, and could significantly affect the observed morphology if present in a continuum bandpass.

### 2.3 Review of the Observations

The principle broad-band optical and infrared imaging observations used in this project were made during 1990 at Mauna Kea Observatories. During the course of the project, state-of-the-art optical CCD cameras and infrared arrays were used at the UH 2.2 m, the IRTF (3.0 m), UKIRT (3.8 m), and CFHT (3.6 m) facilities. The details of the observing runs for this sample are reported in Table 2.1 and described below.

#### 2.3.1 Optical Observations

The optical data for the 13 3C sample objects consists of narrow band images corresponding to the rest-frame 4000  $\text{\AA}$  region and B and/or V band images corresponding to the rest-frame 2500  $\text{\AA}$  region.

Most of the narrow band images were obtained prior to the beginning of this dissertation by Stockton and Lilly (preliminary results reported by Stockton and Lilly

1989). The observations were made using the Galileo/IFA TI 500×500 CCD system at the CFHT 3.6 m in July 1986 and at the UH 2.2 m in January 1986, June 1986 and February 1987, and with a TI 800×800 CCD system at the UH 2.2 meter in May 1990. The filters employed were custom designed to give  $\approx 200 \text{ \AA}$  (rest-frame) passbands corresponding to the continuum regions just shortward of  $3700 \text{ \AA}$  and longward of  $4000 \text{ \AA}$ , as well as a  $50 \text{ \AA}$  (rest-frame) passband filter centered on the [OII]  $\lambda 3727$  emission line.

Additional optical images in the B or V passbands were obtained for most of the sample with the UH 2.2 m telescope during a run in 1990 March with a TI 800×800 detector at 0.26 arcsec per pixel. For the remaining galaxies, B or V band images were generously provided by Le Fèvre and Hammer (previously published in Le Fèvre, Hammer, & Jones 1988; Le Fèvre & Hammer 1988; Hammer & Le Fèvre 1990).

### 2.3.2 Infrared Observations

Twelve of the thirteen sources in the complete 3C  $z \approx 1$  sample, lie within in an RA range suitable for observing during the spring semester (all except for 3C 65). The infrared observations for the twelve spring objects were made with the Proto-CAM array at IRTF and the IRCAM array at UKIRT during runs in March 1990. The program for the two runs included some degree of overlap, which was planned to allowing a comparison of images of galaxies obtained with two separate telescope/detector setups in order to provide a test of the validity of the innovative

methods of infrared data acquisition and reduction. In the case of the ProtoCAM array, these runs represented the first observations of galaxies as faint as  $K > 16$ . Between the two runs, an attempt was made to quickly reduce the ProtoCAM data and it was discovered that there were problems in reducing the images of galaxies with  $K > 17$  (the reasons for which will be discussed in more detail below). Fortunately, we were able to adjust the observing plan for the UKIRT run to incorporate repeat observations of these problem galaxies, and a complete set of adequate images was obtained for the 12 spring objects.

The single fall object in the sample, 3C 65, was observed in September 1990 at CFHT using the newly developed UH NICMOS-3 array. Infrared images of other 3C objects having  $z > 1$ , including 3C 437 ( $z = 1.480$ ) were also obtained during this run. The NICMOS-3 data are of superb quality, and prompted a more detailed analysis of the 3C 65 image than was possible with the ProtoCAM and IRCAM images (the results of which are described in Chapter 4).

## **2.4 Methods of Data Acquisition and Reduction**

### **2.4.1 Optical Imaging**

The optical data were taken and reduced using conventional methods developed during the early 1980's for CCD imaging of faint objects. The narrow band images were originally reduced by Stockton, and then further processed and analyzed by the author during the course of the dissertation.

### 2.4.1.1 The Narrow Band Images

Each narrow-band observation consisted of several exposures between which the the telescope was offset  $\approx 10''$  in order to reduce the effect of bad pixels and columns on the data. Dark and bias frames were subtracted from the raw images, which were then flattened through division of a dome flat. The dome flat was constructed from exposures of the telescope dome illuminated by a flat-spectrum lamp, and was generally sufficient to flatten the pixel-to-pixel variations to  $\approx 1\%$ , although in some images, a gradient or fringe pattern was present at a higher level (see below). The flattened exposures were coregistered using the positions of field objects. Finally, calibration was achieved through measurements of spectrophotometric standards from the list of Oke & Gunn (1983)

The images were further refined by the author after the initial processing. In many cases the background showed residual gradients or "red fringes." The latter phenomenon is caused by the presence of a strong sky line within the filter bandpass having a wavelength comparable to the thickness of the CCD. The result is a low-level pattern of concentric or parallel ripples which is not removed by the dome flat. The variations can affect the appearance and photometric measurements of faint objects. Where possible, these and other gross cosmetic defects were characterized and removed through application of a median box filter. A background value was then determined from the modal value of pixels in the central quarter of the array and subtracted from the image. After making these final refinements, the relative quality of the images for each object (consisting of both UH and CFHT data, with

overlap in some cases) was assessed, and the best images selected to be resampled to a common scale and orientation, and coregistered using the positions of field objects. The FWHM of the point-spread function of each image was determined from stellar field objects. For each galaxy, a set of co-smoothed images, having approximately the same FWHM, was produced through convolution with a gaussian point-spread function. In some cases, co-smoothed UH and CFHT images of a galaxy taken in the same filter were combined to give a deeper image.

The resulting set of images consisted of three images per object: the continuum just shortward of the rest-frame 4000 Å break feature (*SC*), the continuum just longward of the 4000 Å break feature (*LC*), and the [OII] λ3727 emission line (*NB*). The line image (*NB*) contains a small continuum contribution which was removed to produce a line-only image. This was accomplished by subtracting off a 3727 Å continuum image (*C*) comprising a linear combination of the co-smoothed *SC* and *LC* images such that  $\gamma NB = C = \kappa SC + (1-\kappa) LC$ . The two coefficients were optimized through a linear regression of the photometric fluxes of field objects measured within apertures. It was generally found that the best fitting coefficient  $\kappa$  was close to the value obtained from an interpolation based on the effective wavelengths and bandpasses of the continuum filters and assuming no spectral curvature. The best fitting coefficient  $\gamma$ , was generally found to be near unity, as is expected for accurately calibrated images. For each galaxy, a co-smoothed, coregistered set of three images was produced: two corresponding to the continua above and below the 4000 Å break, and one of pure [OII] λ3727 line emission.

### 2.4.1.2 Broad Band Imaging

The B and V images were reduced using standard procedures of bias and dark current subtraction and division by a normalized dome flat. The flattening method was further refined by the technique of statistical sky-flattening. In broadband applications the high background flux results in exposures that are sky-noise dominated within a fairly short exposure time ( $\approx 10$  minutes for optical imaging). Thus, several short exposures of the object field can be taken between which the telescope is moved 10-20" in a mosaic pattern, so that each part of the field is sampled by different array pixels on each exposure. This provides an improved identification of cosmetic defects and cosmic ray events, and allows a "sky-flat" to be constructed from the median of normalized versions of the individual exposures taken throughout the night. The sky flat represents the array's pixel response to the sky devoid of objects. The B and V band images were divided by a normalized version of the sky flat, which reduced the pixel-to-pixel variations in the images to better than 0.1%. After flattening, a refined background level based on the modal value of pixels in the center region of the array was subtracted from each of the individual flattened B and V images. Photometric calibration was achieved through observations of Landolt (1983) standards. The entire set of B and V band images was resampled to the common scale and orientation used for the narrow band images (see above) and coregistered using the positions of field objects. The FWHM of the point spread function of each image was determined from stellar field objects, so that later a co-smoothed set of images could be produced for each object.

### 2.4.2 Infrared Imaging

The use of newly developed infrared array technology was central to this project. Infrared arrays first came to Mauna Kea Observatories during the late 1980's, with the development of the IRCAM 58x62 InSb array at UKIRT (McLean 1987), and the JPL/SISEX HgCdTe 64x64 array (Capps et al. 1987) allowing near-infrared images of high-redshift radio galaxies to be obtained for the first time from the summit of Mauna Kea. During the same time period, the early infrared images of high-redshift radio galaxies were being obtained elsewhere (e.g., Chambers, Miley and Joyce 1988; Djorgovski et al. 1991; Eales & Rawlings 1990; Eisenhardt and Chokshi 1990), which demonstrated the potential of infrared arrays to greatly expand our understanding these objects. In Spring 1990, at the beginning of this dissertation, the MKO facilities included two 58x62 InSb array cameras, the IRCAM at UKIRT, and the newly-developed ProtoCAM at IRTF. These two arrays were used to image all but one of the 3C  $z = 1$  sample in the H and/or K bands. By the Fall of 1990, the UH array had been upgraded to a NICMOS-3 256x256 HgCdTe array (Hodapp, et al 1992) which represented a great improvement over the previous generation arrays due to its larger size and increased sensitivity. The NICMOS-3 array was used to image the remaining member of the 3C sample (3C 65) as well as selected objects at higher redshift.

In order to flatten the infrared data to the level of uniformity required to image faint objects (i.e., to better than 1 part in  $10^4$ ), a method of statistical self-flattening similar to that used in flattening the optical CCD images is employed.

This method represents a substantial improvement over the traditional method of chopping to a nearby field: For a given exposure time, one gains a factor of root-two in signal to noise because the noise in the subtracted sky image is negligible, and an additional factor of two because the target object is kept within the field of the array during the entire observation. There are key differences, however, in the infrared procedure which are necessary because of the relatively high flux and rapid variability of the infrared background. The high background flux results in broad-band images that are background-noise-limited within  $\approx$  one minute or less. An observation consists of many short exposures (2-4 minutes), between which the telescope is moved a small distance (3-10") in a complex, repeating, rectilinear mosaic pattern. Because of the rapid variation in the background flux (and also because of the necessity to repeat the mosaic pattern), it is not feasible to use a large number of the exposures to construct a single all-purpose sky flat. Rather, a windowing function is used through the sequence of exposures to generate a corresponding sequence of individual sky flats. The sky flat for each data frame is constructed by taking the median of normalized versions of the preceding  $N$  frames and following  $N$  frames (excluding the frame being flattened), where the value of  $N$  is optimized for each data set through experimentation. Typically, it was found that a choice for  $N$  of about 6 produced the best results. Using this method, infrared images have been flattened to have a pixel-to-pixel variation of less than one part in  $10^5$ , enabling objects as faint as  $K \approx 20$  to be imaged.

In detail, the actual reduction algorithms developed for use in this dissertation are fairly complex, and were modified to take into account basic differences in the

operational properties of the three arrays used (IRCAM, ProtoCAM, and NICMOS-3). The ProtoCAM data was the most difficult to reduce for two reasons: First, it was discovered during our runs that the "true" flat pattern of the array (i.e., the pixel-to-pixel variation in quantum efficiency for a given bandpass) was very different from the background pattern seen in a long (2-4 min) exposure. This is because of a significant thermal contribution to the background flux from instrumental components in the dewar. In other words, the background seen in any ProtoCAM exposure has two components, the night sky and emission from the instrument, whose relative contribution varies throughout the night with changes in sky brightness and dewar temperature. A reduction algorithm was developed which is capable of taking this into account, and was successfully used to flatten and remove the background from ProtoCAM data (this algorithm is described in more detail below). In principle, the phenomenon of multiple background sources could be present in any array setup, and thus, in some sense, the basic form of the algorithm developed to reduce ProtoCAM array data represents the most cautious approach to reducing data from any array. The basic algorithm was also used to successfully reduce the IRCAM and NICMOS-3 data, which do not suffer from the same problem. In fact, all three arrays behave differently. The NICMOS-3 (HgCdTe) array has a high-level flat pattern ( $\approx 40\%$  variation) similar to that of an optical CCD, while the IRCAM array is flat to within 1%. The basic reduction algorithm also takes these differences into account.

The basic algorithm used in the reduction of infrared array data is outlined as follows. Before processing begins, a bad pixel mask is constructed for a given

observing run by analyzing images of the dark current and normalized dome flats, in which  $\approx 3\%$  of the pixels representing the extreme ends of the distribution are identified. Using this mask, the bad pixels in the raw data cube are replaced with a "magic number" value which subsequently acts as a flag for special treatment in the reduction algorithms. The first step in the reduction procedure is to subtract a dark current image ( $D$ ) from the masked version of the raw data cube ( $R$ ). The exposures are then crudely flattened through division of a normalized "crude flat" ( $F_c$ ) which can be provided either by a dome flat, or by adding all of the exposures, or by some similar means. Once crudely flattened, the frames are normalized to a common modal value ( $b$ ) through division by a vector ( $n_i$ ), and each frame further flattened through division by an individual median sky flat ( $F_s^{(i)}$ ) constructed by taking the median of normalized versions of the  $N$  preceding and  $N$  following frames. The flattened frames are then background subtracted and photometrically restored by subtracting off ( $b$ ), multiplying by ( $n_i$ ), and multiplying by the cumulative background pattern ( $F_c F_s^{(i)}$ ). Finally, the frames are divided by "true" array flat ( $F_t \equiv$  pixel-to-pixel variation in quantum efficiency response) which is constructed from quick exposures of the sky at twilight, or by spline fitting a surface to a mosaic pattern of quick exposures of bright stars. The result is a flattened, background-subtracted image ( $I$ ). Algebraically, the algorithm may be written as:

$$I = \left[ \frac{R-D}{n_i F_c F_s^{(i)}} - b \right] \times \left[ \frac{n_i F_c F_s^{(i)}}{F_t} \right] = \frac{R - D - b n_i F_c F_s^{(i)}}{F_t}$$

where the third term in the numerator may be simply understood as the image of the

background (which must be arrived at by roundabout means). After flattening, the individual exposures are coregistered and co-added. This procedure is capable of flattening infrared data to the level required to image objects fainter than  $K > 19$ .

It was found that coregistering was not always a trivial task. Ideally, the individual exposures are coregistered using the positions of field objects measured on expanded images. To accomplish this, it is basically necessary to detect bright field objects on individual (flattened) short exposures. It was generally trivial to find several bright objects within the large field of view of the NICMOS-3 array ( $>1'$ ), but bright field objects were not always available within the field of view of the IRCAM ( $\approx 40''$ ), and were rarely available within the field of view of ProtoCAM ( $\approx 20''$ ). In the case of the UKIRT data, the automated system of offsetting to mosaic positions and guiding on a star during exposures proved to be extremely accurate, so that the nominal mosaic pattern could be used to coregister the data. The IRTF was not equipped with such facilities at the time of the observations and significant drift in the telescope pointing sometimes occurred during the  $\approx 1$  hour long observations. For target objects with  $K < 17$ , the object itself was visible in individual exposures, and could be used to iteratively improve the coregistration by correcting for telescope drift. For fainter target objects, it was found that a preliminary coregistration of neighboring frames based on the nominal mosaic pattern could in some cases result in a detection of the object, thereby allowing an iterative correction for telescope drift. In some cases, however, the images of these fainter objects could not be coregistered, and they had to be observed again at UKIRT.

In addition to facilitating the detection of bright field objects, the large format of the NICMOS-3 array represents a significant advantage over the smaller format arrays because it allows a larger mosaic spacing, which was discovered to be crucial in the measurement of the characteristic scale sizes of galaxies. This is because the minimum pattern spacing determines the largest scale upon which emission from an extended object can be decoupled from the sky background in the median flat-fielding process. Any information on larger scales is destroyed, and faint "median ghosts" are generated in the positions of the offset field objects. The minimum pattern spacing used for the IRTF and UKIRT observations was only 3 and 5" respectively, which precluded a useful measurement of galactic scale sizes from the data. But with the NICMOS-3, observations employing a mosaic spacing of 10-20" became possible for the first time. This opportunity prompted a more refined version of the basic reduction algorithm described above, designed to minimize the effect of "median ghosting," while improving the flattening, coregistration accuracy, and the handling of bad pixels and cosmic ray events.

The improvement relies on an iterative approach to flat-fielding and coregistration. The first step is to use the basic algorithm to process and flatten the raw data cube. The frames are then coregistered to nearest-pixel accuracy and co-added, with cosmic ray events clipped, to produce a preliminary image from which an object mask is made by masking pixels above some value (typically chosen to be 2 or 3  $\sigma$ ). The coregistration vector is used in conjunction with the raw data cube to produce a "filtered" raw data cube in which magic number value in each bad pixel has been replaced by the median value of the pixels in the other frames throughout

the cube corresponding to that position in the sky. The object mask is used to produce a version of the filtered raw data cube in which the objects have been masked to the magic number value. The flattening procedure is then repeated from scratch, but this time using the object-masked and filtered raw data cube to produce median sky flats, which are used to flatten the filtered raw data cube. The individual frames are then expanded and coregistered to sub-pixel accuracy, producing a "second iteration" image that is free of the median ghosting effect. The process can be iterated multiple times, if desired, each time using the results of the previous iteration to produce an improved object mask, a more accurate coregistration vector, and an improved identification of bad pixels and cosmic rays. In practice, it was deemed unnecessary to go beyond a third iteration with the NICMOS-3 data.

The infrared images were photometrically calibrated through observations of standards from the list of Elias et al. (1982).

## **2.5 Combining and Displaying the Data**

The set of images for each galaxy were oriented to within a degree of NSEW (with north = top and east = left) and rescaled to a common plate scale of 0.200" per pixel, and coregistered using the position of field objects. Where possible, the point-spread function of each image was determined from stellar objects in the field. Where no field objects were available, the point-spread function was estimated from short observations of standard stars taken on either side of the observations. The co-smoothing was accomplished by convolving the images with a Gaussian point-

spread function. For each galaxy, the set of co-smoothed images was used whenever the analysis called for making photometric measurements or for constructing an algebraic combination of images.

The calibrated set of optical and infrared images were corrected for galactic reddening using the  $E_{B-V}$  maps of Burstein & Heiles (1982). The final images were put in the AB magnitude system, such that  $AB = -48.60 - 2.5 \log f_{\nu}$ , where  $f_{\nu} \equiv$  flux density in c.g.s. units. The magnitudes for objects referred to throughout this dissertation are generally given in AB mags. The AB magnitudes in the standard B, V, H or K bands may be transformed back to the standard  $\alpha$  Lyrae photometric system by addition of the following constants: 0.17, 0.00, -1.43, and -1.91 for B, V, H, and K, respectively.

Throughout this dissertation, the multi-wavelength set of images for a galaxy are generally presented as montages of 15"×15" fields centered on the peak of the infrared emission. The contours are plotted at *logarithmic* intervals of surface brightness (at a factor of 1.41, so that two contours correspond to a factor of two in surface brightness). This results in fewer contours than are displayed on linear plots, but allows a greater dynamic range to be presented, so that relative colors and magnitudes of different components can be most easily seen. Each plot typically includes the value of the lowest surface brightness contour (in AB mags per square arcsecond), as well as a hatched circle indicating the FWHM of the point-spread function.

## References for Chapter 2

- Burstein, D., & Heiles, C. 1982, AJ, **87**, 1165
- Capps, R.W., Hodapp, K.W., Hall, D.N.B., Becklin, E.E., Simons, D.A., Bailey, G.C., & Wright, V.G. 1987, in *Infrared Astronomy with Arrays*, ed. C.G. Wynn-Williams & E.E. Becklin (Univ. of Hawaii), 222
- Chambers, K.C., Miley, G., & Joyce, R.R. 1988, ApJ, **354**, L9
- Chambers, K.C., Miley, G., & van Breugel, W. 1987, Nature, **329**, 609
- Djorgovski, S., Weir, N., Matthews, K., & Graham, J. 1991, in ASP Conf. Ser. 14, *Astrophysics with Infrared Arrays*, ed. R. Elston (San Francisco: ASP), 112
- Eales, S.A., & Rawlings, S. 1990, MNRAS, **243**, 1P
- Eisenhardt, P., & Chokshi, A. 1990, ApJ, **351**, L9
- Elias, J.H., Frogel, J.A., Matthews, K., & Neugebauer, G. 1982, AJ, **87**, 1029
- Hammer, F., & Le Fèvre, O., 1990, ApJ, **357**, 38
- Hodapp, K.-W., Rayner, J., Irwin, E. 1992, PASP, in press
- Laing, R.A., Riley, J.M., & Longair, M.S. 1983, MNRAS, **204**, 151
- Landolt, A.U. 1983, AJ, **88**, 439
- Le Fèvre, O., & Hammer, F. 1988, ApJ, **333**, L37
- Le Fèvre, O., Hammer, F., & Jones, J. 1988, ApJ, **331**, L73
- McCarthy, P.J., van Breugel, W., Spinrad, H., & Djorgovski, S. 1987, **321**, L29
- McLean, I.S. 1987, in *Infrared Astronomy with Arrays*, ed. C.G. Wynn-Williams & E.E. Becklin (Univ. of Hawaii), 180
- Oke, J.B., & Gunn, J.E. 1983, ApJ, **266**, 713
- Spinrad, H., Djorgovski, S., Marr, J., & Aguilar, L. 1985, PASP, **97**, 932

Table 2.1: Log of Observations

3CR	Filter	$\lambda_o$ (Å)	UT Date	Telescope	Device	Exposure(s)	PSF(")
65	V		1987 Jun 19	CFHT	RCA2	1200	1.1
	SC	7515	1987 Feb 3	UH88	TI	1800	1.9
	[OII]	8115	1987 Feb 3	UH88	TI	3600	1.9
	LC	8784	1987 Feb 4	UH88	TI	3600	1.9
	H		1990 Sep 2	CFHT	NICMOS	4800	0.9
217	B		1990 May 20,21	UH88	NSF1	8400	1.3
	SC	6535	1987 Feb 3	UH88	TI	1800	1.6
	[OII]	7078	1987 Feb 3	UH88	TI	3600	1.6
	LC	8300	1987 Feb 3	UH88	TI	3600	1.6
	K		1990 Mar 25	IRTF	PCAM	6960	1.0
	K		1990 Mar 31	UKIRT	IRCAM	7800	1.3
226	B		1990 May 22	UH88	NSF1	600	1.0
	SC	6535	1987 Feb 4	UH88	TI	1800	1.2
	[OII]	6800	1987 Feb 4	UH88	TI	3600	1.4
	LC	7515	1987 Feb 4	UH88	TI	3000	1.5
	K		1990 Mar 23	IRTF	PCAM	2400	1.1
252	V		1988 Jan 21	CFHT	RCA2	420	0.6
	SC	7515	1987 Feb 3	UH88	TI	1800	1.1
	[OII]	7851	1987 Feb 3	UH88	TI	3600	1.1
	LC	8784	1987 Feb 3	UH88	TI	4200	1.1
	H		1990 Mar 31	UKIRT	IRCAM	5400	1.3
265	V		1988 Jan 21	CFHT	RCA2	4800	1.1
	SC	6535	1986 Jun 6	UH88	TI	1200	1.1
	[OII]	6750	1986 Jun 6	UH88	TI	3600	1.1
	LC	7531	1986 Jun 6	UH88	TI	1200	1.1
	K		1990 Apr 1	UKIRT	IRCAM	2640	1.1
266	V		1988 Jan 20	CFHT	RCA2	3600	0.6
	SC	7531	1986 Jun 5	UH88	TI	1200	1.3
	[OII]	8479	1986 Jun 5	UH88	TI	3600	1.2
	LC	9100	1990 May 22	UH88	NSF1	7200	1.3
	H		1990 Mar 31	UKIRT	IRCAM	4860	1.0
267	V		1990 May 21	UH88	NSF1	3600	1.1
	SC	7531	1986 Jun 7	UH88	TI	1800	1.1
	[OII]	7955	1986 Jun 7	UH88	TI	3600	1.1
	LC	8784	1986 Jun 7	UH88	TI	1800	1.1
	H		1990 Mar 25	IRTF	PCAM	8640	1.1
	H		1990 Apr 1	UKIRT	IRCAM	5400	1.2

Table 2.1: Log of Observations (continued)

3CR	Filter	$\lambda_0(\text{\AA})$	UT Date		Telescope	Device	Exposure(s)	PSF(")
280	B		1990	May 19,20	UH88	NSF1	10,800	1.0
	SC	6535	1986	Jul 2	CFHT	TI	960	1.0
	[OII]	7445	1986	Jul 2	CFHT	TI	1800	1.0
	LC	8295	1986	Jul 2	CFHT	TI	1800	1.0
	K		1990	Apr 1	UKIRT	IRCAM	3600	1.0
289	B		1990	May 19,20	UH88	NSF1	12,000	1.6
	SC	6535	1986	Jul 3	CFHT	TI	1800	1.1
	[OII]	7338	1986	Jul 3	CFHT	TI	1200	1.1
	LC	8295	1986	Jul 3	CFHT	TI	1800	1.1
	K		1990	Mar 27	IRTF	PCAM	2400	1.2
324	V		1990	May 21	UH88	NSF1	4200	0.7
	SC	7531	1986	Jul 4	CFHT	TI	1800	1.1
	[OII]	8231	1986	Jul 4	CFHT	TI	1800	1.0
	LC	8784	1986	Jul 4	CFHT	TI	2700	1.1
	H		1990	Apr 1	UKIRT	IRCAM	6720	1.3
352	B		1990	May 19,20	UH88	NSF1	10,800	1.2
	SC	6535	1986	Jun 6	UH88	TI	1800	1.5
	[OII]	6750	1986	Jun 6	UH88	TI	3600	1.6
	LC	7531	1986	Jun 6	UH88	TI	2400	1.7
	K		1990	Mar 25	IRTF	PCAM	7440	1.1
356	B		1987	May 30	CFHT	RCA2	1200	1.3
	SC	7531	1986	Jun 5	UH88	TI	2400	1.3
	[OII]	7755	1986	Jun 5	UH88	TI	3600	1.3
	LC	8784	1986	Jul 4	UH88	TI	2700	1.3
	K		1990	Mar 27	IRTF	PCAM	5040	1.3
368	B		1987	Jun 19	CFHT	RCA2	2400	1.0
	SC	7531	1986	Jul 2	CFHT	TI	1800	1.0
	[OII]	7955	1986	Jul 2	CFHT	TI	1800	1.2
	LC	8784	1986	Jul 2	CFHT	TI	2400	1.2
	H		1990	Mar 31	UKIRT	IRCAM	4200	1.3
	K		1990	Mar 27	UKIRT	IRCAM	4560	1.3

## CHAPTER 3: INFRARED AND OPTICAL MORPHOLOGIES OF $z \approx 1$ RADIO GALAXIES

### 3.1 Introduction

In this chapter we describe the results of a study undertaken to examine the optical and infrared morphologies of distant radio galaxies in a systematic way. We have used a homogeneous set of optical and infrared line and continuum images of a well-defined sample of 13 3C radio galaxies with  $0.8 < z < 1.3$  that should be *unbiased with respect to the properties of powerful radio galaxies* as found in the 3C catalog at  $z \approx 1$ . Furthermore, we have attempted to carry out a quantitative and objective analysis of the morphologies of these galaxies as a function of wavelength in order to constrain the spectral energy distributions of the various morphological components and, in particular, to determine the contribution in the infrared of the "aligned" component that dominates at short wavelengths (see, e.g. Figure 1.1). We find that the observations generally provide strong support for the basic old galaxy interpretation of high-redshift radio galaxies.

The material presented in this chapter was originally published in the *Astrophysical Journal* under the title "Infrared and Optical Morphologies of Distant Radio Galaxies" (Rigler, M.A., Lilly, S.J., Stockton, A., Hammer, F., Le Fèvre, O. 1991, *ApJ*, 385, 61). The organization of this chapter closely follows that of the paper: In the next section we briefly describe the sample, review the observations and the method of displaying the data (note that these topics have been covered in greater

detail in Chapters 1 and 2). We then present a qualitative overview of the multicolor data, drawing attention to the basic features which are explored later in the chapter. Next we develop and apply quantitative measures of the morphology at optical and infrared wavelengths, and argue that the morphologies of individual objects are consistent with the old galaxy interpretation of these objects. We then turn to examine the global correlations between various radio galaxy properties that we could expect to find within the sample. Finally, we summarize the chapter. An appendix at the end of the chapter describes significant developments concerning the radio galaxy 3C 267, based on data obtained after the paper went to press, which essentially eliminate the original confusion regarding this object. Where required to calculate sizes and luminosities, we have assumed a Hubble constant of  $H_o = 50 \text{ km s}^{-1} \text{ Mpc s}^{-1}$  and  $q_o = 0.5$ .

### 3.2 The Images

The 13 radio galaxies observed here are selected from the complete 3C sample of Laing, Riley & Longair (1983) updated with new redshifts from Spinrad et al. (1985). The radio galaxies were required to have  $0.8 < z < 1.3$ ,  $\delta < 55^\circ$ , and  $|b| > 15^\circ$ . The data set for each galaxy includes (1) a B or V-band image corresponding to a rest wavelength of about  $2500 \text{ \AA}$ , (2) a line-only [OII]  $\lambda 3727$  image, (3) two intermediate-band ( $200\text{\AA}$ ) images be located at around 4200 and 3500  $\text{\AA}$  in the rest frame, and (4) an H or K-band image corresponding to a rest wavelength of about  $1 \mu m$ .

Primary photometric and morphological analysis was carried out on  $15'' \times 15''$  subimages extracted from both the unsmoothed and the co-smoothed images and centered on the peak of the infrared emission. Montages of the unsmoothed images in each wave band for each radio galaxy are shown in Figures 3.1*a-m* (except for 3C 265, where the images are  $30''$  to a side to accommodate the very large-scale extended structure). These have been plotted with contours at *logarithmic* intervals of surface brightness (at a factor of 1.41, so that two contours represent a factor of 2 in surface brightness). It should be noted that this results in rather fewer contours than are typically represented on linear plots, but has the advantage that the relative colors and magnitudes of different components can be most easily seen. The level of the lowest contour on each plot is indicated in AB magnitudes per square arcsecond.

Those images of the radio galaxies that have equal numbers of contours thus have comparable dynamic range. The images show that, by and large, the goal of having roughly equal dynamic range in all wave bands for a given galaxy was achieved. However, the capabilities of infrared imaging on very red, quiescent objects at high redshifts is well demonstrated by our superb *H*-band image of 3C 65, which is far superior to our optical data.

Aperture magnitudes on the AB system measured through a circular  $4''$  aperture are listed in Table 2, together with the Galactic latitude and assumed  $E_{B-V}$ —usually very small. It should be noted that these are in no way meant to be "total" magnitudes, and are mainly intended to serve as the basis of the construction of spectral energy distributions over a wide baseline in wavelength. The use of isophotal magnitudes or of schemes whereby the aperture is tailored to the morphology of

individual objects would have defeated the purpose of this investigation. These magnitudes have been corrected for Galactic reddening using the  $E_{B-V}$  maps of Burstein & Heiles (1982). The AB magnitudes in the standard  $B$ ,  $V$ ,  $H$ , or  $K$  bands may be transformed back to the standard  $\alpha$  Lyrae photometric system by the addition of the following constants: 0.17, 0.00,  $-1.43$ , and  $-1.91$  for  $B$ ,  $V$ ,  $H$ , or  $K$ , respectively.

Good agreement was found between the new infrared measurements and the single-element aperture photometry of Lilly & Longair (1984). We have constructed synthetic aperture magnitudes from the two-dimensional infrared data through the same apertures used by Lilly & Longair (1984) and have compared these with the Lilly & Longair values in Figure 3.2. The rms magnitude difference is 0.26 mag, consistent with the statistical uncertainties, which are typically 20% for each data set. The uncertainty in the array magnitudes in these large synthetic apertures is dominated by uncertainty in the determination of the background level.

### 3.3 Qualitative Overview of the Morphologies

Visual inspection of the images in Figure 3.1 suggests that the infrared images are generally more compact and symmetric about the peak in the surface brightness distribution. Some of the infrared images appear almost completely round despite striking elongations at shorter wavelengths, and, given the number of contours in each image, *it is evident that this is not simply a dynamic range effect*. A particularly good example of this is given by 3C 352 (see Figure 3.1*k*). On the other hand, several objects do appear to be elongated in the infrared along the axes defined

by the shorter wavelength light. Examples of these include 3C 267, 3C 280, and 3C 324, as well as the well-studied 3C 368 (see also Chambers et al. 1988a; Djorgovski et al. 1991). Nevertheless, even in these objects, the infrared emission generally appears to be more centrally concentrated, consistent with the idea that the elongated component is simply the "tail" of the component that dominates at shorter wavelengths. For instance, careful study of 3C 324, which appears to show a convincing case of alignment, reveals that the peak of emission shifts between the optical and infrared images: the red western component is brightest at  $K$ , and the much bluer eastern component is brightest at  $B$ .

Finally, many objects show evidence of companions or extensions in the infrared in directions well away from the radio source axis. These are also visible in the longer wavelength optical continuum images around  $4000 \text{ \AA}$ , but are fainter or have disappeared in the rest-frame  $2500 \text{ \AA}$  and  $[\text{OII}] \lambda 3727$  images. We believe that these extensions and condensations represent early-type galaxy companions to the radio galaxies that have probably triggered the radio activity in a close encounter. Good examples of this phenomenon, which we discuss in more detail below, are given by 3C 265, 3C 266, and 3C 280.

### 3.4 Quantitative Morphological Analysis

A main motivation for this study was the desire to go beyond a simple qualitative description of the images and obtain quantitative measurements of the mor-

phology of the radio galaxies in order to provide a crude determination of the relative contributions of distinct morphological components in each wave band.

### 3.4.1 A Quantitative Measure of Asymmetry

It is straightforward to define a centroid, position angle and ellipticity for each image from a combination of the zeroth-, first-, and second-order moments  $\Sigma\mu$ ,  $\Sigma x\mu$ ,  $\Sigma y\mu$ ,  $\Sigma xy\mu$ ,  $\Sigma x^2\mu$ , and  $\Sigma y^2\mu$ , where  $\mu$  is the sky-subtracted surface brightness distribution of the image. These summations were carried out over a circular aperture 4" in diameter for all the images, and the derived quantities are listed in Table 3, together with the FWHM to which the images were co-smoothed. The choice of 4" diameter for the aperture used in deriving these parameters represents a trade-off between the desire to include as much as possible of the galaxy light and the increased noise and greater chance of contamination by unrelated objects. The analysis was repeated with a 6" diameter aperture, but this produced no substantial difference in the results. At these redshifts, a diameter of 4" corresponds to roughly the standard sampling radius  $\gamma$  (19.2 kpc radius) introduced by Gunn & Oke (1975) for gE galaxies. In only one case, 3C 265, is the extended structure outside the 4" aperture oriented significantly differently. It should also be noted that the 3C 356 system consists of a pair of objects separated by 4".5 along the radio axis (see below). We have listed in Table 3 the radio source position angle (measured east from north) as determined from published 5 GHz radio maps (Jenkins, Pooley, & Riley 1977 and references therein; Pedelty et al. 1989) by simply constructing a line

connecting the two radio lobes. The optical/infrared P.A. information is given relative to the radio in the sense  $\Delta P.A. = P.A.(optical) - P.A.(radio)$ . In this initial analysis, no attempt was made to remove nearby objects from the optical and infrared images unless they were clearly unrelated to the radio galaxy, as is the case with the bright star near 3C 352.

Describing these objects by a single moment parameter clearly does not do justice to their often complex morphologies. Nevertheless, we believe that it offers the best possibility for the objective assessment of the relative contributions of different morphological components at different wavelengths. As an example of possible limitations in this approach, we note that the  $V$ -band images of 3C 65 and 3C 266 have identical ellipticities (on their respective "co-smoothed" images) but quite distinct morphologies (on the unsmoothed images of Figure 3.1). This arises because of the heavy smoothing applied to the 3C 65 images which has brought the companion into the edge of the aperture used to determine the moment parameters, where it has a large effect on the second moment.

The ellipticity of the images as a function of the difference in position angle with respect to that of the radio axis,  $|\Delta P.A. |$  has been plotted for all the galaxies in the sample in Figure 3.3 in the [OII]  $\lambda 3727$  image, in the roughly  $2500 \text{ \AA}$  continuum band (observed in  $B$  or  $V$ ), and in the roughly  $1 \text{ \mu m}$  continuum band (observed in  $H$  or  $K$ ). The "alignment effect" of McCarthy et al. (1987) and Chambers et al. (1987) is clearly visible in the [OII]  $\lambda 3727$  and  $2500 \text{ \AA}$  panels of this figure. Essentially all of the radio galaxies have position angles at these wavelengths that are within  $40^\circ$  of the radio source axis, with many within  $20^\circ$ . The sole exception is the [OII]  $\lambda 3727$

image of 3C 265, which, as remarked above, shows a much closer alignment on scales outside the 4" aperture (see Figure 3.1). There is clearly also a trend for the most elongated images to be the most closely aligned with the radio axis. In contrast, the position angles determined in an identical way from the infrared images show a wide spread with regards to the radio source axis and no tendency for the more elongated images to be most preferentially aligned. *In the infrared wave band there is therefore little if any of the global "alignment effect" so strongly shown by the optical images*, at least in this well-defined sample at  $0.8 < z < 1.3$ . Examination of those infrared images which are elongated but misaligned with respect to the radio axis shows that the high values of the ellipticity parameter are generally produced by small, rather red, companion galaxies located within or on the edge of the 4" aperture. Inspection of these images shows that the main galaxy component either is round or is weakly elongated along the axis defined by the radio source and optical emission. We explore the nature of these companions more extensively below.

In order to quantify the degree of asymmetry in our images, we have used additional moment parameters. The following considerations guided our choice: (a) the aligned components are usually confined to within a few arcseconds of the nominal center of the galaxy—this being the most true in the case of those components which are most demonstrably elongated and which hence cannot be dynamically old; (b) we wanted parameters that would be as insensitive as possible to errors in the PSF used in the co-smoothing operation and to errors in the determination of the sky background level.

We therefore defined a quadrupole alignment moment,  $S = \Sigma(x'^2 - y'^2)\mu/\Sigma\mu$ . In this summation,  $x'$  and  $y'$  are transformed coordinates such that the  $x'$  is some "preferred" axis, and the  $y'$  axis is perpendicular to it. As before, the summation was carried out over a 4" diameter circular aperture centered on the peak of the infrared image. We also defined a second parameter,  $T = \Sigma(|x'| - |y'|)\mu/\Sigma\mu$ , which weights the outer parts of the images less heavily, but found no significant differences in our analysis when we employed this parameter. The remainder of our discussion is based on the  $S$ -parameter.

The parameter  $S$  is clearly zero for any circularly symmetric image and zero for an image aligned at  $45^\circ$  to the preferred axis, positive for an image aligned along the preferred axis, and negative for an image aligned orthogonally to this direction;. If an image is composed of two components A and B which individually have  $S$ -values of  $S_A$  and  $S_B$  then it is easy to show that the wavelength-dependent value of  $S(\lambda)$  for the composite image is simply given by  $S(\lambda) = f_A(\lambda)S_A + [1-f_A(\lambda)]S_B$ , where  $f_A(\lambda)$  is the fraction of the total light (within the aperture) that is contributed by the A component. Of particular interest is the case where A is a strongly aligned component whose position angle defines the preferred axis, and B is a circularly symmetric component. In this case,  $S_B = 0$ , so that  $S(\lambda) = f_A(\lambda)S_A$ .

In analyzing our images, we have arbitrarily taken the shortest wavelength continuum image (at approximately  $2500 \text{ \AA}$  in the rest frame) to define an "active" component and have determined the position angle of the preferred axis and the value of  $S_A$  from this image. Choice of the [OII]  $\lambda 3727$  image as the defining image

for  $S_A$  did not make much difference to the overall results, reflecting the fact that the 2500 Å and [OII]  $\lambda$ 3727 images are usually similar. We have assumed that the only other component present is a circularly symmetric component, taken to have  $S_B = 0$ . For each of the remaining images, we can therefore determine the relative contributions of these two morphological components by measuring  $S(\lambda)$  and thus determining  $F_A(\lambda) = S(\lambda)/S_A$ . It should be stressed that this simple morphological decomposition *may have no physical basis*. It is used to estimate the fraction of the light in the long-wavelength images (i.e., the infrared H or K images) that *must* come from a symmetric or at least un-aligned component assuming that the asymmetric component has the aligned morphology defined by the shortest wavelength image. As discussed above, this provides the most straightforward test of the idea that the K-band light is dominated by a mature relaxed galaxy, *since as one moves to longer wavelengths the value of  $S(\lambda)$  should progressively decrease toward zero*. Clearly, if the short-wavelength images themselves contain a significant contribution from the symmetric component, then the contribution of this component at longer wavelengths will also have been correspondingly underestimated.

Once  $f_A(\lambda)$  and the overall spectral energy distribution within the aperture is determined for a given galaxy as a function of wavelength, it is straightforward to produce spectral energy distributions for the aligned and symmetric components separately, as defined by the moment analysis. It should be stressed again that these may not be physically meaningful: in particular, our method of analysis sets the flux density of the symmetric component to zero at the shortest wavelengths. However,

these curves will serve to illustrate how the aligned parts of the galaxies are bluer than the central symmetric parts.

The individual measurements of  $S_A$  and  $S(\lambda)$  are of course dependent on the point-spread function, being smaller for more highly smoothed images. However, provided that the seeing is the same for all the images of a particular galaxy, as we have attempted to ensure through the co-smoothing operation, the ratio,  $f_A$ , should be unaffected. This has been verified using different smoothings of the two-component model galaxies discussed in section 1. The value of  $S_A$  for the linear component in the model varies as (30.4, 24.8, 21.0, 19.1) for seeing of (0.5", 1.0", 1.5", 2.0"), but the corresponding values of  $f_A$  are almost constant at (0.206, 0.200, 0.197, 0.196). If an error in the co-smoothing process resulted in a discrepancy of 20% in the effective seeing for the different images, this would, however, translate to an error of 10% in the value of  $f_A$ .

We have estimated the statistical uncertainties in the derived values of  $f_A(\lambda)$  in two ways. First, we have constructed a suite of simulated galaxies using the de Vaucouleurs galaxy model with a linear active component that was describe in section 1 with  $f_A = 0.2$ . To these we have added noise with the approximate characteristics of the noise encountered in our actual images (see selected examples in Figure 1.1, *lower panel*). From the simulated data, we find an rms error in  $f_A$  of 0.1, and find that this is largely independent of the amount of smoothing applied to the image (over the range 0.5" to 2.0"). Second, we have examined the moment parameters derived from multiple images that are available for some objects, and find that

these agree to within about 0.1 in  $f_A$ . For simplicity we take 0.1 as a reasonable estimate of the uncertainty of  $f_A$ . In passing, the uncertainty in the position-angle determination of the  $f_A = 0.2$  model (representative of our infrared data) was  $5^\circ$  for 1" seeing and about  $10^\circ$  for 2" seeing, but would be larger for objects with and even smaller contribution from the aligned component. This may account for some of the spread of P.A. measurements in the infrared seen in Figure 3.3, but we suspect that the dominant effect is that of nearby companions at "random" relative P.A.

The morphological decomposition obviously works best for (a) those objects that are most elongated and "aligned" so that  $S_A$  is large and small random errors do not dominate the change of morphology with wavelength, and (b) those which do not have bright nearby companions that may distort the  $S(\lambda)$  values as a function of wavelength if the radio galaxy and companion have different spectral energy distributions. We have carried out this morphological decomposition analysis for 3C 65, 3C 265, 3C 280, 3C 324, and 3C 352. The values of  $S(\lambda)$  and  $F_A(\lambda)$  as a function of wavelength for these five galaxies are listed in Table 4, and the resulting two-component spectral energy distributions are shown in Figures 3.4a-e. The remaining galaxies are less suited to this detailed individual analysis, usually because a bright infrared companion is producing an orthogonal alignment in the infrared and hence formally a negative value of  $f_A(\lambda)$ , or because the images are almost round in all wave bands, so that the small uncertainties dominate the variation in  $f_A(\lambda)$ .

These spectral energy distributions (SEDs) clearly demonstrate that in these objects, *a substantial symmetric component must be added to the short-wavelength*

*images in order to match the observed morphologies in the infrared.* This is of course exactly the result expected from the model in which all of these galaxies, regardless of their overall color, contain a mature massive galaxy that dominates the light at infrared wavelengths. For the five galaxies for which this detailed analysis was possible, the average contribution of the asymmetric "aligned" component to the infrared light is about 8%.

Mindful of the arbitrary and nonunique nature of the morphological decomposition, the SEDs in Figure 3.4 *suggest* that the active "aligned" component has a spectral energy distribution that is usually roughly flat,  $f_\nu = k\nu^0$  to  $k\nu^{-1}$ , over the 2500 Å to 1 μm interval, and *suggest* that the symmetric components may have a spectral energy distribution that is broadly similar to those of present-day gE galaxies. In order to aid the eye, we have sketched in by hand a smooth curve to represent the SED of the aligned component. A more sophisticated approach is not warranted, on account of the crudity of the morphological analysis. We note in passing that several objects (most notably 3C 280 and 3C 324) exhibit a turn-down in the overall SED. A broadly flat SED in  $f_\nu$  is consistent with both a young starburst (e.g., Bruzual 1983) and the scattered light from an anisotropically emitting quasar nucleus.

On a more speculative note, we notice that the reddest "aligned" component in Figure 3.4 is that of 3C 352, which has a conspicuous misalignment with respect to the radio axis in Figure 3.1. If star formation is responsible for the blue aligned component, this could reflect an aging effect as the jet processes to new orientations. This idea receives some support from the fact that the other radio galaxies appear to

have infrared extensions at slightly different P.A.s to the far-ultraviolet light (e.g., 3C 267, 3C 280, and 3C 324).

The effects of companions, etc., that led us not to analyze the remaining eight objects individually should, however, cancel out within the sample as a whole. We have therefore plotted in Figure 3.5 the values of  $S_A$  (defined as before from the shortest wavelength image) and  $S$  for the infrared image for *all* the galaxies in the sample. It may be seen that, as expected,  $S(\lambda)$  in the infrared is generally much smaller than  $S_A$ . Taking a simple average, it is found that  $\langle S(1\mu m) \rangle = 0.20 \langle S_A \rangle$ . The mean may be largely affected by extreme objects like 3C 368 (which may itself be contaminated by an M star—see below) and 3C 266 (which has a large red companion located orthogonally to the radio axis), so we have calculated the ratio of medians. It is lower, at 0.08.

We conclude that in essentially all objects, the infrared alignments that are seen in this sample are consistent with being produced by the long-wavelength tail of the aligned component (with a roughly flat spectral energy distribution) that dominates at shorter wavelengths. We turn now to examine in detail those objects which show the strongest apparent alignments on Figure 3.5, with  $S(\lambda)$  at  $1\mu m$  comparable to  $S_A$  at  $2500\text{ \AA}$  on Figure 3.5. Principle among these are 3C 217, 3C 267, and the well-known case of 3C 368 observed by Chambers et al. (1988a) and Djorgovski et al. (1991). We review these cases in turn, along with 3C 356, which has been discussed both by Eales & Rawlings (1990) and by Eisenhardt & Chokshi (1990).

### 3.4.1.1 The Galaxy 3C 217

The galaxy 3C 217 is an extremely active object. It has the second bluest 2500 Å to 1 μm color and the highest equivalent width of [OII] λ 3727 in our sample. Its overall color is as blue as that of an Irr galaxy. The 2500 Å and [OII] λ 3727 images are similar and show an elongated "football-shaped" structure symmetric about the peak and aligned at approximately 25° from the radio axis of this asymmetric and rather distorted double. Given the very blue color, a substantial contamination from the ultraviolet component would have been expected in the infrared. In fact, examination of the infrared (equal to the moment at 2500 Å) is actually caused by a secondary peak located at the same position angle but slightly beyond the extent of the ultraviolet images (this component is seen in the 4100 Å image, so is definitely real). Within the area of the ultraviolet "football," the infrared image is actually quite symmetric.

It is tempting to identify this secondary red peak as a companion object, particularly since the alignment with the radio axis is not particularly good. The peak is about the same distance from the nucleus as the hot spot, but at about 30° relative position angle (a displacement of 2.4") from it. As mentioned above and discussed in more detail below, we find many similar red companion candidates in other objects with a wide range of position angles.

In short, we believe that the multicolor morphology of 3C 217 is consistent with the two-component old galaxy interpretation, despite the apparent similarity of the moment parameters as determined in the optical and in the infrared.

### 3.4.1.2 The Galaxy 3C 267

Originally, the object 3C 267 was the most problematic in our sample. It is the faintest object in the infrared and one of the faintest in the optical. Our original data in all wave bands were thus of lower quality than for the other objects in the sample. Its own faintness in the infrared and the lack of any brighter objects nearby precluded our usual checks of the coregistration process, which led to difficulties in interpreting the optical and infrared morphologies. After the paper went to press, a superior infrared image was obtained by the author using the UH/NICMOS-3 array at the UH 2.2 m telescope. The new image, which clears up the confusion, is presented in the appendix to this chapter.

### 3.4.1.3 The Galaxy 3C 368

The object 3C 368 was the first high-redshift radio galaxy to be imaged in the infrared (Chambers et al. 1988a), and the "infrared alignment" seen in this object stimulated much of the theoretical work discussed in Section 1, on the expectation that this was a typical object. In fact, 3C 368 is extreme in its color (it is the bluest in the sample) and [OII]  $\lambda$  3727 line strength. It also provides the most striking example of the alignment effect at optical wavelengths, and some degree of alignment in the infrared is consequently not unexpected. An improved infrared image has been published by Djorgovski et al. (1991). A polarization map at optical wavelengths has recently been published by Scarrot et al. (1990).

It is by now clear that 3C 368 is actually a considerably more complex system than the other radio galaxies in the sample. Hammer et al. (1991) have suggested that the brightest component is a foreground object and have tentatively identified this as a Galactic M star on the basis of optical spectroscopy at high spatial resolution. Analysis of the present multicolor data supports this idea in the following way.

In describing the components of 3C 368 (see Figure 3.6), we follow as much as possible the nomenclature of Hammer et al. (1991), making reference also to that of Djorgovski et al. (1991). The small-aperture colors of various components of the 3C 368 system were measured from the co-smoothed images. Aperture colors in a 1" aperture were measured for the bright central component, "a," for two locations at the local peaks in the rest-frame 2500 Å and [OII] λ 3727 images found to the north and south ("b" and "c"), and for a point midway between "a" and "b," which we have called "G." Our "G" position is thus slightly to the north of the central peak in [OII] λ 3727 (i.e., component "e" of Hammer et al. 1991), which is probably identified with the radio core component. We have also measured the colors through 2" apertures of other objects in the field, including the faint star "comp" (again following Hammer et al. 1991), which is 6" south of "a," and the objects "T" and "R" (the latter following Djorgovski et al. 1991), which lie 2" northeast and 3" north, respectively, of "b." Our "a" component is Djorgovski et al.'s (1991) "Q"; our "b" is their "A"; and our "G" must be close to their "K."

These colors have been plotted on a two-color  $(B-I)_{AB}/(I-K)_{AB}$  diagram (Figure 3.7), converting the "long continuum" image to the I band and applying

reddening corrections to all objects. Because of the very long baseline in wavelength, this diagram is a powerful discriminant between Galactic stars and composite stellar systems, especially when the latter lie at high redshifts (see, e.g., Cowie et al. 1990). The figure shows a locus of Galactic stars, of power-law continua, and of Irr, Sbc, and E galaxies at redshifts  $0.0 < z < 2.0$ . Most of the objects in the field are Galactic stars, and they lie close to the expected track in this diagram. From its location on the diagram, the unrelated southern object "comp" is almost certainly a K7-M1 Galactic star, as was suggested from spectroscopic data by Hammer et al. (1991).

Of the components of the 3C 368 system itself, the northern and southern components ("b" and "c") and the central location ("G") have the colors of blue stellar systems at high redshifts ( $z > 1$ ). Components "b" and "c" have a flat spectral energy distribution between B and I and a gentle rise up to K. This is the signature of an extremely young starburst population (see, e.g., Bruzual 1983). The central component "G" is redder, more like an Irr galaxy at this redshift. The northernmost component "R" is also likely to be a stellar system at  $z = 1.1$ . It is significantly redder than the main components "b," "c," and "g," and appears to have the colors of an Sbc galaxy. In marked contrast to these components, the bright central component "a" (and also the fainter northeastern object "T") lie squarely on the "stellar" locus of the M star "comp." Some admixture from an underlying high-redshift component, presumably with colors similar to those of "G," has probably pulled the position of this component down a little on the figure. It should be noted that "a" does not have a power-law spectral energy distribution. Djorgovski et al. (1991) associated this

component (their "Q") with the radio core and identified it as an obscured quasar nucleus.

We take this analysis to provide important support for the identification of the brightest component "a" in the 3C 368 system as a foreground Galactic star. This will make the underlying galaxy somewhat bluer in  $(B-K)$ . Note, however, that even in this extremely blue object, the central regions (i.e., "G") appear to be redder than the outermost parts "b" and "c," as expected from the old galaxy hypothesis and as found in the other objects in the sample.

We have estimated the contribution of the central star to the overall spectral energy distribution of 3C 368 as follows. The ratio of the peak surface brightnesses of component "a" and star "comp" is 3.0 in H and 3.3 in K, with the difference probably reflecting the greater contribution of the underlying galaxy in K (see Figure 3.6). We can thus take 3.0 times the flux of the star in H and K [thus assuming that the contaminating star has the same  $(H-K)$  color as the star "comp"—a reasonable assumption within the accuracy of this exercise, since  $(H-K)$  changes little with spectral type] as upper limits to the contribution of the interloping star in 3C 368. The star has  $K_{AB} = 21.1$  in a 4" aperture. This causes the K-magnitude of the real 3C 368 to become 0.75 mag fainter. If we, less justifiably, assume that the spectral energy distributions of the two stars are the same down to B, then we can estimate the contamination over the whole wavelength range. We find a contamination of 50% at K, 75% at I, and 17% in B. The  $(B-K)_{AB}$  color of the galaxy changes from 1.4 to 0.84. Henceforth we will use both the raw and "decontaminated" colors in the discussion to follow.

Clearly the infrared image of 3C 368 is aligned with the radio and optical axes even if the foreground star is removed. However, within the context of the old galaxy hypothesis, this object is so blue (regardless of whether the original or corrected colors are used) that the aligned component may completely swamp the underlying old component and an arbitrarily large amount of infrared alignment is "acceptable." We noted above, however, that the central regions "G" do appear to be redder than the outer parts "b" and "c," even in this extreme object.

#### **3.4.1.4 The Galaxy 3C 356**

The situation with 3C 356 is confusing. Two comparably bright objects lie on the radio axis. The object is thus unique within our sample. There is disagreement in the literature as to the location of the active nucleus: Eisenhardt & Chokshi (1990) considered the northern object to be the radio galaxy host and quoted the position of a central radio core (R.A. Laing 1990, private communication) to support this identification. In contrast, Eales & Rawlings (1990) also quoted a private communication from Laing of a core component co-located with the southern object. We have taken the northern object to be the radio galaxy on account of its higher ionization spectrum.

Our infrared image is similar to that of Eisenhardt & Chokshi (1990). The northern object is compact and almost unresolved. The southern object is more extended and diffuse. While aligned along the radio axis with respect to the northern

object, it is itself slightly elongated along a roughly perpendicular direction in the infrared (see Figure 3.1).

Our view on 3C 356 is that while both components unarguably *lie on* the radio axis, neither shows evidence in the infrared for *elongation along* that axis. Individually, therefore, neither shows evidence for infrared light that *must* come from a dynamically young component, and hence both could be composed of old stars. Our guess is that the southern component may be a companion galaxy that has wandered into the jet path.

We conclude that all of the radio galaxies in the sample have individual morphologies at infrared wavelengths that are fully consistent with the idea that the light is dominated by a symmetric component, which plausibly has a spectral energy distribution similar to that of a gE galaxy, with only modest contamination from the long-wavelength tail of a much bluer, roughly "flat-spectrum," component that is aligned with the radio axis.

It should be stressed that this analysis does not prove that the symmetric component is an extended mature galaxy. For instance, a compact quasar nucleus would have produced the same morphological result. However, given the original argument based on the small dispersion in the K-z relation, a gE host galaxy is the most plausible identification for this component. We believe that this analysis does prove that, for this sample (i.e., 3C radio galaxies at  $0.8 < z < 1.3$ ), morphological arguments *against* the old galaxy hypothesis based on the alignment of the infrared images (Chambers et al. 1988a; Eisenhardt & Chokshi 1990) are incorrect.

### 3.5 Sizes of the Galaxies

If the red/visual light is dominated by the starlight from the old elliptical-like host galaxy, then the characteristic scale length of this light may provide constraints on the dynamical evolution of massive galaxies and/or the cosmological geometry.

With the exception of our CFHT image of 3C 65 obtained with the large-format  $256 \times 256$  array, our data are not ideally suited to such an investigation because of (a) the large pixel size of the data (up to 0.6") (b) the indifferent image quality (typical FWHM  $\approx 1.0''$ - $1.3''$ ); (c) subtle ghosting effects introduced by the median flat-fielding process. The latter arises because the median filter does not completely eliminate ghosting effects introduced by the median flat-fielding process. The latter arises because the median filter does not completely eliminate the effects of objects (and in particular the radio galaxy itself) in the frames used to construct the background image. This effect is most serious in the IRTF data, where the spatial separation of the positions in the mosaic is small. A thorough treatment of these effects to yield precise scale sizes for these images is beyond the scope of this chapter, and is probably impossible.

As part of the work presented in this chapter, the sizes of the radio galaxy images were analyzed only to the extent of satisfying ourselves that they were consistent with the old galaxy hypothesis. The radius  $r_{0.25}$  at which the Petrosian function  $\eta(r)$  (defined as the surface brightness at some radius divided by the average surface brightness within that radius) falls to 0.25 was determined (cf. Djorgovski & Spinrad 1981). A value of  $\eta = 0.25$  corresponds to a value of the Gunn-Oke struc-

ture parameter  $a$  (Gunn & Oke 1975) of  $\alpha = 0.50$ . This is a convenient value to choose, since Lilly & Prestage (1987) measured  $\alpha$  at 19.2 kpc radius for a sample of 23 radio galaxies with  $z < 0.1$  and found  $\langle \alpha \rangle = 0.5$ . We would therefore expect the radio galaxies to have  $\langle r_{0.25} \rangle$  in the range  $2'' < r_{0.25} < 3''$  for  $0.05 < q_o < 0.5$ . The radio galaxies observed with UKIRT and CFHT span an (uncorrected) range  $1.7 < r_{0.25} < 3.3$ . Correction for seeing effects reduces the sizes of the smaller galaxies to around 1.3. The extended light associated with the blue aligned components would also tend to increase the effective sizes of the galaxies.

These sizes are thus consistent with the known sizes of the giant elliptical galaxies associated with powerful radio sources at low redshifts, to within the limitations of our data. This topic is explored much more thoroughly in Chapter 4 of this dissertation, where we present detailed measurements of the scale sizes of images taken with NICMOS-3 array, which are of extremely high quality and do not suffer from the median ghosting effect described above.

### 3.6 Red Companion Galaxies

One of the most striking features of our infrared data is the large number of relatively red objects that are found close to a large fraction of the radio galaxies, and which are likely to be companion galaxies. These possible companions are generally more prominent on our infrared images than at shorter wavelengths, at least in part because the strong alignment of the radio galaxy continuum is weaker or absent in the infrared. In some cases, they are responsible for the high ellipticities meas-

ured in the infrared, especially when the derived position angles are grossly misaligned with radio source axes. Particularly good examples are provided by 3C 217, 3C 265, 3C 266, 3C 280, and 3C 368 (over a third of the sample observed here). We have identified these objects on Figure 3.1 with the letter "C." It should be noted that we have excluded blue continuum regions, especially when located along the radio axis, since these are likely to be part of the "alignment effect" (see, e.g., the many blue knots in 3C 265 and the blue companion to 3C 65). Companions may also be present in several other objects, such as 3C 324 and 3C 352, but these are less compelling, with the neighbor in question being farther away (3C 352) or not particularly red (3C 324). The properties of the most likely companion objects are summarized in Table 5.

In many cases these possible companions are distinctly redder than the radio galaxy itself when viewed over the full  $2500 \text{ \AA}$  to  $1 \mu m$  range. As well as being prominent in the infrared, they are seen on the "long continuum" images (just above the  $4000 \text{ \AA}$  break) and are thus undoubtedly "real" objects. They are usually noticeably fainter in the "short continuum" images (at roughly  $3500 \text{ \AA}$ ) and are frequently absent at  $2500 \text{ \AA}$  and in the  $[\text{OII}] \lambda 3727$  emission line.

We have crudely estimated the relative magnitudes of the radio galaxies and the possible companions in the infrared by simply comparing their peak surface brightnesses. It is found that the companions range from 1.0-2.5 mag fainter than the radio galaxies and are located 2.0"-4.5" (of order 20-45 kpc) away and span a wide range of position angles relative to the radio axis, with two at  $80^\circ$  relative P.A. Any companions that are significantly fainter, or are either closer to or farther away

from the radio galaxy, would probably have been missed. It is possible that asymmetries in the infrared images of some other objects (e.g., 3C 226) may be caused by closer companions that we have been unable to resolve. It is also possible that the relatively large southern object in the 3C 356 system could be viewed as a "companion," although, as discussed above, it does lie on the radio axis.

Down to  $K = 19$ , there are 40,000 objects per square degree (Cowie et al. 1990), giving an average separation to random field objects of approximately 10". We have not considered objects more than 5" away to be "companions," so most of the claimed companions should be real. 3C 266 is behind Abell 1374 at  $z \approx 0.2$ , so a higher density of foreground objects might be expected in this case. However, objects at such low redshifts would be relatively blue.

Within our small sample, we find that the radio galaxies with the best examples of nearby red companions that are clearly *not* associated with the alignment effect (i.e., the five galaxies named above) are preferentially the bluest systems with the more striking optical alignment effects. A Mann-Whitney test indicates that this difference is significant at the 99.5% level.

Close interactions with companions have been proposed as the trigger source for quasar, Seyfert, and starburst activity for some time (Toomre & Toomre 1972; Adams 1977; Stockton 1982; Hutchings et al. 1981), and there is a considerable body of evidence to support this idea (Sanders et al. 1988; Stockton 1990; Heckman 1990). Even gas-poor companions can disrupt the central galaxy and funnel gas into the central regions. It is therefore not too surprising that we find companions around these very powerful radio galaxies. Their significance in the context of this chapter

rest on two indirect arguments that they provide against Chambers & Charlot's (1990) scenario in which some of the  $z \approx 1$  radio galaxies are very young and are being formed by the radio activity itself.

First, it suggests that the radio activity is still being triggered in the  $z = 1$  systems through mechanisms similar to those which operate in the present-day Universe. If, as has been suggested (Chambers & Charlot 1990), some of these radio sources are truly dynamically young systems, and if young radio sources are indeed themselves responsible for the formation of much of the stellar populations in the host galaxies, then one might have expected to find quite different triggering mechanisms in operation. Second, the fact that these companions are usually redder than the radio galaxy suggests that some "old" galaxies, of lower but still comparable mass, have existed around the site of the radio galaxy for some time, presumably in the small group or cluster. This makes the presence of an old population in the main radio galaxy itself appear very natural.

### **3.7 Global Correlations with Color**

The preceding quantitative examination of the morphologies of individual objects has provided important support for the hypothesis that these radio galaxies contain a luminous red elliptical-like galaxy plus varying amounts of a blue extended and "aligned" active component. The infrared images are more compact than the optical images, showing weaker alignments with the radio axes. Those alignments

that are seen in the infrared are explicable in terms of the infrared tail of a roughly flat-spectrum component that dominates in the ultraviolet.

In this section, we examine the global correlations with the overall 2500 Å to 1 μm color that would be expected in this picture in various parameters, the point being that the color should reflect the level of activity in each object. Curiously, we find that these correlations are not as compelling as we would have expected from the individual morphologies, although the statistical significance within this small sample is low.

We have constructed the 2500 Å to 1 μm color from our spectral energy distributions by interpolating or by using an extrapolations based on the empirical colors. As a true color, this parameter is uncertain at the 0.2 mag level, but it enables us to compare galaxies at different redshifts as consistently as possible.

### 3.7.1 The Color-Magnitude Relation

A correlation between color and luminosity would be expected, since the bluer objects should have a greater contribution, at all wavelengths, from the active aligned component. Such a correlation is indeed seen in the optical wave band as shown in Figure 3.8a, where we have plotted the absolute magnitude at 2500 Å against the overall 2500 Å to 1 μm color.

Although diluted by the uniform red component dominating at infrared wavelengths, a residual of this correlation should be apparent in the infrared, unless the active component has an extremely blue color. If the aligned active component

had a uniformly flat spectral energy distribution in all objects, then an increase in luminosity at  $1\ \mu m$  of about 0.5 mag would be expected over the full 3 mag range of color present in the sample. This is shown in Figure 3.8*b*. A redder active component would produce a larger effect in the infrared. To eliminate this expected correlation between color and magnitude entirely would of course require an infinitely blue active component, a possibility that can be ruled out because some residual alignment is seen in the infrared, indicating that some fraction of the infrared light is indeed produced from the aligned component.

A straightforward linear least-squares fit to these data produces an inverse correlation. This is driven by 3C 217, which is one of the bluest but faintest galaxies in the sample, and by 3C 65, which is the reddest and brightest! The remaining galaxies do show a trend in the desired sense, although it should be remembered that 3C 368, the second bluest objects, may well be about 0.75 mag fainter if it is contaminated by a foreground object (see above).

Four possibilities present themselves. First, the observations could be in error for 3C 65 and 3C 217. This is very unlikely. The infrared photometry agrees well with the Lilly & Longair (1984) measurements, and in the case of 3C 217 there is good agreement in the present study between independent IRTF and UKIRT measurements. There are also independent reasons to think 3C 65 to be red and 3C 217 to be blue, in that these objects have the smallest and greatest equivalent widths for [OII]  $\lambda 3727$  in the sample.

Second, 3C 65 and 3C 217 may be statistical flukes within a small sample. This is still quite reasonable. A Pearson rank test gives only a very low correlation

coefficient ( $r_S = 0.07$ ), indicating that there is an 80% chance that the observed distribution comes from an *uncorrelated* distribution. While a weak correlation in the opposite sense would have been expected, the chance of observing the observed distribution is still presumably reasonably high. This possible explanation can of course be tested with a larger sample. Until such a larger sample is studied, this explanation for the form of Figure 3.8*b* is our preferred one.

Third, 3C 65 and 3C 217 may represent different physical situations where the standard old galaxy picture would not apply. The galaxy 3C 217, for example, could represent a new class of subluminoous radio galaxies. We are naturally unwilling to advocate such an unattractive interpretation at this stage. The object 3C 65 could have a red non-stellar nucleus. A strong nuclear component seems unlikely because the emission lines are relatively weak. The morphological analysis presented in Chapter 4, however, suggests that a nuclear component might be present with a modest flux of  $\approx 10\%$  the total galaxy flux in the H-band.

Finally, the diagram could represent the true situation in which there is an inverse correlation between color and luminosity, in the sense that the reddest objects are brighter. Within the context of the old-galaxy interpretation, this would require that the strength of the active component was in some way related to the mass of the galaxy. It is possible to envisage a scenario in which more massive galaxies get rid of their gas at earlier times, so that the most vigorous jet-induced star formation at  $z = 1$  occurred in lower mass systems. In this sense the small dispersion in the  $K-z$  relation would be at some level a coincidence: the true dispersion in the  $K$ -magnitudes of the underlying galaxies would actually be larger, with the fainter

members being boosted by the additional active component. This option is similarly unattractive.

We note in passing that alternative models in which there is a wide range of ages (e.g., the Chambers & Charlot 1990 model) also predict a correlation between color and luminosity in the sense that the brighter objects should be bluer.

### 3.7.2 Elongation as a Function of Color

In the simple model where a blue aligned component is added to a red symmetric galaxy, it would be expected that the alignment effects would be most apparent in the bluest objects, since these will have the largest contribution from the blue aligned component. Of course, some blue objects may be symmetrical if the active component is itself not elongated, and a variation in spectral index of the aligned component may further dilute any correlation, but red objects would not be expected to show strong alignments. Such an overall trend was demonstrated by Lilly (1989), who showed that the optically most aligned objects in the original McCarthy et al. (1987) sample had the bluest colors in (r-K). Furthermore, the very red "1 jansky" identifications presented by Lilly (1989) showed virtually no alignment effect even at very short wavelengths.

In Figure 3.9a we have plotted the  $S_A$  parameter, defined at roughly  $2500 \text{ \AA}$ , against the overall rest-frame ( $2500 \text{ \AA}$  to  $1 \mu m$ ) color for the sample of objects studied here. The most aligned objects, 3C 368, 3C 267, 3C 280, and 3C 324, all have

colors 1.5 mag bluer than the reddest, and much more symmetrical, radio galaxy 3C 65.

To look directly at this effect in the infrared, we have plotted in Figure 3.9*b* the value of  $S(1\mu m)$  measured in the infrared (with the preferred axis again being defined by the short-wavelength images) against the overall color. A more confusing diagram results, partly because of the relatively large elongation of the "misaligned" 3C 266 (recall that this was due to a red companion lying perpendicular to the radio axis) and the anomalously high elongation of 3C 267. The remaining objects have a distribution similar to that in Figure 3.9*a*, in that there are no very red, very aligned objects, although it is again striking in this figure how much smaller the infrared moments are relative to the optical ones.

### 3.8 The Aligned Component

The actual nature of the active, aligned component has not been important for most of the foregoing discussion in this chapter, which has been concerned primarily with establishing the presence of a central symmetric red component in these galaxies. We are presently analyzing our images with a view to trying to understand the nature of the active component, and some of our preliminary conclusions are presented in Chapter 5 of this dissertation. Nevertheless, in this section we present a few general comments concerning the alignment effect that have struck us in our initial examination of the images, bearing in mind that this is the first complete and statistically well-defined sample to be subjected to systematic scrutiny.

First, the "alignment effect" is by no means perfect. Many striking elongated objects have position angles that are displaced from the radio axis by several tens of degrees. The spread in relative position angles displayed in the upper two panels of Figure 3.3 is certainly not measurement error, as cursory examination of 3C 352 reveals.

Second, we note that the distribution of 2500 Å continuum and [OII] λ3727 emission-line gas are often strikingly similar. Indeed, we initially used the [OII] λ3727 image to define the "active" component, before deciding that the 2500 Å was the more logical choice. The results changed very little when this change was made, as is seen by comparing the values of  $S$  for the 2500 Å continuum and [OII] λ3727 images listed in Table 3.

Finally, we note that the "quality" of the alignment (meaning the degree of elongation *and* the relative position angle) depends strongly on the size of the radio source. The objects 3C 266, 3C 324, and 3C 368 are all small double sources with separations of 10" or smaller (roughly 90 kpc at  $z \approx 1$ ). This trend is shown in Figure 3.10, where we have plotted the short-wavelength  $S_A$  parameter against the projected radio separation (note that the  $S_A$  parameter of 3C 267 is overestimated in this figure; see Appendix A). We have plotted both  $S_A$  and  $S_A \times \cos 2\theta$ , where  $\theta$  is the misalignment angle between the optical and radio axes. McCarthy et al. (1990) have already noted that the elongated components are frequently one-sided and in these cases appear always to lie toward the nearer radio lobe.

### 3.9 Summary

Qualitative and quantitative analysis of a homogeneous set of multicolor line and continuum images of a complete sample of 3C radio galaxies at  $0.8 < z < 1.3$  has led us to the following conclusions:

1. The infrared morphologies are much more symmetric than those at optical wavelengths. Although several of the infrared images are aligned with the radio axes, quantitative measures of the asymmetry show a progressive *reduction* as one goes from rest-frame  $2500 \text{ \AA}$  to  $1 \mu m$ , as is to be expected if a symmetric component increasingly dominates at the longer wavelengths. This is consistent with the "old galaxy hypothesis" for these galaxies, whereby the small scatter in the  $K-z$  relation is produced by a homogeneous population of mature host galaxies.

2. A spectral decomposition based on these quantitative morphological parameters strongly suggests that the "active" component, which dominates in the ultraviolet wave band and is usually roughly aligned with the radio source axis, has a roughly flat spectral energy distribution in  $f_\nu$ , between  $2500 \text{ \AA}$  and  $1 \mu m$ . Similarly, the data are consistent with the "symmetric" component having a red spectral energy distribution similar to that of a gE galaxy, although the spectral decomposition is not unique.

3. Typical 3C radio galaxies at  $z = 1$  probably have about 10% of their rest-frame  $1 \mu m$  light produced by the active component. The more active objects have larger contributions. Nevertheless, these modest contaminating components are

insufficient to perturb either the scatter or the continuity of the observed  $K-z$  relation.

4. The angular sizes of the infrared images of the radio galaxies are consistent with the known sizes of the giant elliptical galaxies associated with powerful radio sources at low redshifts for reasonable cosmologies, i.e.,  $0.05 < q_o < 0.5$ .

5. A significant fraction (5/13) of these radio galaxies are accompanied by possible nearby red companion galaxies that are prominent on the infrared images. These are 1-2 mag fainter than the main galaxy, but are usually redder in overall color and usually have little or no associated [OII] emission. The presence of the red companions would suggest that "conventional" triggers for the radio sources are still operating at  $z > 1$ , and that, regardless of the evolutionary state of the radio galaxy, at least some old galaxies exist around the central object.

6. Photometric analysis of the components of the complex object 3C 368 supports the view that the brightest component is a foreground Galactic M star.

7. While there is a strong correlation between the overall color and absolute magnitude at short wavelengths, there is little evidence for the expected correlation between color and absolute magnitude in the infrared, although our sample is small and, given the intrinsic scatter expected, the statistics are poor.

8. As expected, the most aligned objects are the ones with the bluest overall colors, since these have the strongest active components. These objects also have the smallest projected radio separations.

Viewed as a whole, the results of this morphological study are consistent with the infrared morphologies being dominated by a round symmetric component, and give support to the idea that these radio galaxies form a homogeneous population of mature gE-type galaxies undergoing, to various degrees, bursts of star formation associated with the radio source activity, as originally proposed by Lilly & Longair (1984) and further refined by Lilly (1989) to explain the small scatter in the  $K-z$  relation and the large range of optical-infrared colors. It must be remembered, however, that the spectral decompositions presented here are by no means unique. The strongest statement that can be made with certainty is that the appearance of aligned morphologies does not, in and of itself, necessarily imply young ages. Thus, the evolutionary status of these and other radio galaxies remains an open and important question.

## Appendix A: An Improved Infrared Image of 3C 267

In the analysis presented in the original paper, the galaxy 3C 267 was the most problematic in the sample because the infrared emission appeared elongated and roughly aligned with both the radio source axis and the aligned optical emission. Unfortunately, the original set of images for this object was of poorer quality than for all the other objects in the sample, and the lack of available field objects precluded an accurate coregistration of the optical and infrared images.

On 1991 May 30 the author obtained an improved infrared image of 3C 267 using the NICMOS3 ( $256 \times 256$ ) device at CFHT. The high resolution and large field of view of this image enabled an extremely accurate coregistration with the optical data, and also confirmed that this galaxy has fairly blue optical to infrared color. The  $15 \times 15''$  K' band and V band images are shown in Figure 3.11. With the improved coregistration it is evident that, while the infrared morphology is indeed elongated, it makes an angle of  $30^\circ$  with the radio axis and it does not coincide exactly with the aligned optical emission. Rather, the surface brightness distribution of the infrared emission is peaked at its southwest end, at a point coinciding with the northeast end of the aligned optical emission. The morphological components of the system can be simply interpreted as an evolved host galaxy centered at the infrared peak, with a red (non-aligned) extension to the north that is possibly due to unresolved companions, and a flat-spectrum aligned component that extends along the southwestern radio axis. The optical and infrared morphologies of the galaxy 3C 267 are therefore not unusual compared to the others in the sample.

### References for Chapter 3

- Adams, T.A. 1977, *ApJS*, **33**, 19
- Bruzual, A.G. 1983, *ApJ*, **273**, 105
- Burstein, D., & Heiles, C. 1982, *AJ*, **87**, 1165
- Chambers, K.C., & Charlot, S. 1990, *ApJ*, **348**, L1
- Chambers, K.C., Miley, G., & Joyce, R.R. 1988a, *ApJ*, **329**, L75
- Chambers, K.C., Miley, G., & van Breugel, W. 1987, *Nature*, **329**, 609
- Coleman, G.D., Wu, C-C., & Weedman, D.W. 1980, *ApJS*, **43**, 393
- Cowie, L.L., Gardner, J.P., Lilly, S.J., & McLean, I.S. 1990, *ApJ*, **360**, L1
- Djorgovski, S., & Spinrad, H. 1981, *ApJ*, **251**, 417
- Djorgovski, S., Wier, N., Matthews, K., & Graham, J. 1991, in *ASP Conf. Ser.* 14, with *Infrared Arrays*, ed. R. Elston (San Francisco: ASP), 112
- Eales, S.A., & Rawlings, S. 1990, *MNRAS*, **243**, 1P
- Eisenhardt, P., & Chokshi, A. 1990, *ApJ*, **351**, L9
- Gunn, J.E., & Oke, J.B. 1975, *ApJ*, **195**, 255
- Hammer, F., & Le Fèvre, O., Proust, D. 1991, *ApJ*, **374**, 91
- Heckman, T.M. 1990, in *IAU Colloq. 124, Paired and Interacting Galaxies*, ed. J.W. Sulentic (NASA CP-3098), 359
- Hutchings, J.B., Crampton, D., Campbell, B., & Pritchett, C. 1981, *ApJ*, **274**, 743
- Jenkins, C.J., Pooley, G.G., & Riley, J.M. 1977, *MNRAS*, **84**, 61
- Laing, R.A., Riley, J.M., & Longair, M.S. 1983, *MNRAS*, **294**, 151
- Laing, R.A., 1990, private communication
- Lilly, S.J. 1989, *ApJ*, **340**, 77
- Lilly, S.J., & Longair, M.S. 1984, *MNRAS*, **211**, 833

- Lilly, S.J., & Prestage, R.M. 1987, MNRAS, **225**, 531
- McCarthy, P.J., Spinrad, H., Djorgovski, S., Strauss, M.A., van Breugel, W.,  
& Liebert, J. 1987, ApJ, **319**, L39
- McCarthy, P.J., van Breugel, W., Kapahi, V.K., & Subrahmanya, C.R. 1991, ApJ,  
**371**, 438
- Pedelty, J.A., Rudnick, L.A., McCarthy, P.J., & Spinrad, H. 1989, AJ, **97**, 647
- Sanders, D.B., Soifer, B.T., Elias, J.H., Madore, B.F., Matthews, I.,  
Scarrot, S.M., Rolph, C.D., & Tadhunter, C.N. 1990, MNRAS, **243**, 5P
- Spinrad, H., Djorgovski, S., Marr, J., & Aguilar, L. 1985, PASP, **97**, 932
- Stockton, A. 1982, ApJ, **257**, 33
- Stockton, A. 1990, in Dynamics and Interactions of Galaxies, ed R. Wielen  
(Heidelberg: Springer-Verlag), 440
- Toomre, A., & Toomre, J. 1972, ApJ, **178**, 623

Table 3.1: Spectral Energy Distribution

3CR	z	$b_{\text{II}}$	$E_{\text{(B-V)}}$	2500 Å	AB Magnitudes		1 $\mu\text{m}$
					SC	LC	
65	1.176	-20	0.04	23.38 (V)	22.15	21.73	19.43 (H)
217	0.898	43	0.00	21.93 (B)	21.68	21.14	20.14 (K)
226	0.823	43	0.00	22.99 (B)	21.47	20.94	18.83 (K)
252	1.103	67	0.00	21.93 (V)	21.34	21.17	20.15 (H)
265	0.811	75	0.00	20.77 (B)	19.98		18.43 (K)
266	1.275	64	0.00	21.82 (V)	21.42	20.81	20.09 (H)
267	1.140	70	0.00	22.86 (V)	21.98	20.92	20.34 (H)
280	0.996	70	0.00	22.75 (B)	21.44	20.79	19.10 (K)
289	0.967	65	0.00	23.44 (B)	21.92	20.88	19.02 (K)
324	1.206	49	0.03	22.47 (V)	21.56	21.60	19.75 (K)
352	0.806	36	0.03	22.92 (B)	21.07	21.49	19.10 (K)
356	1.079	34	0.03	22.70 (B)	21.43	20.39	19.53 (K)
368	1.132	15	0.17	20.57 (B)	20.41	19.82	19.18 (K)

Table 3.2: Alignment Parameters

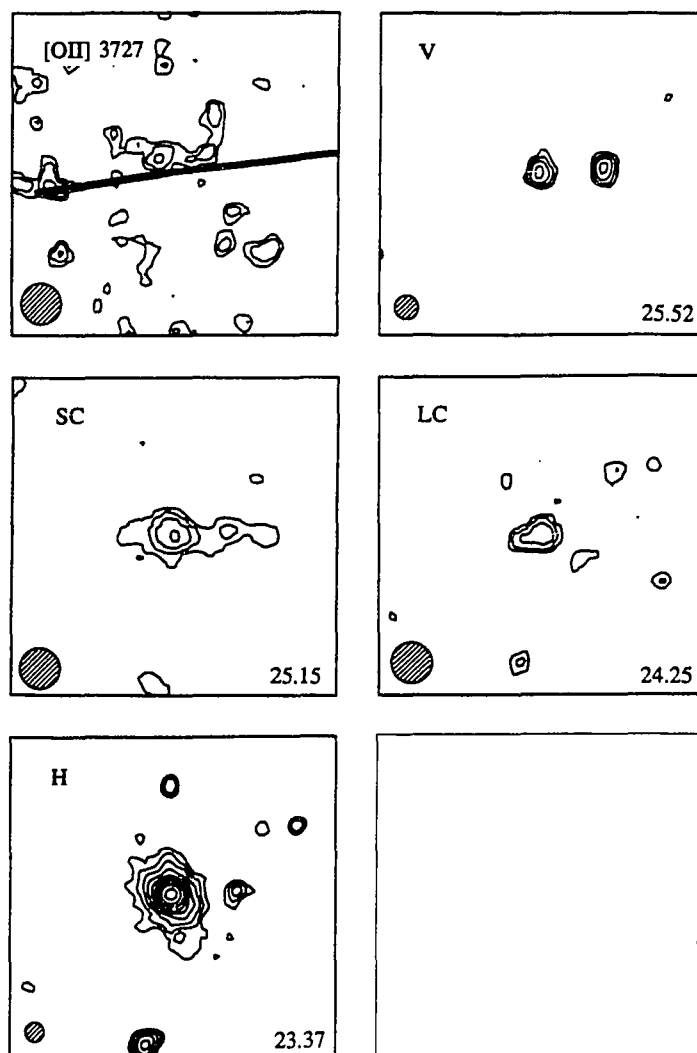
3CR	psf(")	2500 Å		[OII] λ3727		1 μm		Radio	
		ε	ΔPA	ε	ΔPA	ε	ΔPA	PA size(")	
65	1.9	0.12	-19.5	0.25	-18.2	0.06	-64.4	95	16
217	1.6	0.15	-25.6	0.18	-24.3	0.13	-26.5	98	12
226	1.5	0.12	-2.5	0.02	39.3	0.14	67.8	146	35
252	1.3	0.09	20.8	0.05	22.2	0.01	4.7	106	60
265	1.1	0.10	19.3	0.15	67.3	0.12	-22.8	107	78
266	1.3	0.12	9.6	0.44	5.9	0.19	70.1	7	4
267	1.2	0.32	-20.5	0.17	-39.4	0.33	-33.5	80	38
280	1.0	0.27	18.1	0.10	8.0	0.13	-29.5	91	12
289	1.7	0.14	44.8	0.17	37.5	0.08	48.4	109	10
324	1.3	0.24	25.2	0.36	19.5	0.11	-2.1	77	10
352	1.7	0.21	-29.2	0.20	-22.8	0.06	-12.2	176	10
356	1.3	0.13	-3.0	0.19	30.7	0.05	58.1	171	71
368	1.3	0.43	3.1	0.41	1.1	0.31	-9.3	18	8

Table 3.3: Moment Analysis

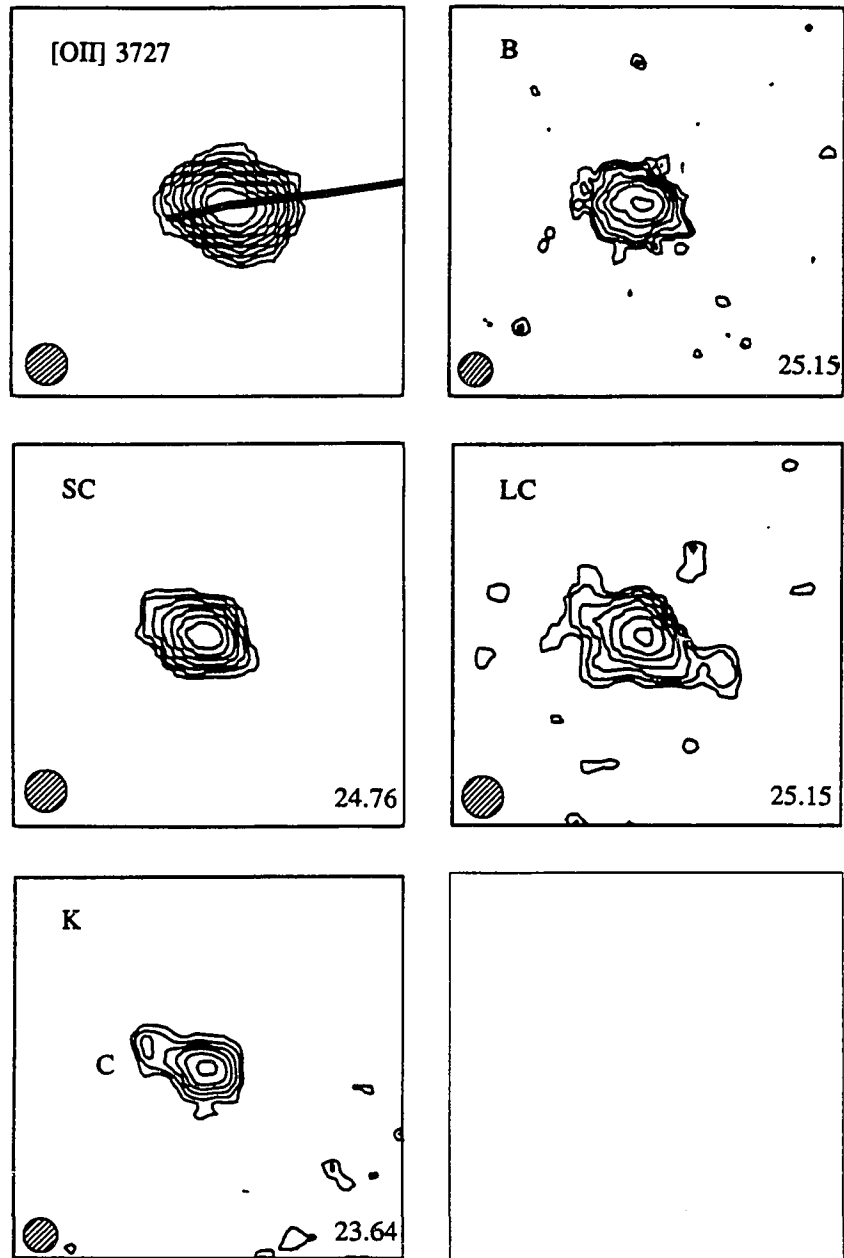
3CR	2500 Å		SC		[OII] λ3727		LC		1 μm	
	S <sub>A</sub>	f <sub>A</sub>	S	f <sub>A</sub>	S	f <sub>A</sub>	S	f <sub>A</sub>	S	f <sub>A</sub>
65	3.89	1.00	3.77	0.97	0.55	0.14	2.01	0.52	-0.26	-0.07
265	4.02	1.00	2.22	0.55	-1.12	-0.15			0.39	0.10
280	10.48	1.00	5.89	0.56	5.02	0.48	2.88	0.27	0.04	0.00
324	10.69	1.00	9.95	0.93	11.77	1.10	8.57	0.80	2.44	0.22
352	7.04	1.00	5.29	0.75	6.99	0.99	1.93	0.27	1.27	0.18

Table 3.4: Red Companions

3CR	d(")	PA(°)	ΔPA	ΔK
217	2.4	69	29	1.3
265	4.6	341	54	1.8
266	1.9	75	68	0.9
280	2.2	13	78	1.9
368	4.3	359	19	1.4



**Figure 3.1—(a-m)** Montages of the unsmoothed multicolor images of each of the 13 3C radio galaxies observed in this program. The images are 15" square (except 3C 265, which is 30" square), and are accurately coregistered. Orientation is within  $1^{\circ}$ - $2^{\circ}$  of NSEW, with north at the top and east at the left. Contours are plotted in logarithmic surface brightness (at root 2 intervals in surface brightness). Images are identified by standard gilter passbands except for LC and SC, which stand for the intermediate-band filters located above and below the  $4000 \text{ \AA}$  spectral feature. The small disk represents the FWHM of the seeing point-spread function. The number indicates the level of the lowest contour in  $\text{AB mag arcsec}^{-2}$ . The radio jet axes are sketched on the  $[\text{O II}] \lambda 3727$  images, and red companions, discussed in the text, are marked by C. (a) 3C 65 ( $z = 1.176$ ).



**Figure 3.1(b)**—Montage of the unsmoothed multicolor images of 3C 217 ( $z = 0.898$ ).

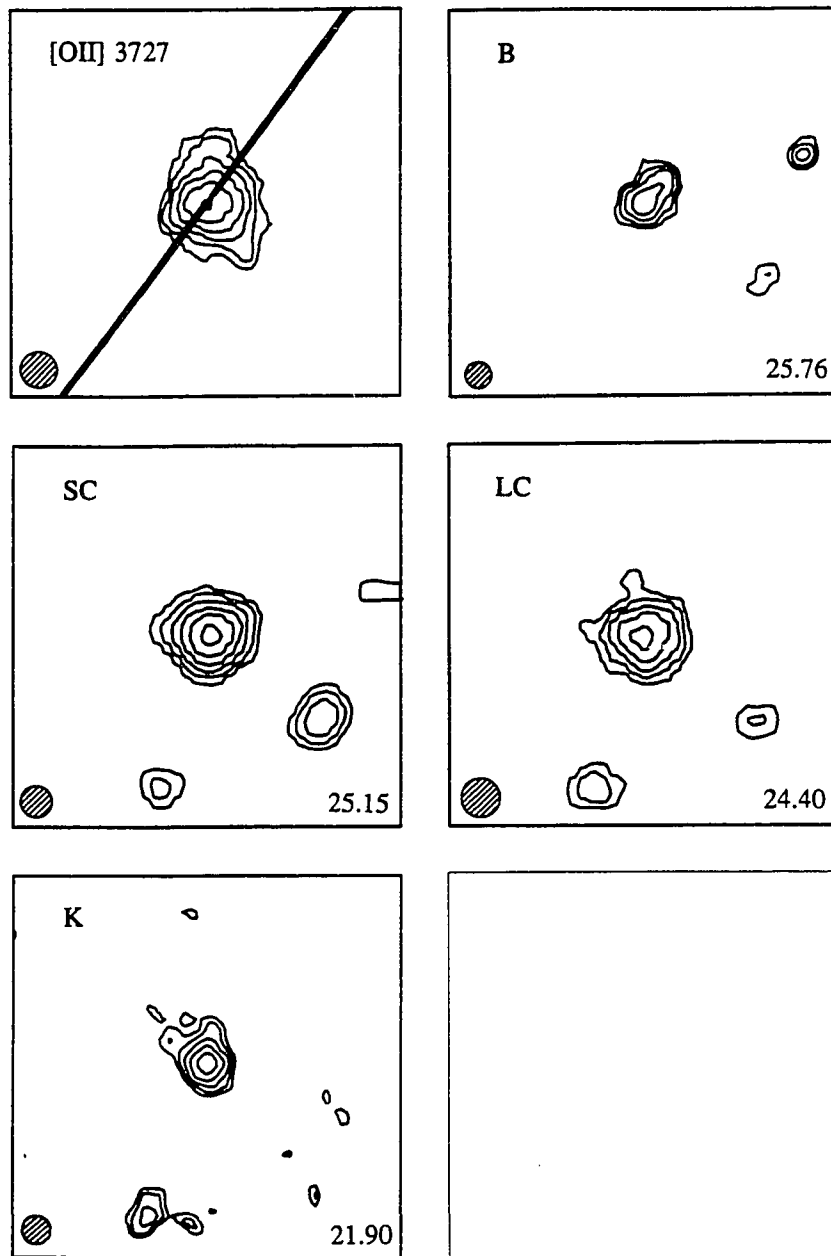


**Figure 3.1(c)**—Montage of the unsmoothed multicolor images of 3C 226 ( $z = 0.823$ ).

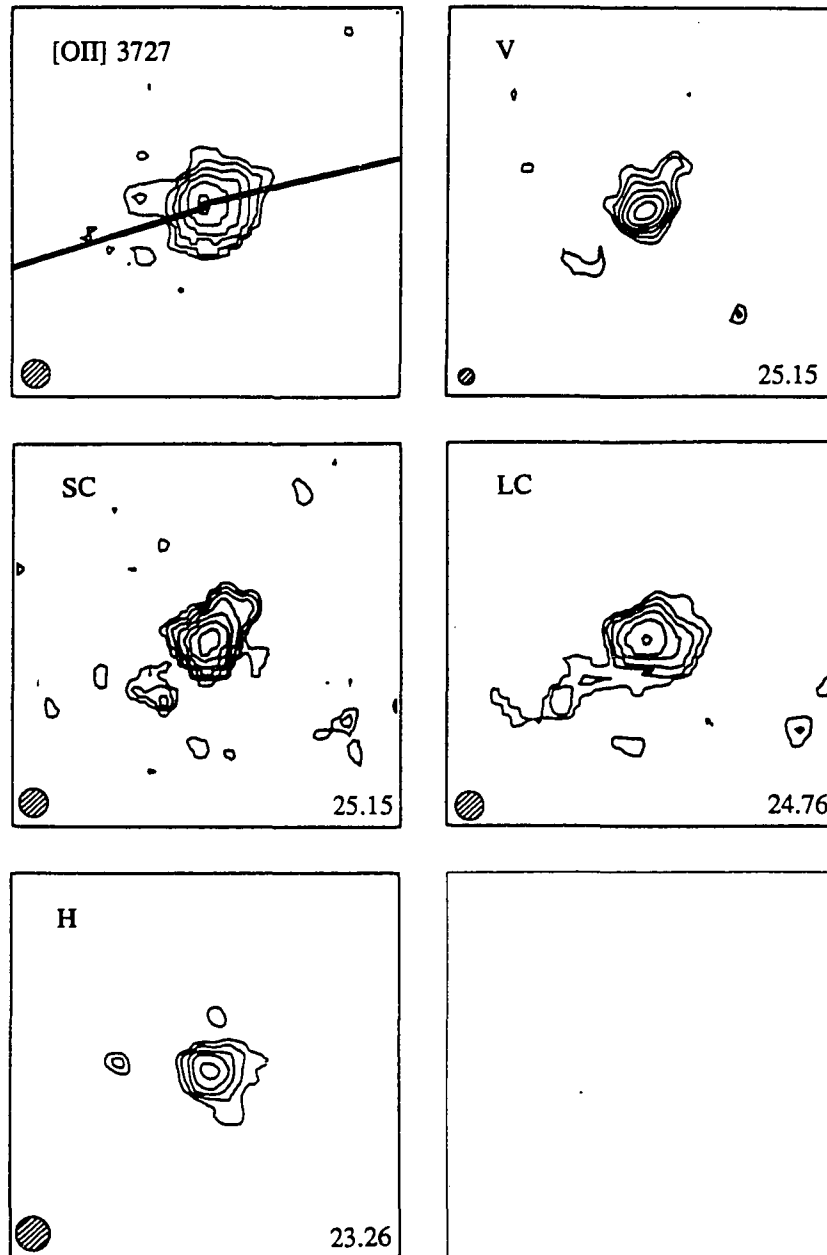


**Figure 3.1(d)**—Montage of the unsmoothed multicolor images of 3C 252 ( $z = 1.103$ ).

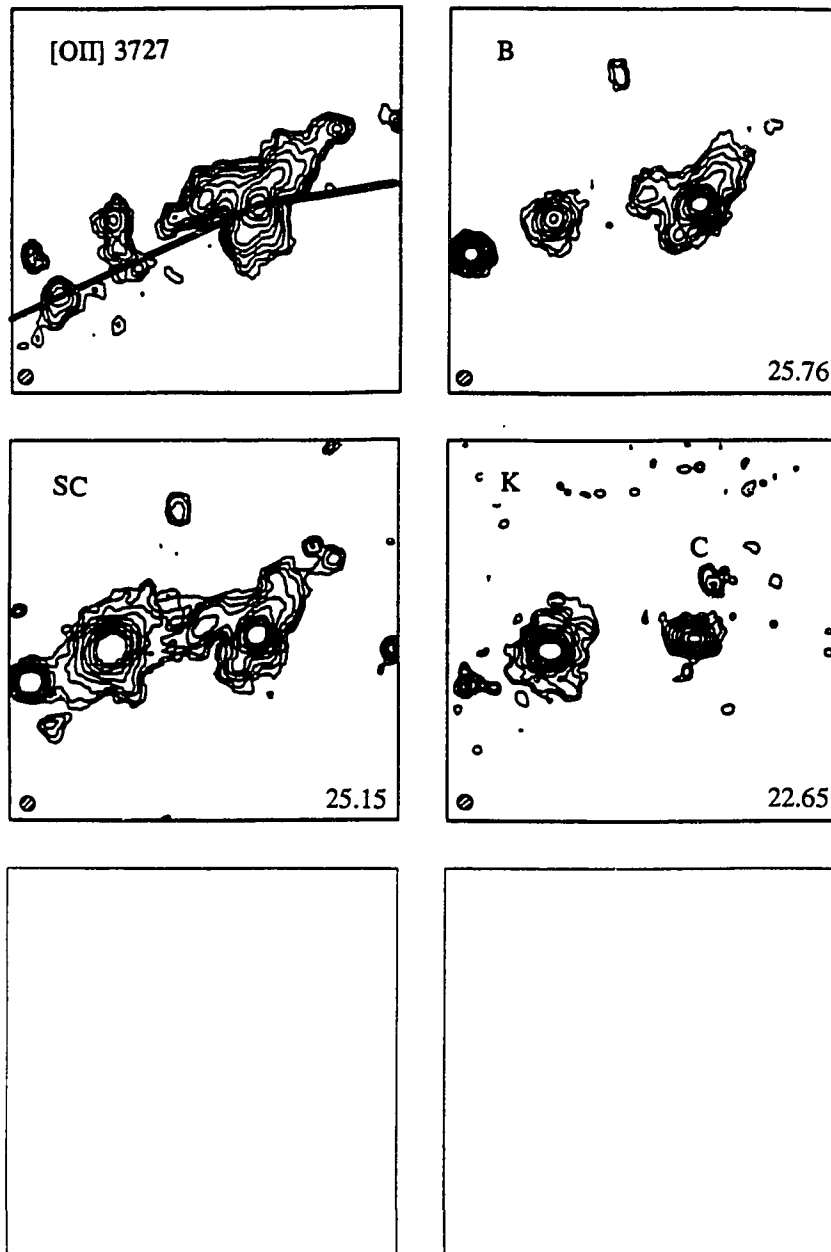


**Figure 3.1(e)**—Montage of the unsmoothed multicolor images of 3C 265 ( $z = 0.811$ ).

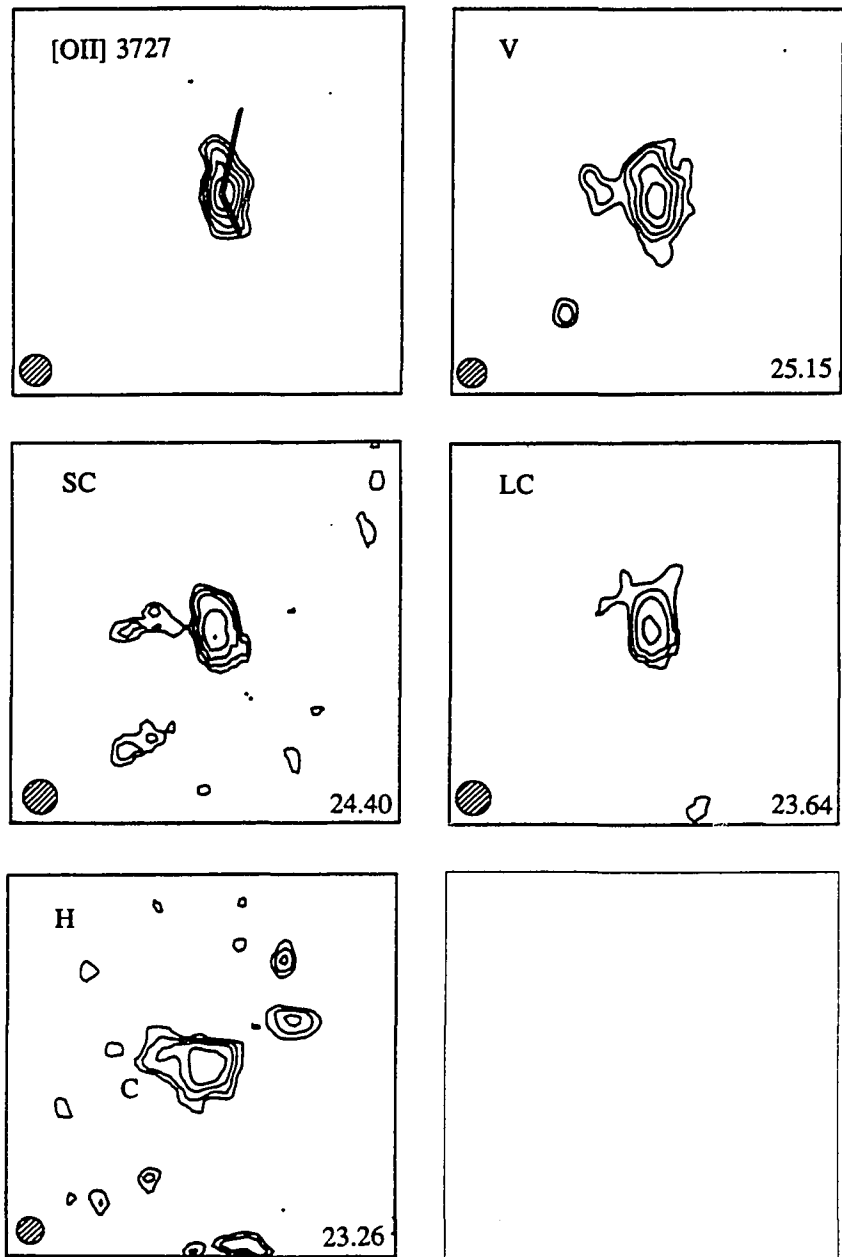


**Figure 3.1(f)**—Montage of the unsmoothed multicolor images of 3C 266 ( $z = 1.275$ ).

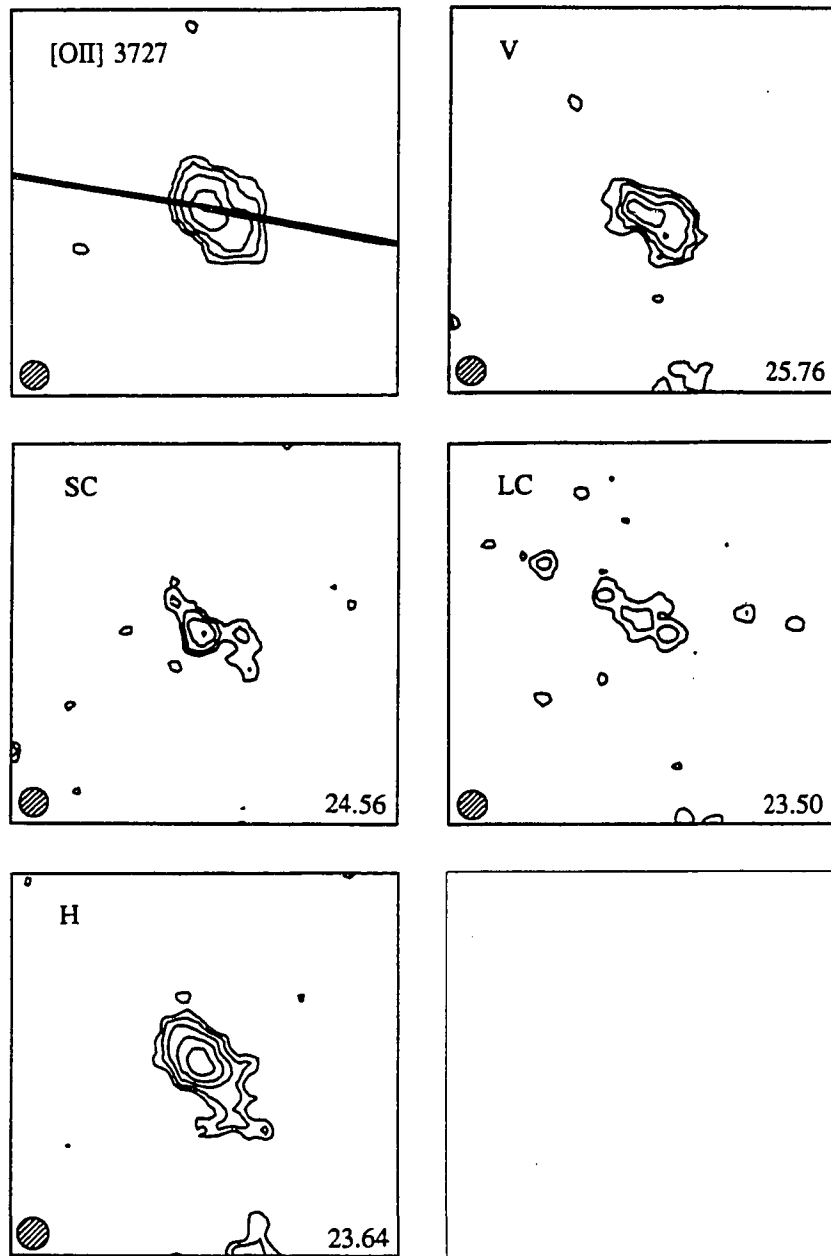


Figure 3.1(g)—Montage of the unsmoothed multicolor images of 3C 267 ( $z = 1.140$ ).

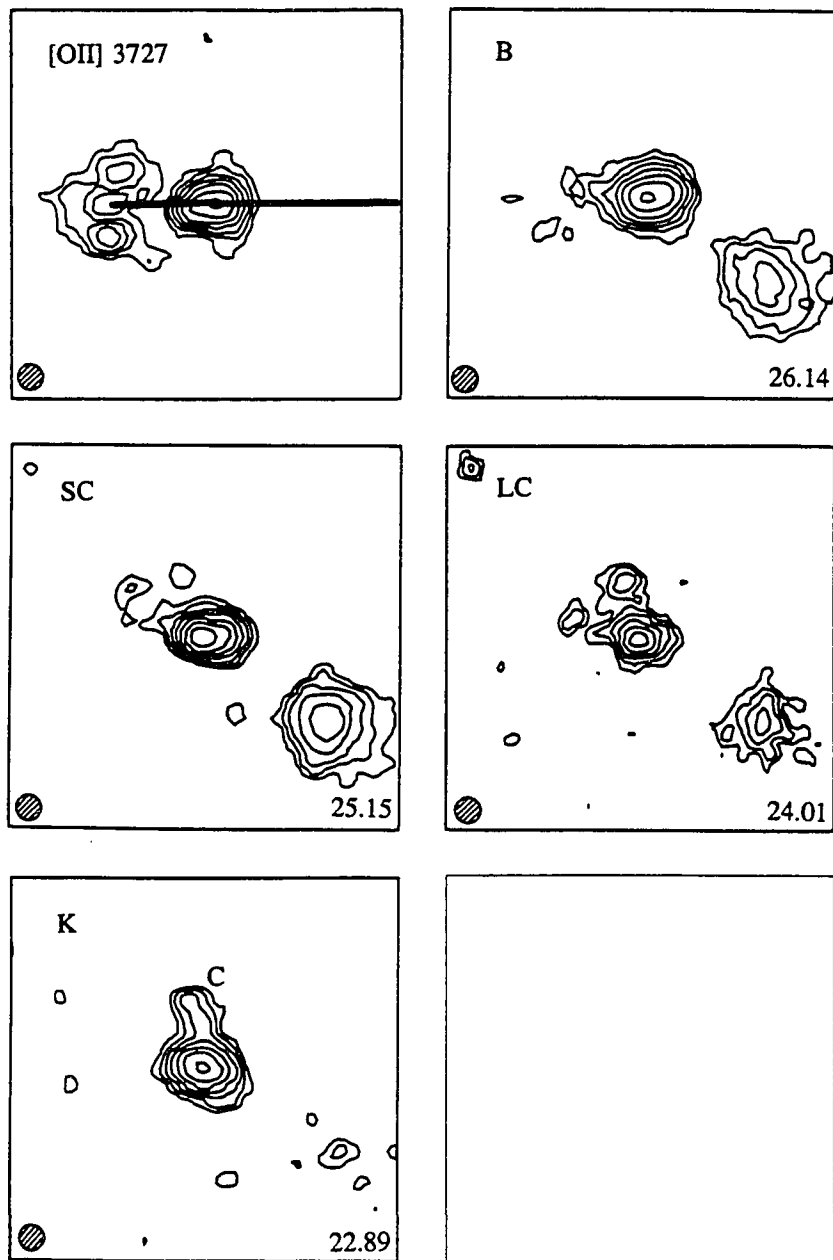
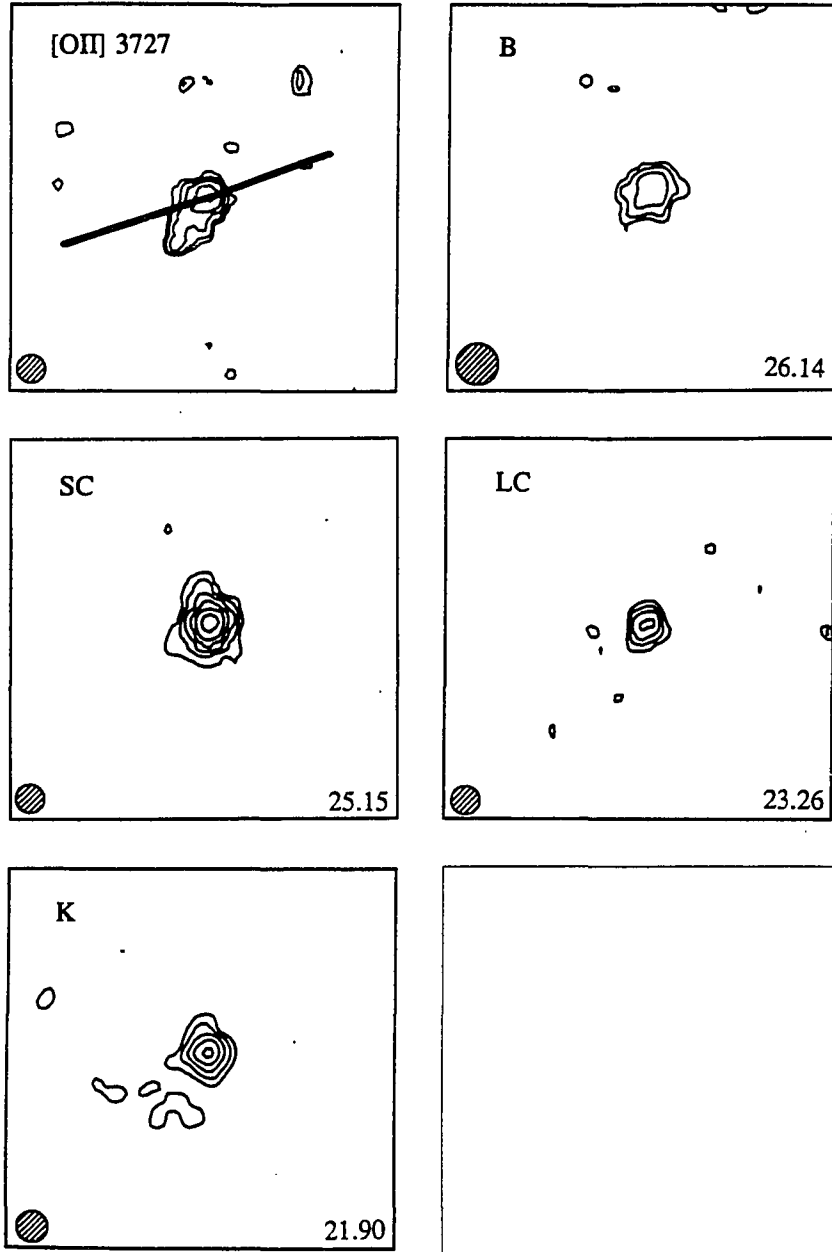
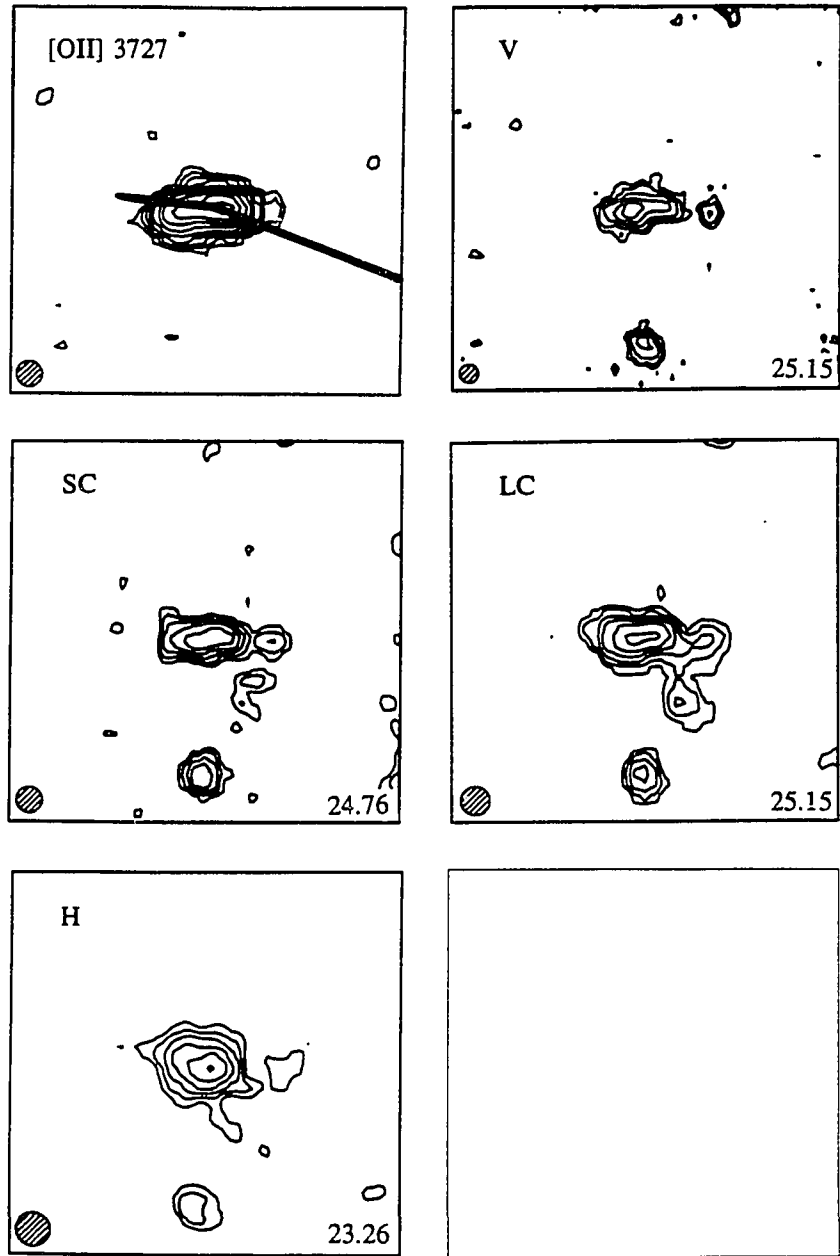


Figure 3.1(h)—Montage of the unsmoothed multicolor images of 3C 280 ( $z = 0.996$ ).



**Figure 3.1(i)**—Montage of the unsmoothed multicolor images of 3C 289 ( $z = 0.967$ ).



**Figure 3.1(j)**—Montage of the unsmoothed multicolor images of 3C 324 ( $z = 1.206$ ).

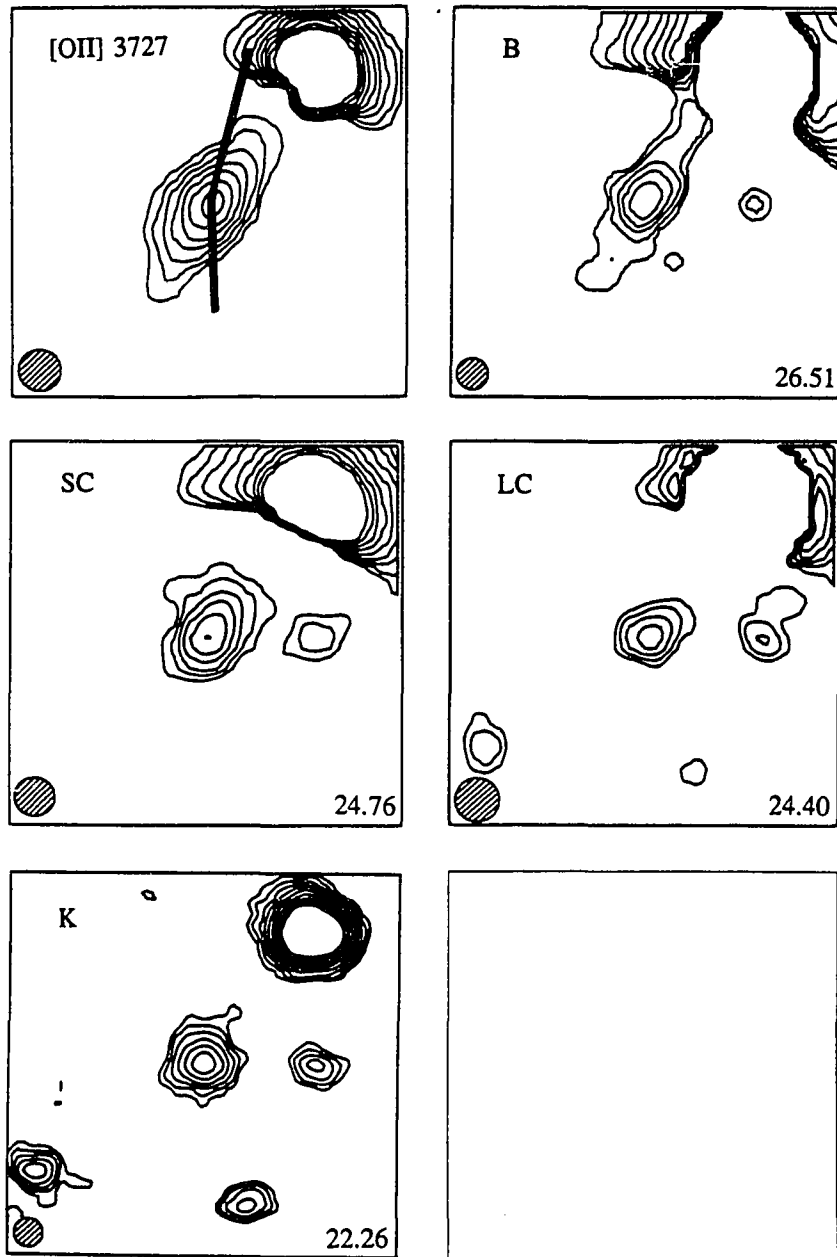


**Figure 3.1(k)**—Montage of the unsmoothed multicolor images of 3C 352 ( $z = 0.806$ ).

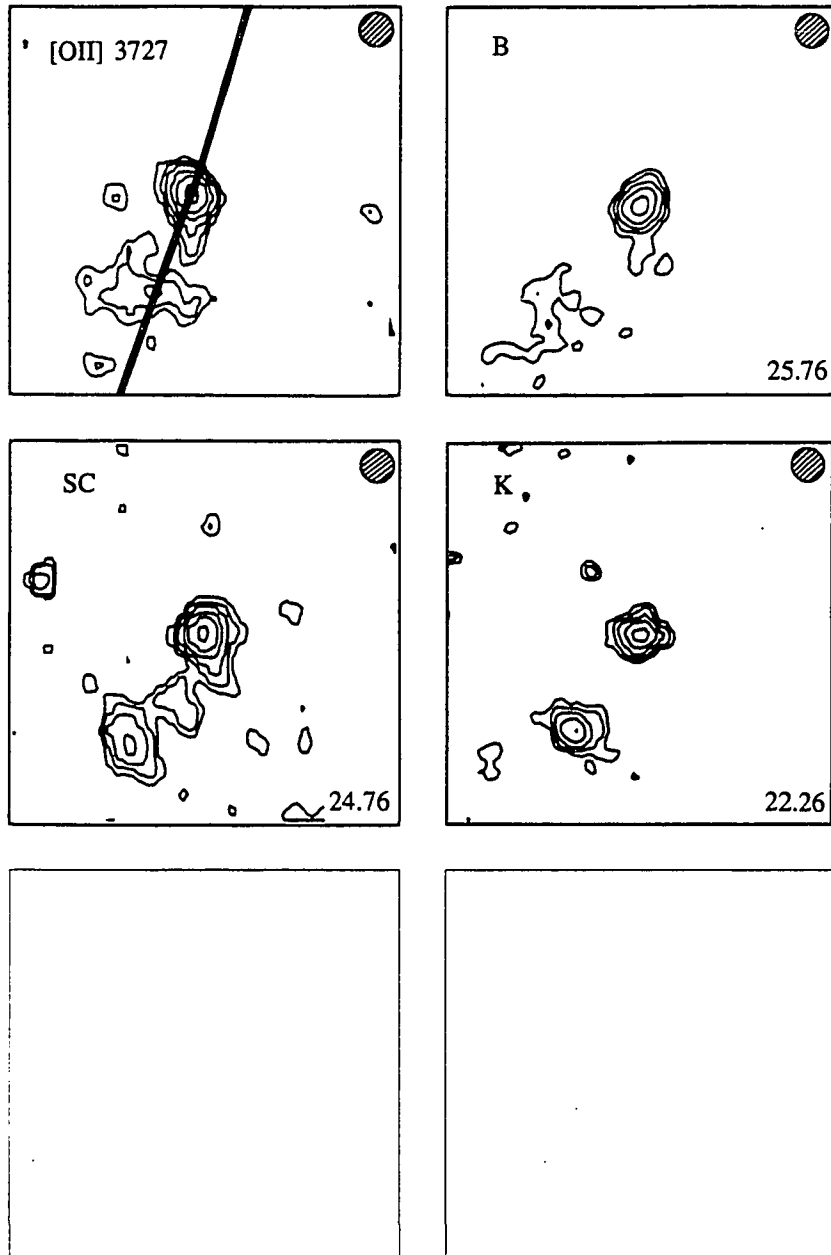


**Figure 3.1(l)**—Montage of the unsmoothed multicolor images of 3C 356 ( $z = 1.079$ ).

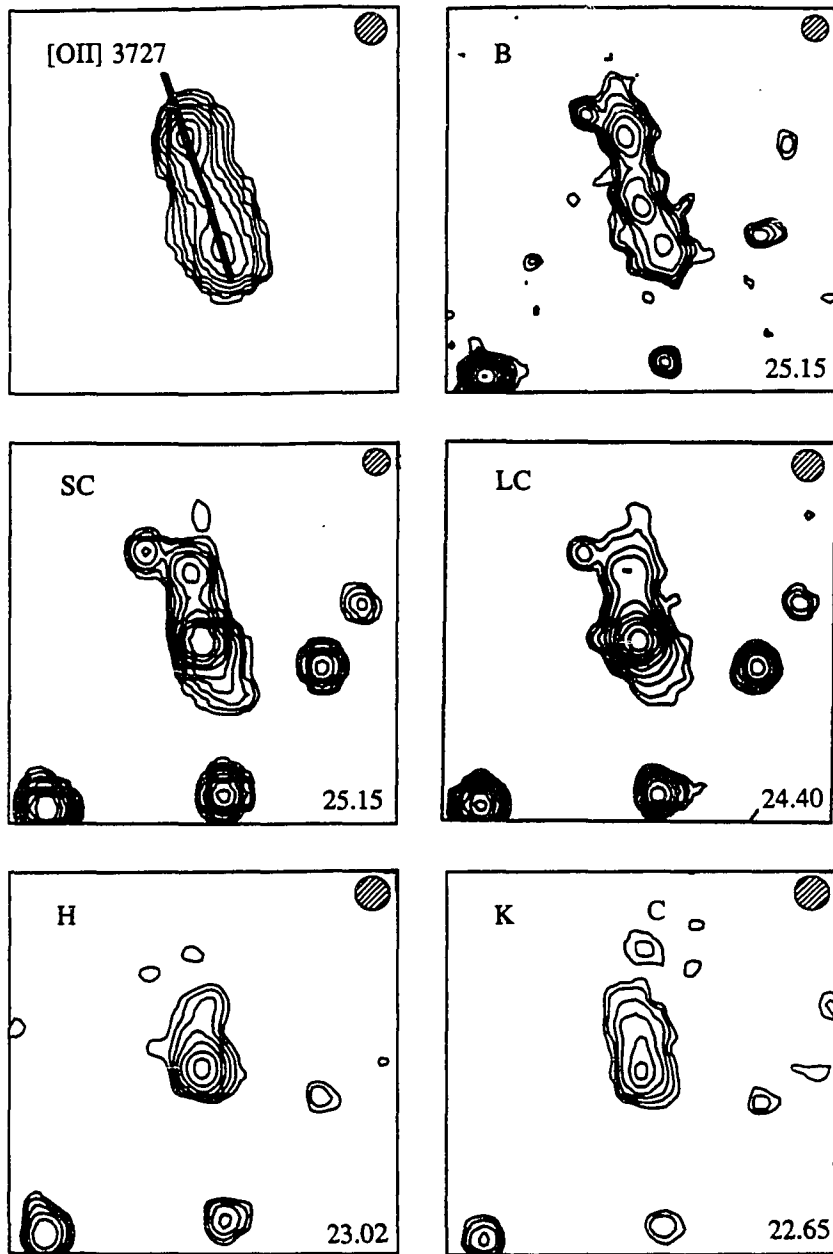


Figure 3.1(m)—Montage of the unsmoothed multicolor images of 3C 368 ( $z = 1.132$ ).

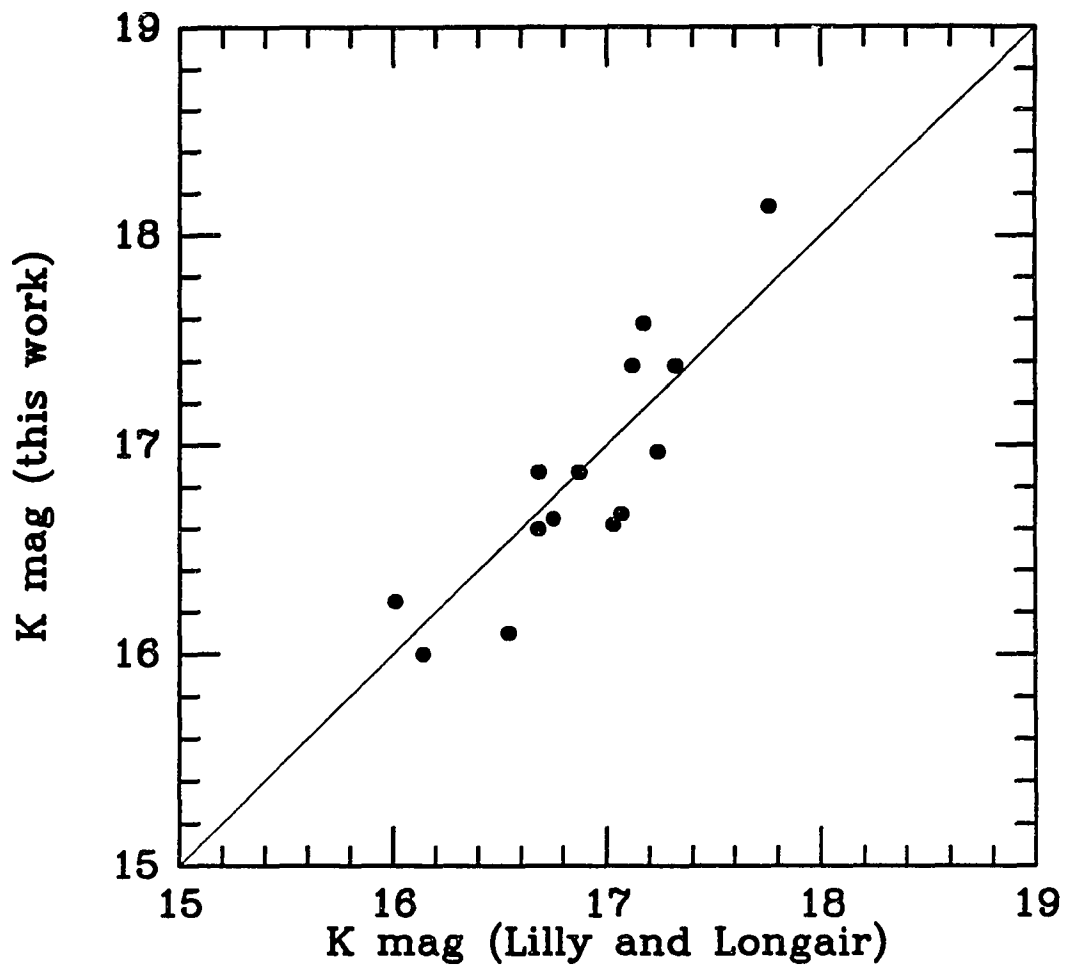


Figure 3.2—Comparison of single-element aperture photometry from Lilly & Longair (1984) and aperture photometry (through the same aperture) constructed from the present two-dimensional array data. Where the observations were carried out in the  $H$  band, they have been converted to  $K$  using  $(H-K) = 1.0$ .

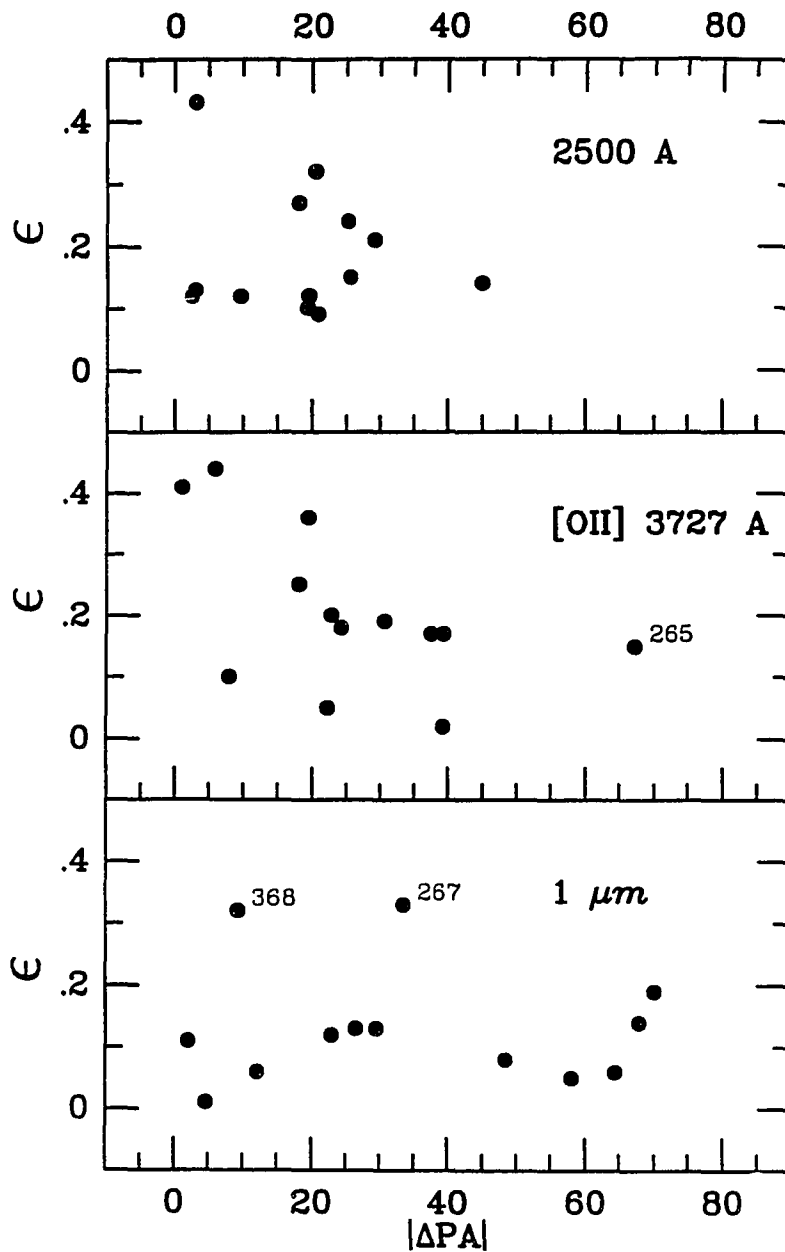
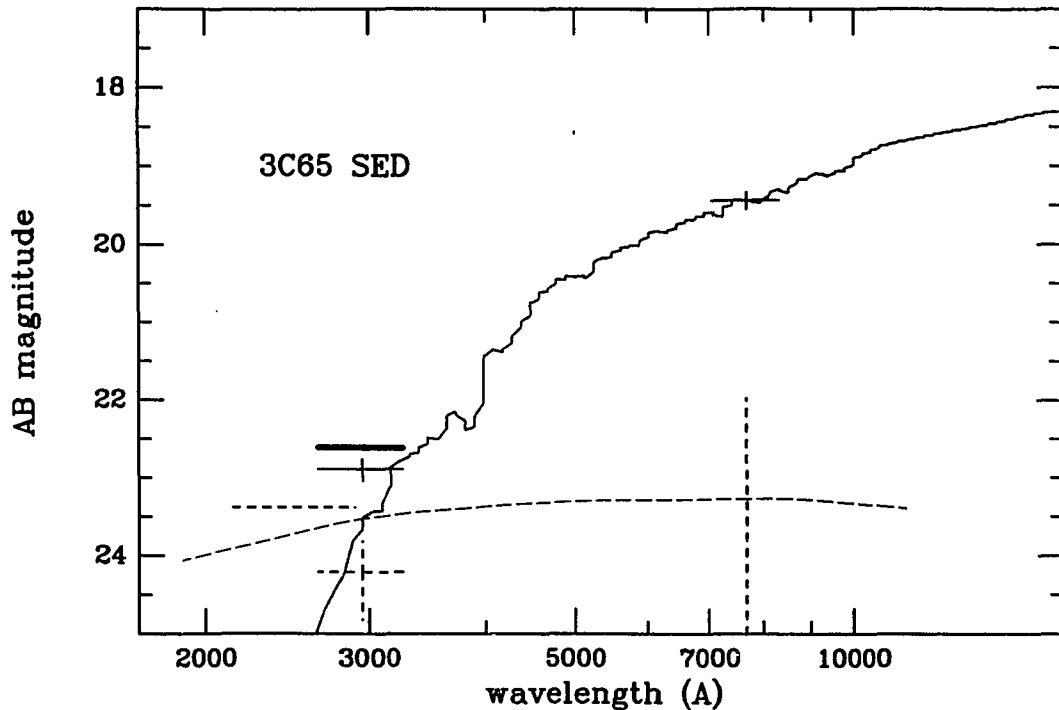


Figure 3.3—Ellipticity parameter  $\epsilon$  plotted against the absolute value of the difference in position angle with respect to that of the radio source axis for the continuum image at approximately rest-frame 2500 Å, for the [O II]  $\lambda 3727$  emission line, and for the infrared continuum at approximately rest-frame 1  $\mu m$ .



**Figure 3.4—(a-e)** Spectral energy distributions for the five galaxies for which a morphological decomposition was attempted (*heavy horizontal lines*). The horizontal width of lines indicates the approximate bandpass of each filter. Other lines represent the "asymmetric" (*dashed line*) and "symmetric" (*continuous line*) components based on the nonunique morphological decomposition described in the text. Vertical error bars are based on a 10% uncertainty in the  $f_A(\lambda)$  parameter. For reference, the spectral energy distribution of a gE galaxy (Coleman et al. 1980) is shown passing through the "symmetric" point at long wavelengths, and a smooth continuum has been drawn by eye through the "asymmetric" component. Note that the 2500 Å continuum is assumed, in this analysis, to define the "asymmetric" component. The figures indicate that while this asymmetric aligned component contaminates at very short wavelengths, it has a roughly flat spectral energy distribution in  $f_\nu$  and contributes only a small fraction of the infrared light. Continuum bands which were contaminated by [O II]  $\lambda 3727$  emission or were of very low quality have been omitted. (a) 3C 65 ( $z = 1.176$ ).

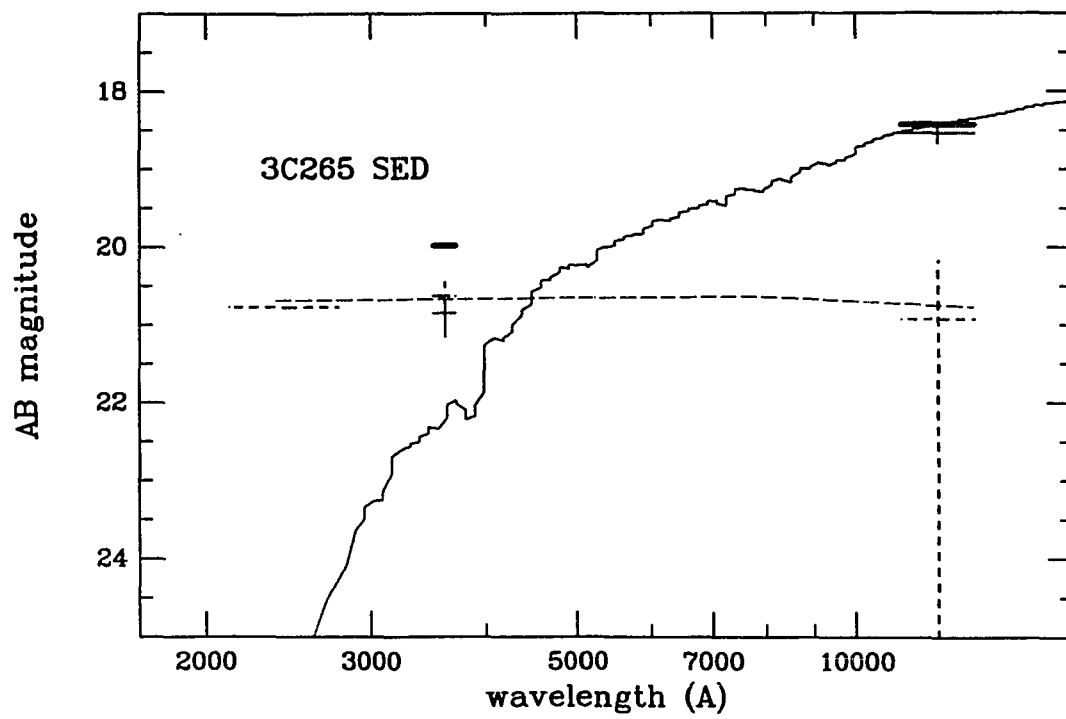


Figure 3.4(b)—Spectral energy distribution for 3C 265 ( $z = 0.811$ ).

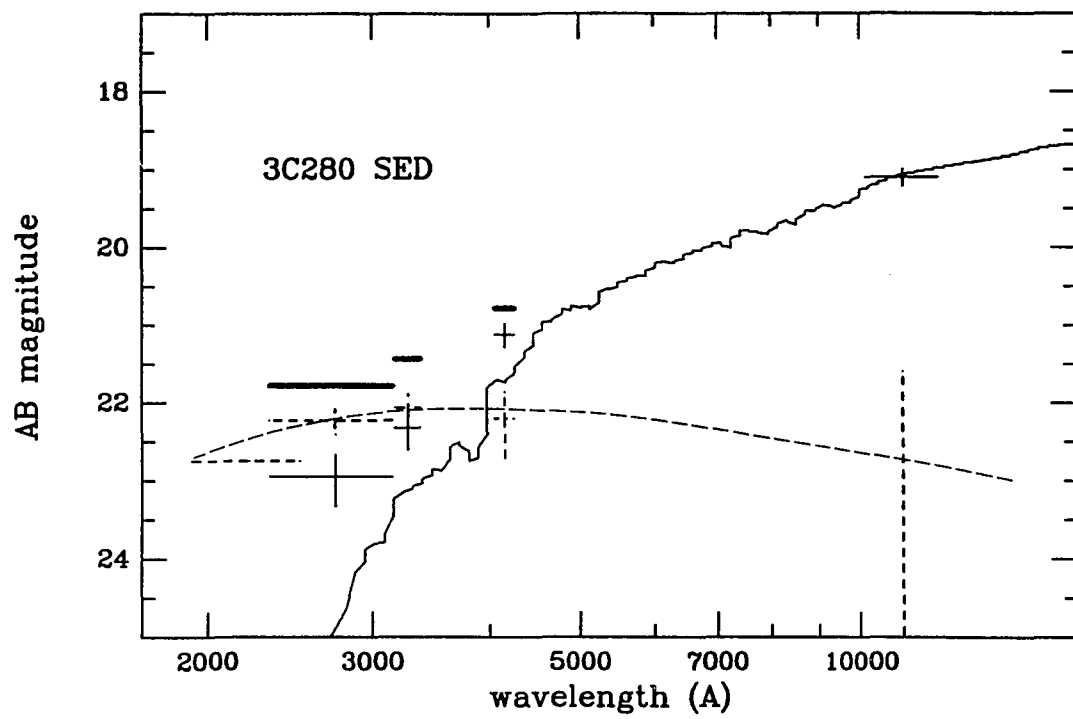


Figure 3.4(c)—Spectral energy distribution for 3C 280 ( $z = 0.996$ ).

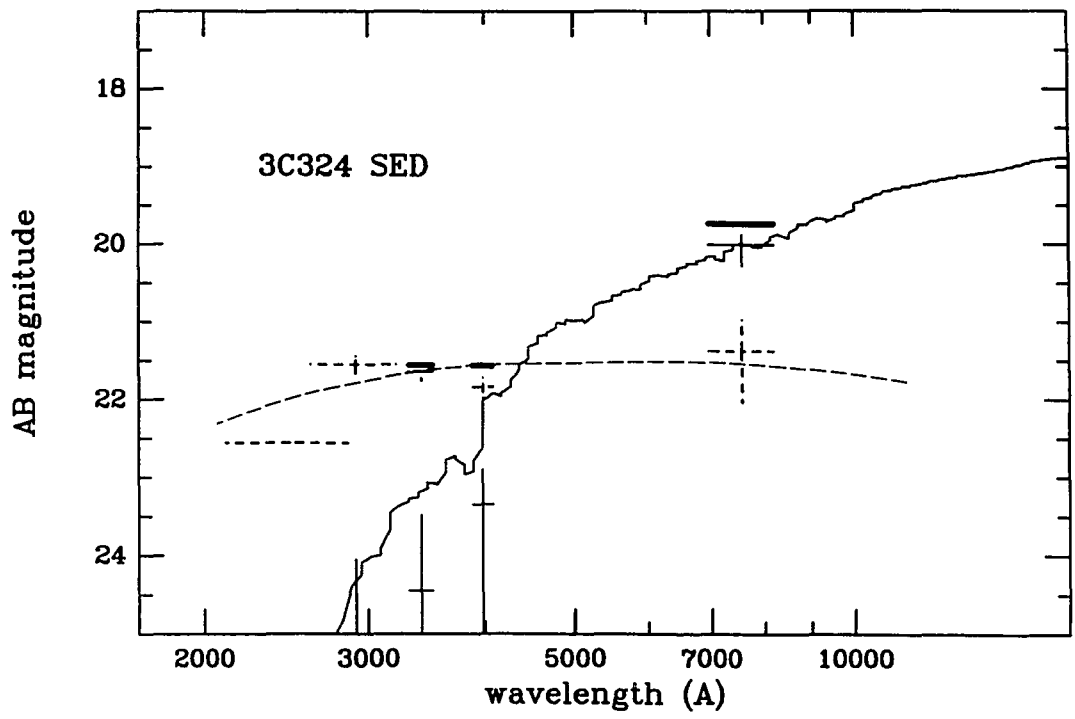


Figure 3.4(d)—Spectral energy distribution for 3C 324 ( $z = 1.206$ ).

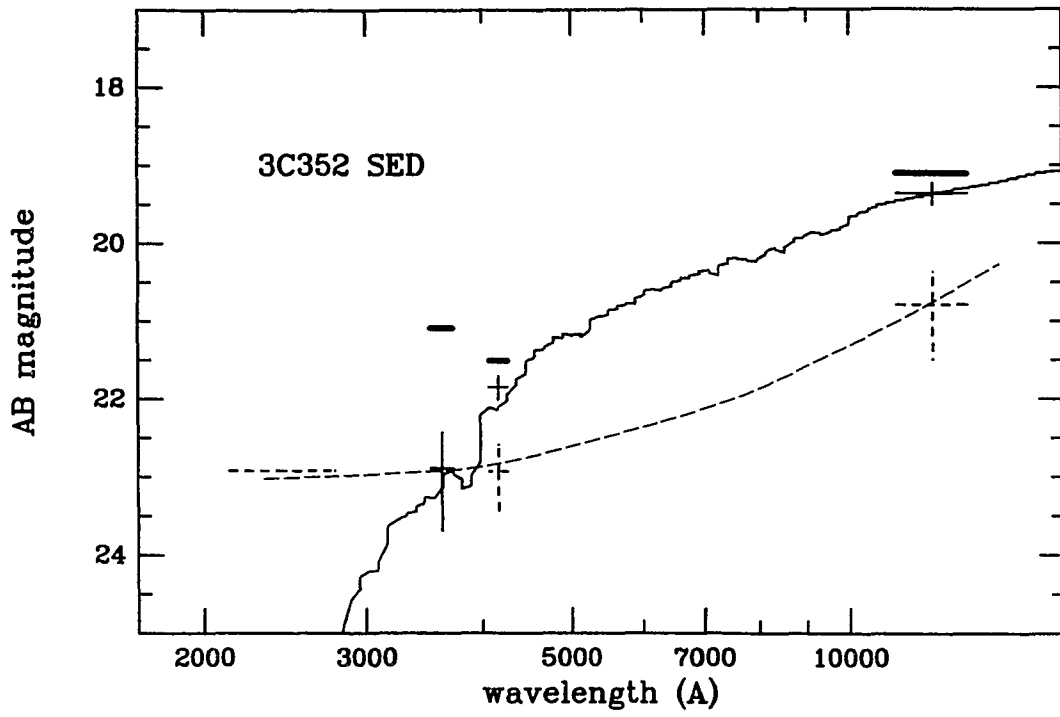
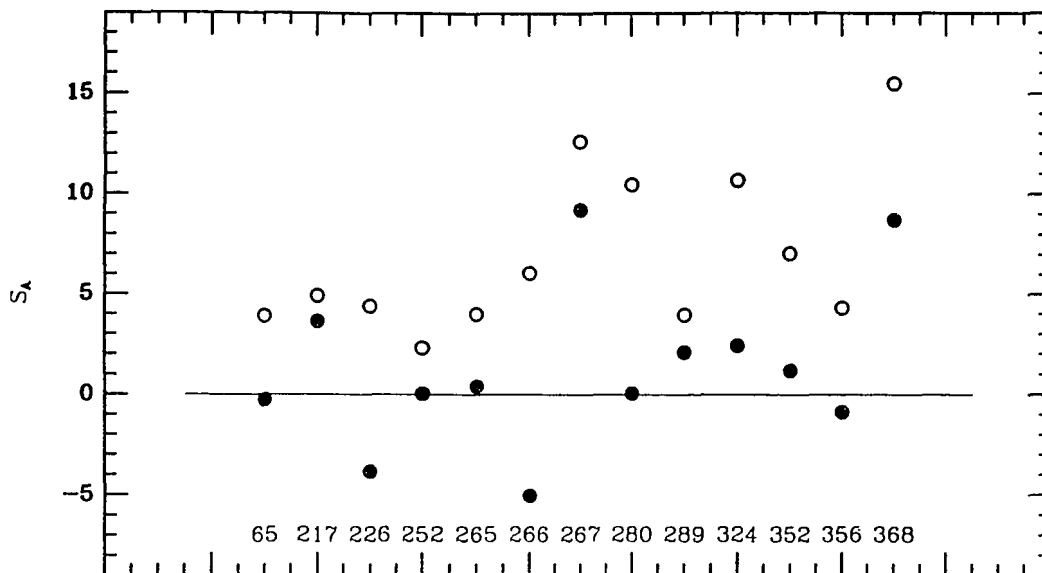
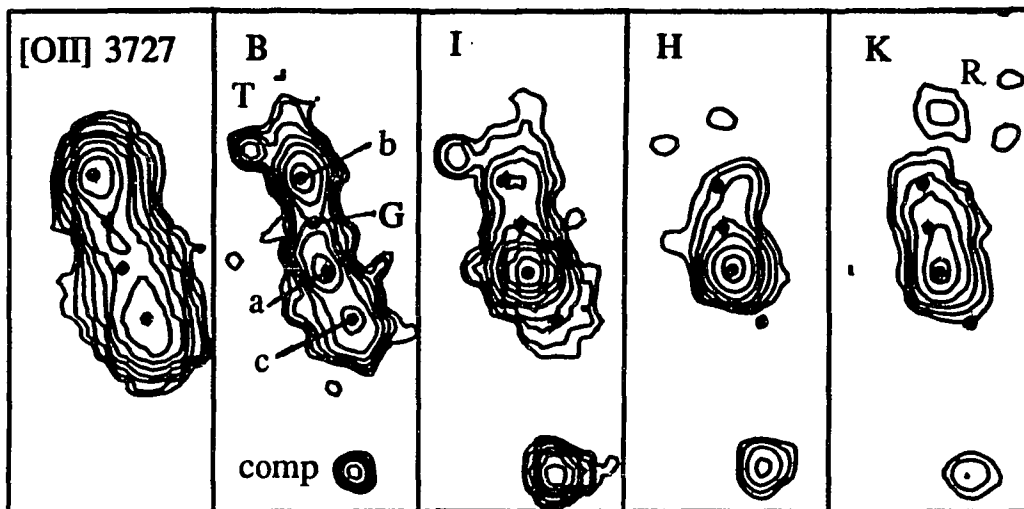


Figure 3.4(e)—Spectral energy distribution for 3C 352 ( $z = 0.806$ ).



**Figure 3.5**—Moment parameter (along the preferred axis defined by the 2500 Å image),  $S(\lambda)$ , measured at 2500 Å (*open symbols*) and 1 μm (*filled symbols*) for all the objects in the sample. In every case  $S$  is substantially smaller in the infrared, indicating that a red symmetric component dominates at long wavelengths.



**Figure 3.6**—Detailed montage of 3C 368 identifying the various components discussed in the text. The brightest component ("a") is very likely to be a superposed Galactic M star.

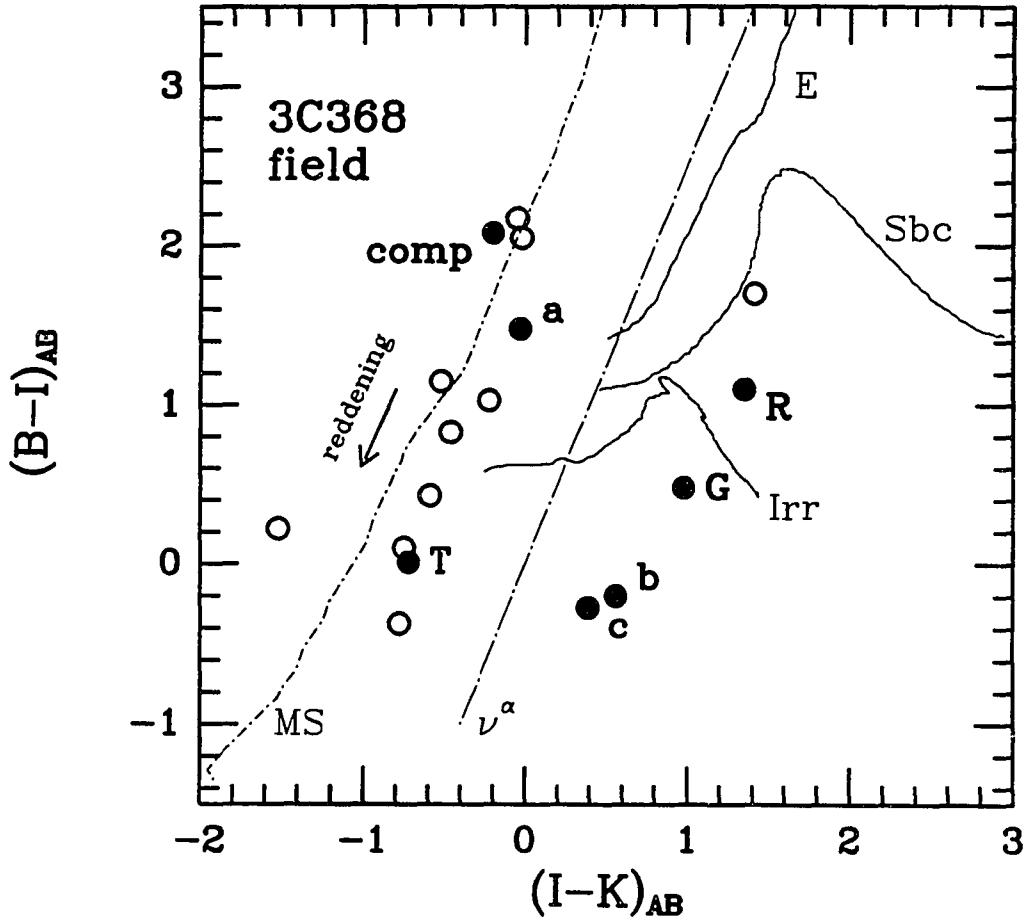
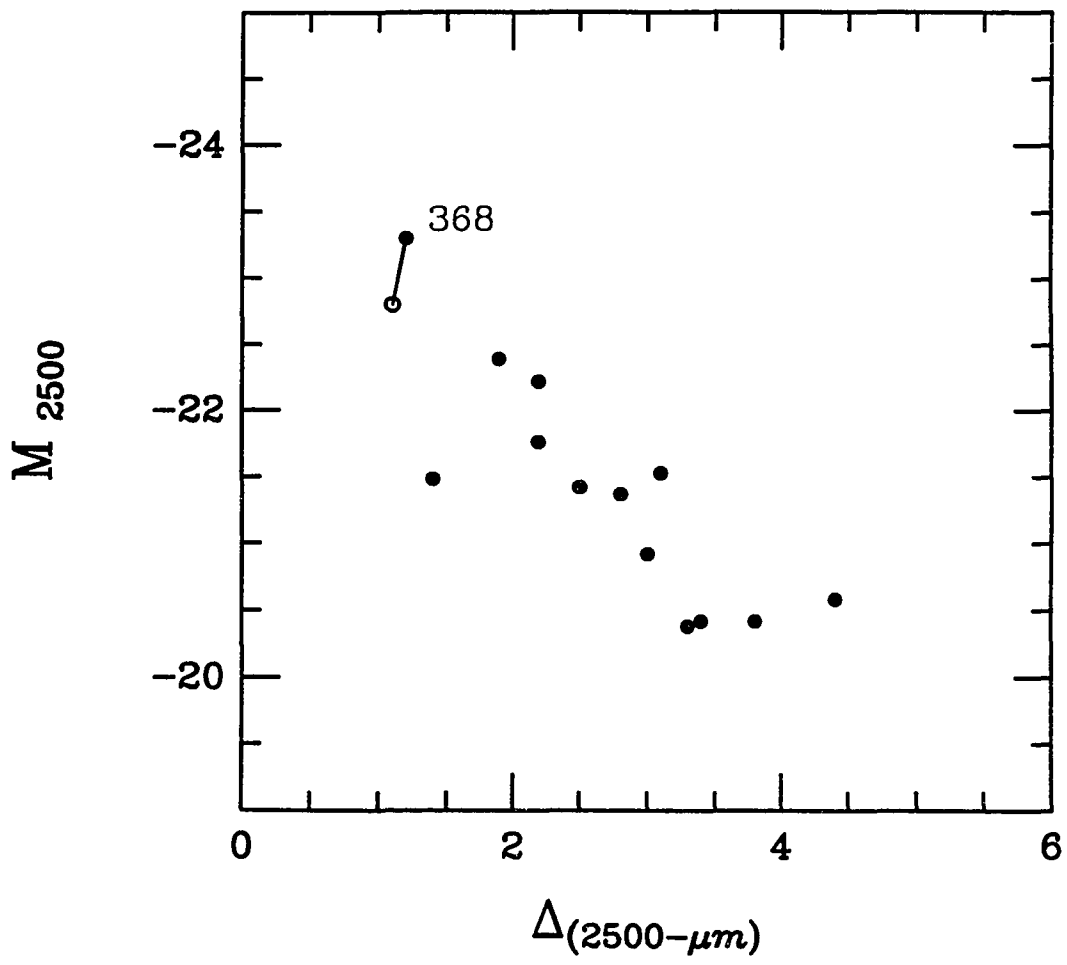


Figure 3.7— $(B-I)_{AB}/(I-K)_{AB}$  two-color diagram for objects in the 3C 368 field. The lines represent the stellar main sequence, power-law spectral energy distributions, and the colors of E, Sbc, and Irr galaxies as a function of  $z$  in the interval  $0 < z < 2$ . All the data points have been dereddened with the reddening vector shown.



**Figure 3.8(a)**—Color-absolute magnitude diagram for the galaxies in the sample, showing 2500 Å to 1 μm color vs. 2500 Å absolute magnitude. 3C 368 has been shown as observed (*solid symbol*) and after attempted removal of the putative M star (*filled symbol*).

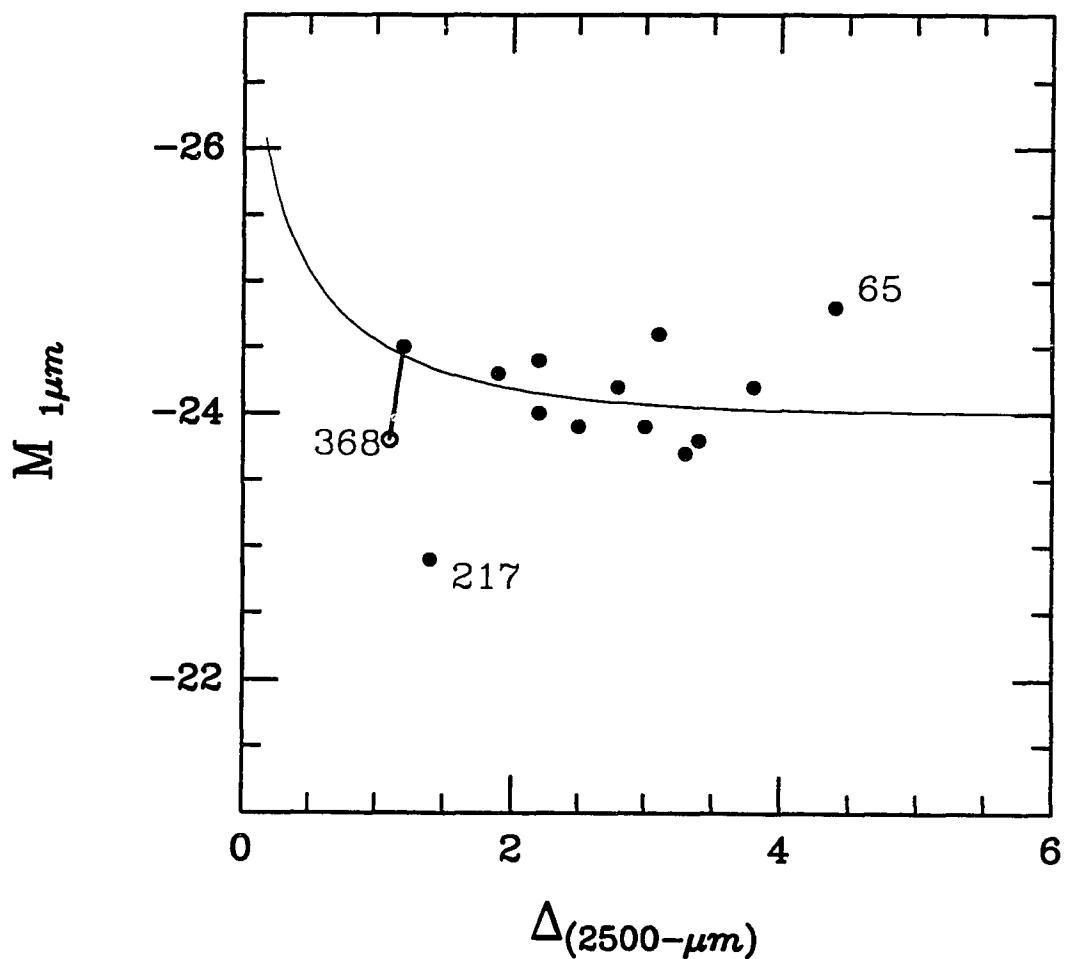


Figure 3.8(b)—Color-absolute magnitude diagram for the galaxies in the sample showing 2500 Å to 1 μm color vs. 1 μm absolute magnitude. The curve represents the expected effect of adding a flat-spectrum component to a gE galaxy. 3C 368 has been shown as observed (*solid symbol*) and after attempted removal of the putative M star (*filled symbol*).

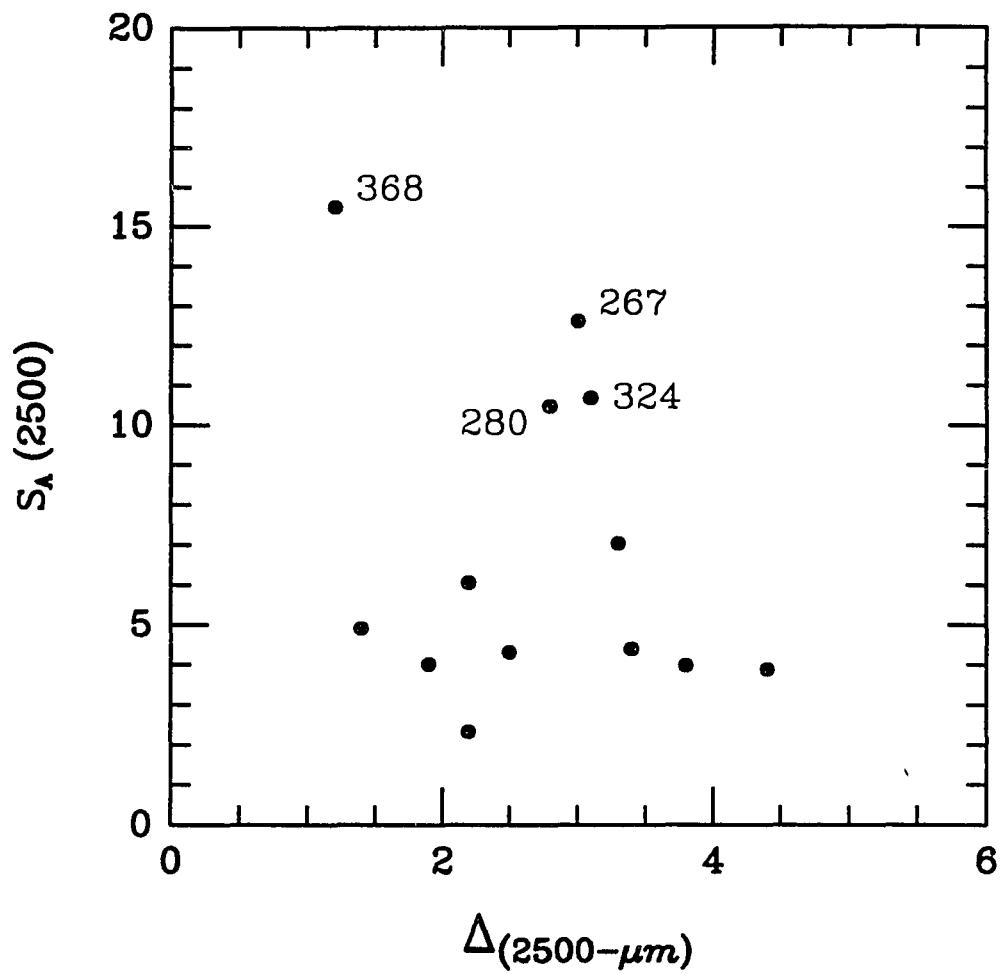


Figure 3.9(a)—Relationship between the overall 2500 Å to 1 μm color and the degree of alignment, parameterized by the moment  $S$  along the axis defined by the 2500 Å image, determined at 2500 Å.

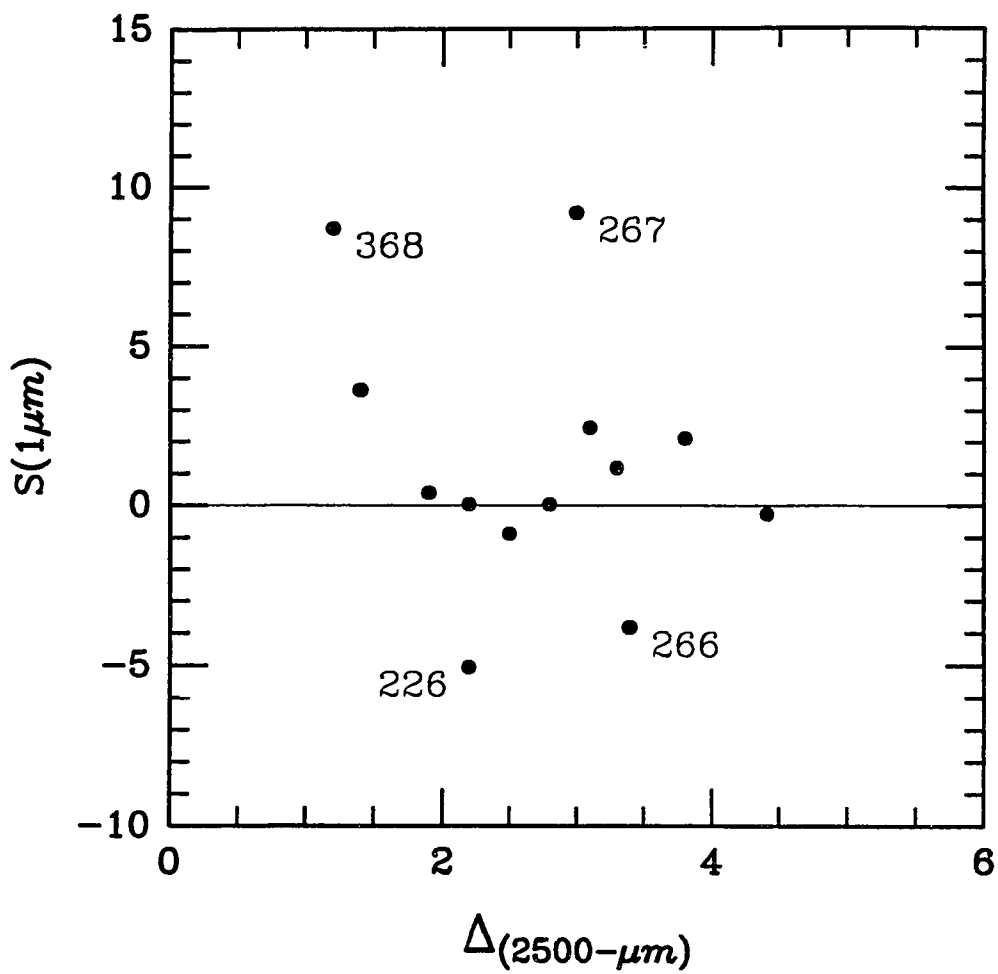
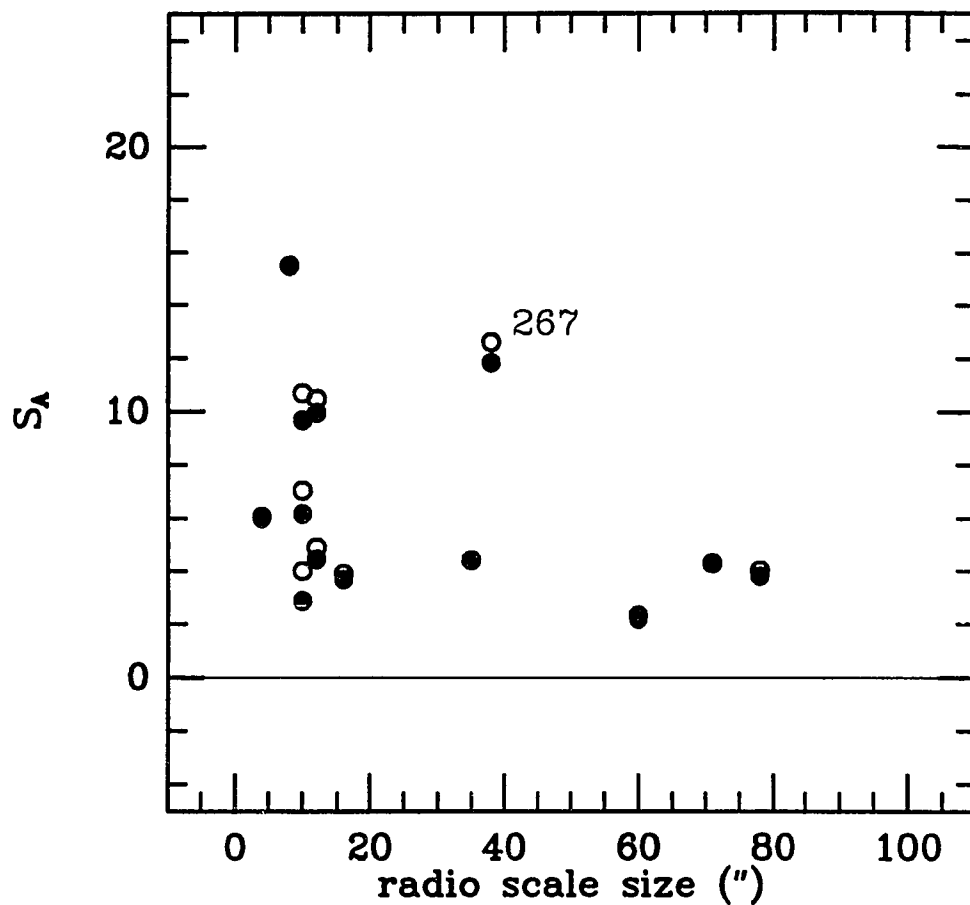
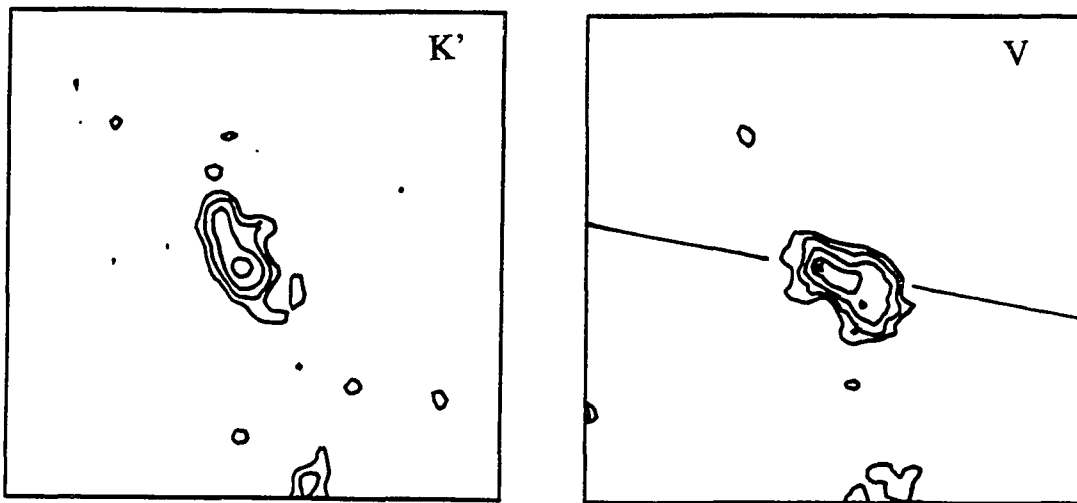


Figure 3.9(b)—Relationship between the overall 2500 Å to 1 μm color and the degree of alignment, parameterized by the moment  $S$  along the axis defined by the 2500 Å image, determined at 1 μm.



**Figure 3.10**—Diagram showing the tendency for the most dramatic alignment effects to occur in objects associated with physically small radio sources. Open symbols represent  $S_A$ ; filled symbols are  $S_A \times \cos 2\theta$ , where  $\theta$  is the misalignment angle between the radio source axis and the  $2500 \text{ \AA}$  axis.



**Figure 3.11**—A montage of the unsmoothed V and K' images of 3C 267. The images are 15" square and are very accurately coregistered. Orientation is within 1-2° of NSEW, with north at the top and east at the left. Contours are plotted in logarithmic surface brightness (at root 2 intervals in surface brightness). Images are identified by standard filter passbands. The radio jet axis is sketched on the V-band image. On the V-band image, a small 'X' has been marked at the position of the K'-band surface brightness peak to aid the eye. The 3C 267 system can be readily interpreted as an evolved galaxy located at the K' surface brightness peak, with a red northward extension (possibly due to an unresolved red companion), and aligned blue emission extending along the southwestern radio axis.

## CHAPTER 4: SURFACE PHOTOMETRY OF QUIESCENT RADIO GALAXIES

### 4.1 Preface

The material presented in this chapter has been prepared for publication in the *Astrophysical Journal Letters* under the title "Infrared Surface Photometry of High-Redshift Radio Galaxies: Stellar Evolution and the Tolman Signal" (Rigler & Lilly, in preparation). The organization of this chapter closely follows that of the paper. First, we briefly discuss the prospect of using quiescent radio galaxies to study ellipticals at high redshift. Second, we review the observational details and the advantages of using the NICMOS-3 array. Then, we describe the morphological characteristics of the two high-redshift galaxies and outline a detailed analysis used to measure their photometric parameters. Next, we compare the photometric parameters of the high-redshift radio galaxies to those of lower redshift radio galaxies, brightest cluster members (BCMs) and ellipticals, and discuss the results in the context of galaxy evolution and cosmology. The results are briefly summarized in the final section.

### 4.2 Abstract

In this chapter we present an analysis of the infrared surface brightness profiles of two high-redshift radio galaxies, 3C 65 ( $z = 1.176$ ) and 3C 437 ( $z = 1.480$ ), which are well fit by a deVaucouleurs  $r^{1/4}$  law. A model surface fitting routine yields characteristic photometric parameters comparable to those of brightest

cluster members (BCMs) and low-redshift radio galaxies for standard cosmologies. The small displacement of these galaxies from low-redshift BCMs and radio galaxies on the  $\mu_e$ - $\log r_e$  plane suggests that little or no stellar evolution is required in a cosmology with  $q_0 = 0.5$  ( $\Lambda = 0$ ), while a modest degree of stellar evolution is implied in a model with  $q_0 = 0$  ( $\Lambda = 0$ ), or models with  $\Lambda > 0$ . A non-expanding cosmology would require the high-redshift systems to lie at the extreme end of the distribution of properties of local gE galaxies. The effects of stellar and/or dynamical evolution would be to make the objects more extreme.

### 4.3 Introduction

Infrared observations of high-redshift radio galaxies, through their sensitivity to older stellar populations, have come to play a vital role in our understanding of the evolutionary status of these objects. The smooth continuity and small dispersion seen in the infrared K-z Hubble diagram for radio galaxies with  $z \leq 2$  and beyond suggests that the infrared emission of essentially all radio galaxies is dominated by massive, mature gE-like stellar populations (Lilly & Longair, 1984; Lilly 1989).

However, radio galaxies with  $z > 1$  display a wide range of optical to infrared colors, elongated morphologies and a statistical tendency of these for alignment with the radio jet axes (Chambers, Miley, & van Breugel 1987; McCarthy et al. 1987). Rigler et al. (1992) undertook a spectro-morphological analysis of a complete sample of 3C radio galaxies at  $z \approx 1$  which showed that the morphologies at each wavelength are consistent with the superposition of two different morphological com-

ponents: (1) a round symmetric component having a gE-like spectral energy distribution (SED) which dominates at infrared wavelengths, and (2) an aligned component having a much bluer SED ( $f_{\nu} \approx \nu^0$  to  $\nu^{-1}$ ) which is generally dominant at UV-optical wavelengths. This result is consistent with the idea that essentially all radio galaxies have mature underlying stellar populations producing the small scatter in the  $K-z$  relation. In this scenario, the reddest objects in any sample are expected to appear in the infrared as gEs, in the sense that they will be most free from the emission causing the alignment effect (see, e.g., Daly 1992, for a review of the alignment effect). These reddest objects therefore offer the most promising targets for studies of elliptical galaxies at high redshift. Infrared surface photometry of gEs at cosmologically significant redshifts also could in principle provide constraints on  $q_0$  and  $\Lambda$ , and test for the presence of  $(1+z)^4$  surface brightness dimming due to the Universal expansion. In this chapter, we present a detailed morphological analysis of two such quiescent radio galaxies, 3C 65 ( $z = 1.176$ ), which is the reddest member of the  $z = 1$  sample of Rigler et al. (1992), and 3C 437 ( $z = 1.480$ ). Where necessary, a value of for the Hubble constant of  $H_0 = 50 \text{ km s}^{-1} \text{ Mpc}^{-1}$  is assumed.

#### 4.4 Observations and Reductions

Deep, high-resolution infrared images were obtained of 3C 65 in the H band and 3C 437 in the K' band during a run on the Canada-France-Hawaii 3.6 m telescope (CFHT) in 1990 September, using the UH NICMOS-3 Near Infrared Camera (Hodapp et al., 1992) in the Cassegrain focus at plate scales of  $0.29'' \text{ pixel}^{-1}$ . The

camera employs a Rockwell 256x256 HgCdTe device whose low noise characteristics and a large size make it remarkably similar in operation to an optical CCD. The 3C 65 observations consisted of 35 guided exposures of 2 minutes each, and the 3C 437 consisted of 77 guided exposures of 2 minutes each. Between each short exposure the telescope was moved 10-20", through a sequence of positions forming a rectilinear mosaic, with the target object kept near the central region of the array throughout the entire sequence. During the observations, the atmospheric conditions were photometric with sub-arcsecond seeing.

The reduction of the infrared images employed statistical techniques to decouple the chip response from the varying sky background. For each exposure a background pattern was constructed through median averaging of normalized versions of the six preceding and six following frames. After background subtraction, the frames were coregistered and co-added. The entire process of median flat fielding, coregistration and co-adding was then repeated, after masking bad pixels, cosmic rays and astronomical objects identified during the first iteration. Photometric calibration of the co-added images was achieved through observations of standards from the list of Elias et al (1982).

The final co-added images are of very high quality. In this type of study, the large field of view of the NICMOS-3 device represents a significant advantage over previous generations of infrared arrays, for two reasons. First, the large field of view facilitates the detection of bright field objects enabling the individual exposures to be coregistered with sub-pixel accuracy, and the point spread function to be reliably determined. Stellar field objects on our images show gaussian profiles with FWHM

$\approx 0.6''$ . Second, the minimum pattern spacing determines the largest scale upon which emission from the object can be decoupled from the sky background in the median-flat-fielding process. A pattern spacing of  $10''$  or larger can be used with the NICMOS-3, thereby allowing the accurate detection of faint galactic emission out to a radii of several arcseconds.

## 4.5 Morphological Analysis

### 4.5.1 Gross Morphological Features

The infrared images of 3C 65 and 3C 437 show strikingly normal morphologies. The field of 3C 65 contains a faint object roughly  $3.0''$  west of 3C 65 lying directly along the radio axis. This object has a blue SED that is consistent with the SED of aligned emission seen in the sample of  $z = 1$  radio galaxies studied by Rigler et al. (1991), and may represent an example of detached aligned emission associated with the radio jet (see Chapter 5). The field of 3C 437 contains a object  $2.6''$  southwest of 3C 437 with a position angle roughly  $20^\circ$  north of the southeast radio axis and an unknown SED. Preliminary radial surface brightness profiles of 3C 65 and 3C 437, obtained by taking the median pixel values in circular annuli, are well fit by a deVaucouleurs  $r^{1/4}$  law over a large dynamic range, extending from radii just outside the seeing disk to radii at which sky noise dominates (see Figure 4.2). However, the surface brightness profiles at radii interior to the seeing disk are in excess of a simple extension of the seeing-convolved deVaucouleurs  $r^{1/4}$  law to the center. These central surface brightness excesses can be accounted for, however,

with the addition of a nuclear point source having approximately 10% of the flux of the main galaxy. Thus, the initial inspection of the surface brightness profiles of 3C 65 and 3C 437 suggests that they are consistent with being gE galaxies with the possible addition of a not unreasonable nuclear source. In the next section, we describe a surface fitting technique used to more precisely constrain the values of the deVaucouleurs  $r^{1/4}$  parameters.

#### 4.5.2 Surface Fitting Procedure

The general technique involved in the surface fitting procedure was to compare each galaxy image to a suite of simulated model images, where each model image consists of a seeing-convolved deVaucouleurs surface and a nuclear point source. Each model was evaluated on the basis of a  $\chi^2$  statistic based on the difference between data and model, and an acceptable range of parameter values was determined from the set of best fitting models. The procedure is described in greater detail below.

The data frame  $D(x,y)$  was constructed directly from the image made by co-adding the individual processed exposures. The co-add was expanded by a factor of three along both axes using bilinear interpolation, resulting in a plate scale of 0.0971 arcseconds pixel<sup>-1</sup>. A 128×128 pixel (12.5"×12.5") box centered on the position of peak surface brightness of the object was extracted. All identifiable field objects in this box were masked with circular apertures, and pixels within these apertures were

subsequently ignored by the model fitting algorithm. A point spread function frame was similarly constructed using a bright star in the field of the co-added image.

A suite of 128x128 pixel model frames  $M_i(x,y)$  was generated. Each model consists of the superposition of (1) an elliptical deVaucouleurs surface parameterized by the central position  $(x_0,y_0)$ , the ellipticity  $\epsilon$ , the position angle of the semi-major axis  $\theta$ , and the effective radius  $r_e$  (defined along the axis  $45^\circ$  from the semi-major axis), and (2) a simulated nuclear point source parameterized by the fractional contribution of the nuclear point source flux to the total flux within the frame,  $\alpha$ . Each model was convolved with the point spread function frame using a fast-fourier transform algorithm, and normalized to have the same total flux as the data frame  $D(x,y)$ .

For each model, a value of  $\chi^2 = v^{-1} \sum \{D(x,y) - M_i(x,y)\}^2$ , where  $v \equiv$  number of degrees of freedom, was calculated within a circular aperture of 6". The best fitting parameters are taken from the model that had the minimum value of  $\chi^2$ . In the case of both galaxies, the high quality of the model fit is demonstrated by the fact that the minimum value of  $\chi^2 \approx \sigma^2$ , the value expected to arise purely from fluctuations in the sky background. The one-sigma uncertainties in the parameter values correspond to the set of models whose  $\chi^2$  values do not exceed the minimum by an amount greater than that corresponding to 84% confidence levels. Inspection of the residual images (Figure 4.1, right-hand panels) verifies that the fits are good over the entire spatial extent of the  $12.5'' \times 12.5''$  frames. Finally, the entire analysis was carried out on images in which the background had been artificially modified by

amounts consistent with the uncertainty in the background determination. It was found that the resulting systematic variation in the best fitting model parameters was insignificant ( $\approx 10\%$  and  $\approx 20\%$  for 3C 65 and 3C 437 respectively). The values of the best fitting deVaucouleurs  $r^{1/4}$  parameters  $\mu_e$  and  $\log r_e$  are listed in Table 4.1 along with their formal errors. The errors in the two parameters are strongly coupled, however, and are more properly described by ellipses, as shown in Figure 4.3.

## 4.6 Discussion

Our model surface fitting analysis of the infrared images of the two quiescent radio galaxies 3C 65 ( $z = 1.176$ ) and 3C 437 ( $z = 1.480$ ) leads us to the following interesting points:

### 4.6.1 Quality of Fit of gE Models.

Rigler et al. (1991) showed that the members of a statistical sample at  $z = 1$  show the signature of a centrally concentrated symmetric red component having an approximately gE-like SED, as expected if the infrared light of high-redshift radio galaxies is dominated by mature stellar populations (Lilly & Longair 1984; Lilly 1989). In this chapter, we have found that the infrared morphologies of two red systems are well-fit by deVaucouleurs  $r^{1/4}$  laws characteristic of gE galaxies. We therefore conclude that the infrared morphologies of these two galaxies (1) are consistent *in detail* with them being gE-like galaxies, and (2) by extension, suggest that the

symmetric round component identified by Rigler et al (1992) may be associated with gE-like stellar populations in essentially all high-redshift radio galaxies.

#### 4.6.2 Comparison with Lower Redshift Systems

For each galaxy, we have plotted the best fitting scale size and surface brightness values on the  $\mu_e$ - $\log r_e$  plane (Figure 4.3) and compared them to the loci of present epoch brightest cluster members (BCMs; Schombert 1987, Oegerle & Hoessel 1991, and Kormendy 1980) and low-redshift radio galaxies (Lilly & Prestage 1987, Lilly et al. 1984), including in the latter both FRI and FRII sources. The position of the high-redshift radio galaxies on this diagram is dependent on  $\Omega_o$  and  $\Lambda_o$ , as indicated on the figure, and for the three "reasonable" standard cosmological models shown, the high-redshift radio galaxies lie very close to the low-redshift radio galaxies and present epoch BCMs.

##### 4.6.2.1 Stellar Evolution and $q_o$

A comparison of the photometric parameters of the high- and low-redshift galaxies can in principle offer constraints on  $q_o$  and  $\Lambda_o$ . Such a comparison is of course limited by the inherent uncertainty in associating the high- and low-redshift systems, as well as by the largely unconstrained effects of stellar and dynamical evolution. Nevertheless, certain features in Figure 4.3 are worth pointing out.

First, the errors in  $\mu_e$  and  $\log r_e$ , though large, are strongly correlated and are represented on the diagram as highly-elongated ellipses oriented roughly parallel to the standard  $\mu_e$ - $\log r_e$  relation. Second, we note that under conditions of homology, any merging activity acts to shift galaxies in a direction that is also roughly parallel to the standard  $\mu_e$ - $\log r_e$  relation. Thus, if merging is homologous (or if none has occurred), we could relate the degree of stellar evolution to  $q_o$  by requiring that stellar evolution move the objects down on to the locus of low-redshift radio galaxies and BCMs. Based on the two galaxies presented here, a model with  $q_o = 0.5$  ( $\Lambda = 0$ ) is consistent with about 0 to 1 mag of stellar evolution occurring between the two epochs, while about 0.5 to 1.5 mag of stellar evolution is implied if  $q_o = 0$  ( $\Lambda = 0$ ) and 1.5 mag if  $\Lambda > 0$ . These amounts of stellar evolution implied are quite reasonable, lying within the range expected for passive evolution in an initial burst model of star formation,  $\Delta m = (1.41 - 0.33x) \ln(t_1/t_0)$ , where  $t_1/t_0 \approx 1/3$  and  $0 < x < 1.35$  (Gunn & Tinsley 1976).

#### 4.6.2.2 Tolman Test for Universal Expansion

The photometric parameters of high-redshift galaxies can in principle provide a test of the classic Tolman prediction that bolometric surface brightness dims as  $(1+z)^{-4}$  due to Universal expansion (see Hubble & Tolman 1935). This test is difficult to make because the vector corresponding to the Tolman signal on the  $\mu_e$ - $\log r_e$  diagram also lies roughly parallel to both the standard  $\mu_e$ - $\log r_e$  relation for ellipticals and the homologous merging track. Sandage and Perelmuter (1990a,

1990b, and 1991), for example, have attempted to make use of the small difference between the slopes of the Tolman vector and the standard relation in order to remove this ambiguity. The two radio galaxies presented here are of sufficiently high redshift, however, that the Tolman vector becomes large enough to allow the adoption of a different approach. In a non-expanding Universe, the high-redshift radio galaxies would lie at the extreme end of the distribution of BCMs and low-redshift radio galaxies on the  $\mu_e$ - $\log r_e$  diagram. Evolutionary effects would be expected, if anything, to have made them still larger and of lower surface brightness, so that by the present epoch, 3C 65 and 3C 437, would be larger and fainter than any known galaxy. While the possibility that these are such extreme objects cannot be ruled out, a non-expanding Universe seems rather unlikely.

#### 4.7 Conclusions

A model surface fitting analysis of the infrared surface brightness profiles of two high-redshift radio galaxies 3C 65 ( $z = 1.176$ ) and 3C 437 ( $z = 1.480$ ) has shown that:

- (1) The infrared morphologies are well-fit by a de Vaucouleurs  $r^{i/4}$  law characteristic of gE-like galaxies.
- (2) The measured photometric parameters are comparable to those of brightest cluster members (BCMs) and low-redshift radio galaxies for standard cosmologies.
- (3) The small displacement of these galaxies from low-redshift BCMs and

radio galaxies on the  $\mu_e$ - $\log r_e$  plane suggests that little or no stellar evolution (0 to 1 mag) is required in a cosmology with  $q_0 = 0.5$  ( $\Lambda = 0$ ), while a slightly higher degree of stellar evolution (0.5 to 1.5 mag) is implied in a model with  $q_0 = 0$  ( $\Lambda = 0$ ), or models with  $\Lambda > 0$ .

(4) A non-expanding cosmology is unlikely because it would require the high-redshift systems to lie at the extreme end of the distribution of properties of local gE galaxies. The effects of stellar and/or dynamical evolution would be to make these objects even more extreme.

In Chapter 3 (and in Rigler et al 1992) we identified a symmetric round component dominating the infrared morphologies of a complete sample of  $z \approx 1$  radio galaxies. The results presented in this chapter provide strong evidence that the morphology of the round component is consistent *in detail* with being gE-like galaxies. Furthermore, these results demonstrate that the *photometric parameters of high-redshift radio galaxies can be accurately measured from high-quality infrared images*, and suggest that the reddest radio galaxies will offer the most promising targets for studies of elliptical galaxies at high-redshift.

#### References for Chapter 4

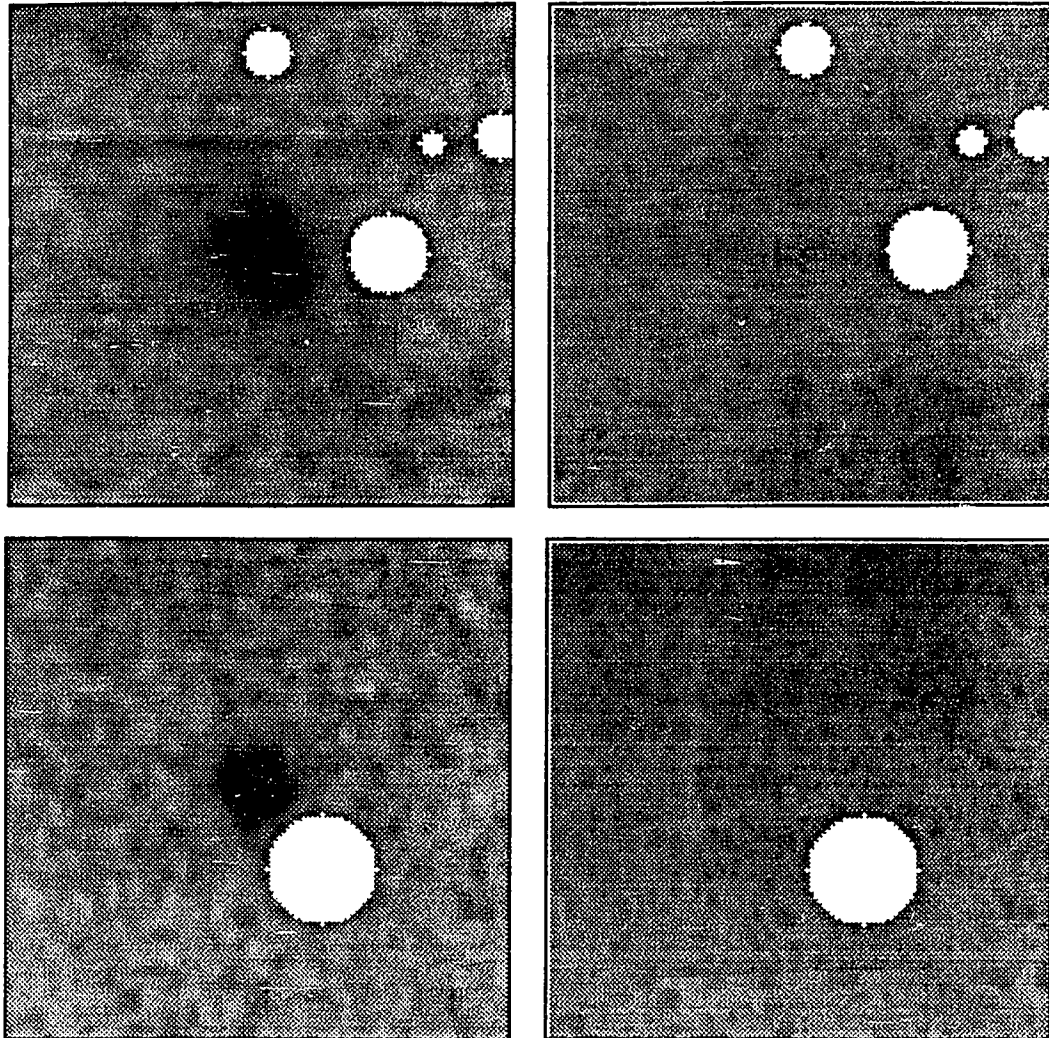
- Burstein, D., Davies, R.L., Dressler, A., Faber, S.M., Stone, R.P.S.,  
Chambers, K.C., Miley, G., & van Breugel, W. 1987, *Nature*, **329**, 609
- Daly, R. 1992, *ApJ*, in press
- Djorgovski, S., & Davis, M. 1987, *ApJ*, **313**, 59
- Djorgovski, S., & Spinrad, H. 1981, *ApJ*, **251**, 417
- Elias, J.H., Frogel, J.A., Mathews, K. & Neugebauer, G. 1982, *AJ*, **87**, 1029
- Gunn, J.E., & Tinsley, B.M. 1976, *ApJ*, **210**, 1
- Hamabe, M., & Kormendy, J. 1987, in IAU 127, "Structure and Dynamics of  
Elliptical Galaxies", ed. by de Zeeuw, T., (Kluwer: Dordrecht), 379
- Hodapp, K.-W., Rayner, J., Irwin, E. 1992, *PASP*, in press
- Hubble, E., & Tolman, R.C. 1935, *ApJ*, **82**, 302
- Kormendy, J. 1980, in SAAS-FEE 12, "Morphology and Dynamics of Galaxies",  
ed. by Martinet, L. & Mayor, M., Geneva Observatory, 113.
- Lilly, S.J. 1989, *ApJ*, **340**, 77
- Lilly, S.J., & Longair, M.S. 1984, *MNRAS*, **211**, 833
- Lilly, S.J., McLean, I.S., & Longair, M.S. 1984, *MNRAS*, **209**, 401
- Lilly, S.J., & Prestage, R.M. 1987, *MNRAS*, **225**, 531
- Lynden-Bell, D., Terlevich, R.J., & Wegner, G. 1987, *ApJ Supp*, **64**, 601
- McCarthy, P.J., van Breugel, W., Spinrad, H., & Djorgovski, S. 1987, *ApJ*,  
**321**, L29
- Oegerle, W.R., & Hoessel, J.G. 1991, *ApJ*, **375**, 15
- Rigler, M.A., Lilly, S.J., Stockton, A., Hammer, F., Le Fèvre, O. 1992, *ApJ*, **385**, 61
- Sandage, A., & Perelmuter, J.-M. 1990a, *ApJ*, **350**, 481
- Sandage, A., & Perelmuter, J.-M. 1990b, *ApJ*, **361**, 1

Sandage, A., & Perelmuter, J.-M. 1991, ApJ, **370**, 455

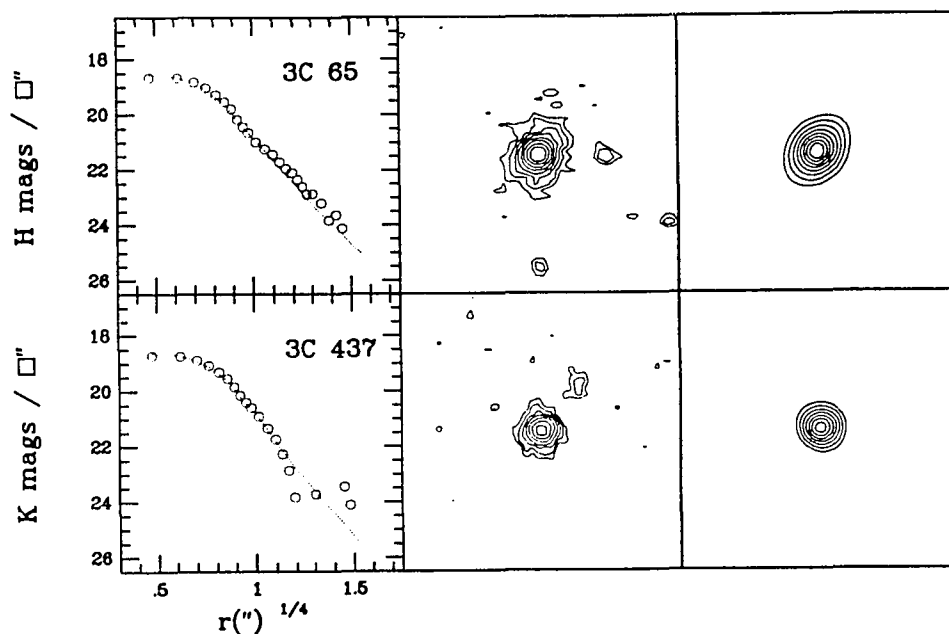
Schombert, J.M. 1987, ApJ Supp, **64**, 643

Table 4.1: Surface Photometry

3C	mag	nuc	$\mu_e$	$\log r_e$ (")
65	18.00 (H)	0.1	22.6 (0.5)	0.25 (0.16)
437	18.10 (K)	0.1	21.4 (0.9)	0.04 (0.20)



**Figure 4.1**—The infrared images of the radio galaxies 3C 65 ( $z = 1.176$ ; H band; upper left panel) and 3C 437 ( $z = 1.480$ ; K' band; lower left panel) used in the model surface fitting analysis. The images are 12.4" square, and oriented roughly NSEW, with north at the top and east at the left. To the right of each galaxy, the residual image resulting from the subtraction of the best fitting model is displayed. The residual images are dominated by noise throughout, which suggests that the data are well-fit by the models over the entire spatial extent of the frames.



**Figure 4.2**—Montage of the model surface fitting analysis of 3C 65 ( $z = 1.176$ ; H band; upper set of panels) and 3C 437 ( $z = 1.480$ ; K' band; lower set of panels). The central panels display the data images, and right-hand panels display best-fitting model images. Each image is  $12.4''$  square, and oriented roughly NSEW, with north at the top and east at the left. In both images the FWHM of the seeing point spread function is about  $0.6''$ . Contours are plotted in logarithmic surface brightness (at root 2 intervals). The lowest contours shown are  $21.64$  H mags/ $''^2$  and  $21.08$  K' mags/ $''^2$  for 3C 65 and 3C 437 respectively. The left-hand panels display the radial surface brightness profiles of the data (*open circles*) and of the best-fitting model (*dotted line*).

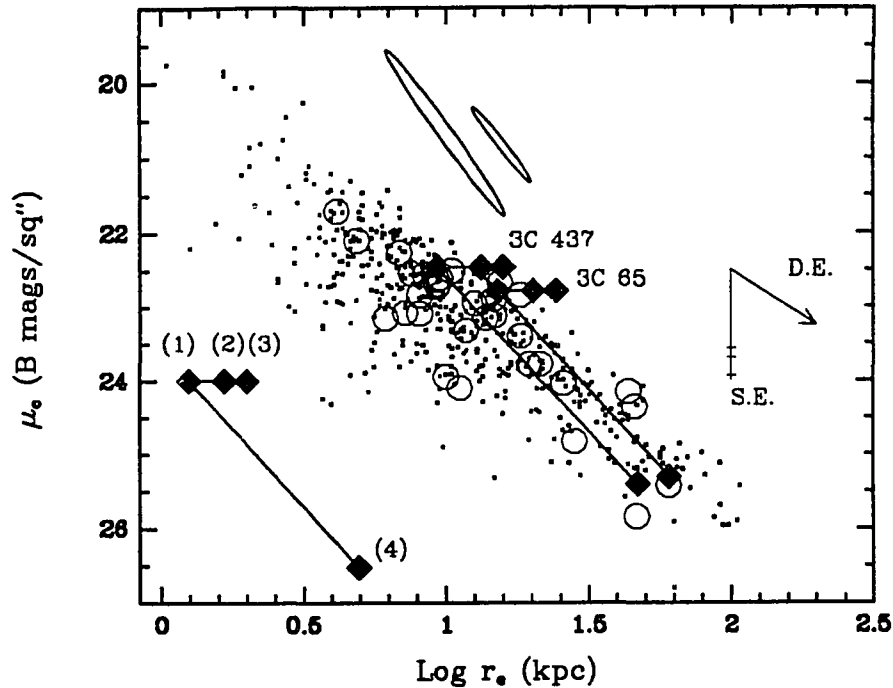


Figure 4.3—The  $\mu_e$ - $\log r_e$  diagram for elliptical galaxies (*small x's*), BCM's (*small open squares*), and low-redshift radio galaxies (*large open circles*), to which we have added new data points for the radio galaxies 3C 65 ( $z = 1.176$ ) and 3C 437 ( $z = 1.480$ ) based on our model surface fitting analysis. The position of the high-redshift galaxies on the diagram is dependent on the cosmological geometry, and here we have plotted each galaxy as a set of four points corresponding to four cosmological models (*large solid diamonds connected by solid lines*): (1)  $\Omega_o = 1$ ,  $\lambda_o = 0$ , (2)  $\Omega_o = 0$ ,  $\lambda_o = 0$ , (3)  $\Omega_o = 0.1$ ,  $\lambda_o = 0.9$ , and (4) a non-expanding Universe model (see legend at lower left). The error ellipses corresponding to one sigma (84% confidence level) are displayed in a position 2 magnitudes above the "model 1" point for each galaxy. Also shown is a vector indicating the direction of dynamical evolution (*labelled D.E.*) for homologous merging, as well as a vector indicating the magnitude of passive stellar evolution (*labelled S.E.*) in an initial burst model  $\Delta m = (1.41 - 0.33x) \ln t_1/t_0$  where  $t_1/t_0 \approx 0.33$  with tickmarks corresponding to values for the stellar initial mass function  $x = 0, 1$ , and 1.35 (Gunn and Tinsley 1976). In interpreting this figure, it is important to note that the error ellipses, the homologous merging vector (*D.E.*) and the Tolman signal (i.e., the line connecting models 1 and 4), are all oriented roughly parallel to the slope of the standard  $\mu_e$ - $\log r_e$  relation for ellipticals and BCMs.

## CHAPTER 5: DETACHED ALIGNED REGIONS OF EMISSION

Radio galaxies with  $z > 0.8$  display active phenomena that are not seen in systems at lower redshift. It has been known for some time that the high-redshift systems span a wide range in optical-to-infrared colors. Optical CCD images reveal a variety of continuum and emission line morphologies, with a tendency toward elongation and multimodel structure. The discovery that the elongated morphologies tend to be aligned with the radio axis (the "alignment effect"; McCarthy et al. 1987b; Chambers et al. 1987) demonstrated that the mechanism responsible for the activity is closely associated with the radio sources. This activity must be transient in nature since the radio source lifetimes are expected to be no more than a few times  $10^8$  years (e.g., Woltjer 1990) and possibly as short as a few times  $10^7$  years based on the typical separations of the radio lobes and properties of the radio bridges (Daly 1992a; Alexander & Leahy 1987).

To date, the mechanism or mechanisms responsible for the alignment effect emission have not been established. Several theoretical models have been discussed, including models involving (a) radio-jet-induced star formation, (Rees 1989; de Young 1989; Begelman & Cioffi 1989; Daly 1990; Bithel & Rees 1990) (b) scattering of anisotropic light from a central source by electrons or dust (Fabian 1989; Daly 1992a) (c) inverse Compton scattering of cosmic microwave background photons by relativistic electrons (Daly 1992b), and (d) synchrotron radiation (see Daly 1992c). Recent observational efforts include the possible detection of ultraviolet stellar absorption features in the combined spectra of selected  $z \gg 1$  radio galaxies

(Chambers & McCarthy 1990), which implies a stellar origin, and the detection of polarized emission in certain radio galaxies (di Seregho Allighieri, et al 1989; Scarrot et al. 1990; Jannuzi & Elston 1991), which suggests some scattering of light from the central source. The inverse Compton scattering model is also attractive, because it agrees well with the observed correlations between optical-to-infrared color and radio spectral index (Lilly 1989) and between emission line luminosity and radio power. It is entirely possible that more than one mechanism is in operation from galaxy to galaxy, or even within the same galaxy.

Hitherto, an important problem has been that observations of the aligned component have generally included light from the entire galaxy, or from regions of emission extending continuously from the center (Chambers & McCarthy 1990, di Seregho Allighieri, et al 1989; Scarrot et al. 1990; Jannuzi & Elston 1991). The contribution of a central nuclear source and the underlying stellar population to these measurements might be quite large. Indeed, the optical surface brightness distribution is often peaked at the center of the galaxy, even at very short wavelengths. Examples are known, however, of detached regions of aligned emission, which offer the prospect of studying the aligned emission component in relative isolation. While it is possible that these represent an atypical form of the alignment effect in operation, we present in this chapter the spectral energy distributions of two detached components lying in the fields of the galaxies 3C 65 ( $z = 1.176$ ) and 3C 326.1, which suggests that they are similar to the aligned component of the complete  $z \approx 1$  3C sample (Rigler et al 1991; see also Chapter 3).

## 5.1 The Blue Object Near 3C 65

The field of 3C 65 contains a nearby blue object which is likely to be an example of a detached region of alignment effect emission. This galaxy is relatively quiescent, having the reddest colors in the  $z \approx 1$  sample, and little or no [OII]  $\lambda 3727$  line emission. A montage of optical and infrared images is presented in Figure 5.1 including a continuum-free [OII]  $\lambda 3727$  image, and V, R and H images corresponding to rest-frame continua near 2500 Å, 3200 Å, and 8000 Å, respectively, and narrow-band images corresponding to continua just shortward and longward of the 4000Å break. The H band image (UH/NICMOS-3 at CFHT) and the V and R band images are of high quality. In comparison, the narrow-band continuum and line-only images are of poor quality in terms of depth and seeing. The V, R, SC and H images show a blue object lying along the western radio axis roughly 3" west of the surface brightness peak of the main galaxy. We have not obtained a redshift for the blue object, and there is little or no line emission present in the narrow band filter centered on [OII]  $\lambda 3727$  from either object. It is therefore possible that this alignment results from a chance superposition. We suggest, however, that the blue object is likely to be an case of the alignment effect operating in a region isolated from the main galaxy.

We have determined the spectral energy distribution of the main galaxy and nearby blue object from co-smoothed versions of the V, R and H images with FWHM  $\approx 0.7''$ . Photometric measurements were made within synthetic apertures of 1" diameter centered on three positions: that of the main galaxy, the blue aligned

object 3" to the west of the main galaxy, and the field 3" to the east of the main galaxy. The latter provided an estimate of the emission from the main galaxy that is present within the aperture centered on the blue aligned object. Within the 1" apertures, the main galaxy was found to have  $H = 20.7$ ,  $R = 24.0$ , and  $V = 24.7$  (in AB magnitudes), while the blue object (with the fluxes measured within the apertures located on the azimuthally opposite side of 3C 65 subtracted) was found to have  $H = 23.4$ ,  $R = 24.9$ , and  $V = 24.7$  (in AB magnitudes). The spectral energy distributions of the main galaxy and the blue object are plotted in Figure 5.2, along with scaled versions of elliptical and irregular galaxy models for comparison (Coleman, Wu & Weedman 1980). The spectral energy distribution of the blue object is consistent with a power law of  $f_\nu \approx \nu^{-1.2}$ , (between rest-frame 2500 Å to 7600 Å), and also with the spectral energy distribution of an irregular-like galaxy.

## 5.2 The Detached Component of 3C 326.1

The galaxy 3C 326.1 ( $z = 1.82$ ) had already attracted a great deal of attention prior to this dissertation because it is associated with a large powerful Ly $\alpha$  emission cloud. McCarthy et al (1987a) suggested that the galaxy might be a protogalaxy on the basis of early optical CCD images which showed the Ly $\alpha$  cloud to be diffuse. Several faint optical continuum components were present, but the cloud seemed to lack any obvious central condensation. Indeed, during an early stage of its formation, a galaxy might well very well consist of multiple star-forming regions embedded in a collapsing gas cloud. Subsequent infrared observations, however, identified a

$K \approx 19$  infrared source associated with one of the optical components located approximately midway between the radio lobes (Lilly & McLean 1987). The  $K$  magnitude of this component lies on the  $K-z$  relation, has a spectral energy distribution similar to other high-redshift 3C radio galaxies, and is now regarded as the main galaxy. The system is most easily interpreted as an evolved population undergoing a burst of alignment effect activity, possibly star formation. An improved  $\text{Ly}\alpha$  image was also obtained by Lilly (1990) which showed that the  $\text{Ly}\alpha$  emission is actually strongly peaked on the position of the western radio hot spot, which is co-located with one of the optical components (Lilly 1990) lying roughly 3" west of the main galaxy. While these discoveries removed much of the original motivation for believing this system to be a protogalaxy, 3C 326.1 continues to be an extremely interesting system because it includes an aligned component that is separated from the main galaxy.

As part of this dissertation, the author obtained an improved, high-resolution  $K'$  image of the 3C 326.1 field. The  $K'$  image consists of  $36 \times 3$  minute exposures taken with the UH/NICMOS-3 array camera at the UH 2.2 m telescope during a run in May 1991 at a plate scale of 0.224" per pixel. From this image, a faint infrared source has been identified with the aligned component at the radio hot spot. A montage of the 3C 326.1 field is shown in Figure 5.3 including  $U'$ , B and  $K$  band images. The various field objects are readily identified as galactic stars and low- to moderate-redshift galaxies on the basis of their optical-to-infrared colors. A continuum-free  $\text{Ly}\alpha$  image was constructed using the  $U'$  and B band images.

When combined with existing data sets, the new images constrained the spectral energy distributions of the main galaxy and the aligned component. The spectral

energy distributions were constructed through photometric measurements of a set of co-smoothed versions of the images using 2" diameter apertures. These are displayed in Figure 5.4, along with spectral energy distributions of elliptical and irregular model galaxies for comparison (Coleman, Wu & Weedman 1980).

## 5.4 Conclusions

We have determined the small-aperture spectral energy distributions of the morphological components of the 3C 65 and 3C 326.1 systems. The main galaxy components of both systems have spectral energy distributions that are not unlike those seen in the  $z \approx 1$  sample and other high-redshift radio galaxies, and are consistent with being dominated by a gE-like spectral energy distribution in the infrared. The detached blue aligned components of both systems have spectral energy distributions which can be fit by either an irregular-like spectral energy distribution, such as might be expected in a scenario of jet-induced star formation, or by a power law of slope  $f_\nu \approx -1$  (between rest-frame 2500Å and 8000Å), which is consistent with various non-thermal models for the alignment effect.

This result is entirely consistent with the spectral energy distribution of the aligned component of the  $z \approx 1$  3C sample as determined from a spectral decomposition based a moment analysis of the light distributions measured within 4" apertures centered on the main galaxy (Rigler et al 1991; Chapter 3, this dissertation). In the moment analysis, the spectral energy distributions were intentionally constructed a crude fashion because the aim of the experiment was to relate the light distributions

of the sample to the large aperture  $K-z$  relation. The fact that similar results are obtained here using smaller aperture photometry of selected morphological components can be taken as additional justification for the moment analysis method. Conversely, it suggests that the emission in the detached aligned components is produced by the same basic mechanism responsible for the aligned morphologies seen in the sample, which tend to be of the elongated, continuous variety. Furthermore, the general similarity between 3C 326.1 and the  $z \approx 1$  systems suggests that the conclusions drawn from the analysis of the  $z \approx 1$  3C sample might extend to radio galaxies with redshifts as high as  $z \approx 2$ . Detached aligned regions such as these offer attractive targets for further studies of the alignment effect because measurements can be made in apertures relatively free from contamination by emission from the main galaxy.

## References for Chapter 5

- Alexander, P., & Leahy, P.J. 1987, MNRAS, **225**, 1P
- Begelman, M.C., & Cioffi, D. 1989, ApJ, **345**, L21
- Bithel, M., & Rees, M. 1990, MNRAS, **242**, 570
- Chambers, K.C., McCarthy, P.J. 1990, ApJ, **354**, L9
- Chambers, K.C., Miley, G., & van Breugel, W. 1987, Nature, **329**, 609
- Coleman, G.D., Wu, C.-C., & Weedman, D.W. 1980, ApJS, **43**, 393
- Daly, R.A. 1990, ApJ, **355**, 416
- Daly, R.A. 1992a, in Testing the AGN Paradigm, ed. S. Holt, S. Neff, & M. Urry (New York: American Institute of Physics), 427
- Daly, R.A. 1992b, ApJ, **386**, L9
- Daly, R.A. 1992c, ApJ, in press
- de Young, D.S. 1989, ApJ, **342**, L59
- di Seregho Allighieri, S., Fosbury, R.A.E., Quinn, P.J., & Tadhunter, C.N. 1989, Nature, **341**, 307
- Fabian, A.C. 1989, MNRAS, **238**, 41P
- Jannuzi, B.T., & Elston, R. 1991, ApJ, **366**, L69
- Lilly, S.J. 1989, ApJ, **340**, 877
- Lilly, S.J. 1990, in ASP Conf. Ser. 9, The Evolution of the Universe of Galaxies, ed. R.G. Kron (Dordrecht: Kluwer), 344
- Lilly, S.J., & McLean, I.S. 1989, ApJ, **346**, L65
- McCarthy, P.J., Spinrad, H., Djorgovski, S., Strauss, M.A., van Breugel, W., & Liebert, J. 1987a, ApJ, **319**, L39
- McCarthy, P.J., van Breugel, W., Spinrad, H., & Djorgovski, S. 1987b, ApJ, **321**, L29

Rees, M.J. 1989, MNRAS, **239**, 1P

Rigler, M.A., Lilly, S.J., Stockton, A.N., Hammer, F., LeFevre, O. 1992, ApJ, **385**, 61

Scarrot, S.M., Rolph, C.D., & Tadhunter, C.N. 1990, MNRAS, **243**, 5P

Woltjer, L. 1990, in Saas-Fee Advanced Course 20, Active Galactic Nuclei, ed. T.J.-L. Courvoisier & M. Mayor (Springer-Verlag: Berlin Heidelberg 1990), 1

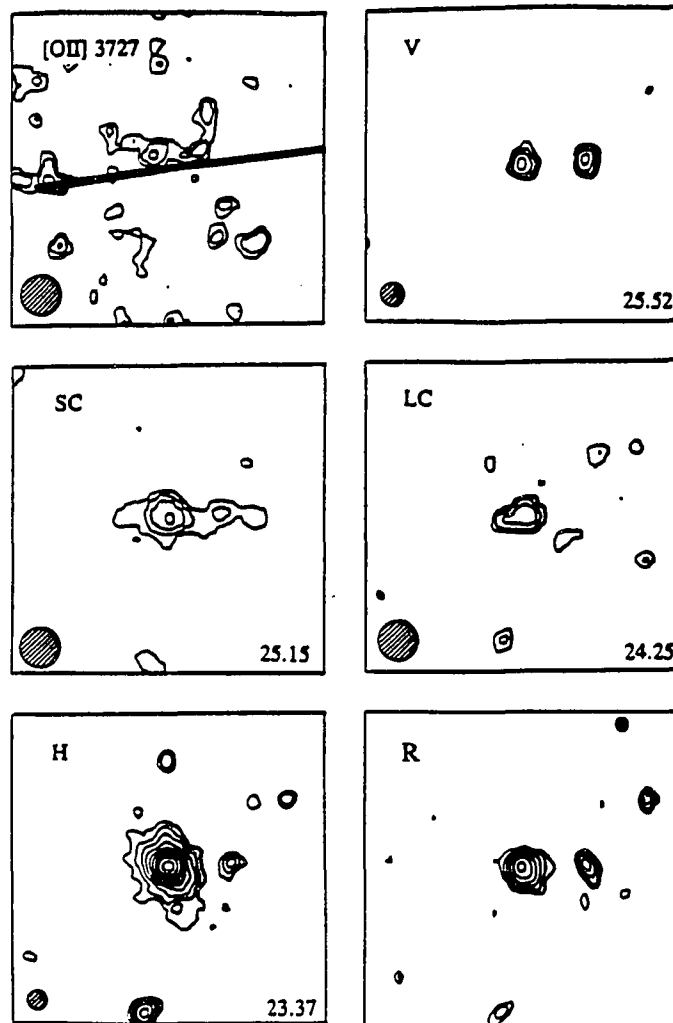


**Figure 5.1**—A montage of the unsmoothed multicolor images of 3C 65. The images are 15" square and are accurately coregistered. Orientation is within 1-2° of NSEW, with north at the top and east at the left. Contours are plotted in logarithmic surface brightness (at root 2 intervals in surface brightness). Images are identified by standard filter passbands except for LC and SC, which stand for the intermediate-band filters located above and below the 4000 Å spectral feature. The radio jet axis is sketched on the [OII]  $\lambda$ 3727 image. This figure shows the blue object 3" west of 3C 65 in the V, R, SC and H band filters, which may be an example of the alignment effect operating in a region that is detached from the main galaxy.

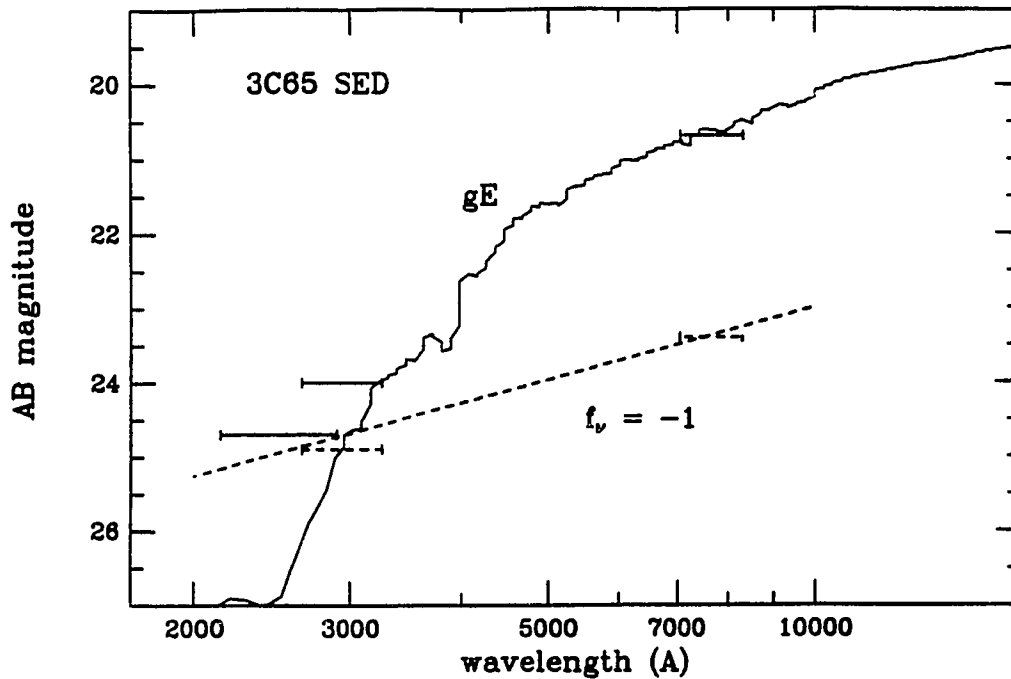


**Figure 5.2**—The small-aperture (1") spectral energy distributions of the main galaxy component of 3C 65 (*dotted line*) and the nearby blue object (*dashed line*), where the horizontal lines indicate the approximate bandpasses of the V, R and H filters. For comparison, the spectral energy distribution of a gE galaxy (Coleman et al. 1980) is shown passing through the H-band point of the main galaxy (*dotted line*), and a power law with a slope of  $f_{\nu} \approx -1$  is shown passing through the points of the blue object. The figure shows that the nearby blue object has roughly the same spectral energy distribution as the "aligned component" of the  $z = 1$  3C sample. This provides an independent justification for the moment analysis described in Chapter 3, and it suggests that detached aligned regions are not atypical examples of the alignment effect.

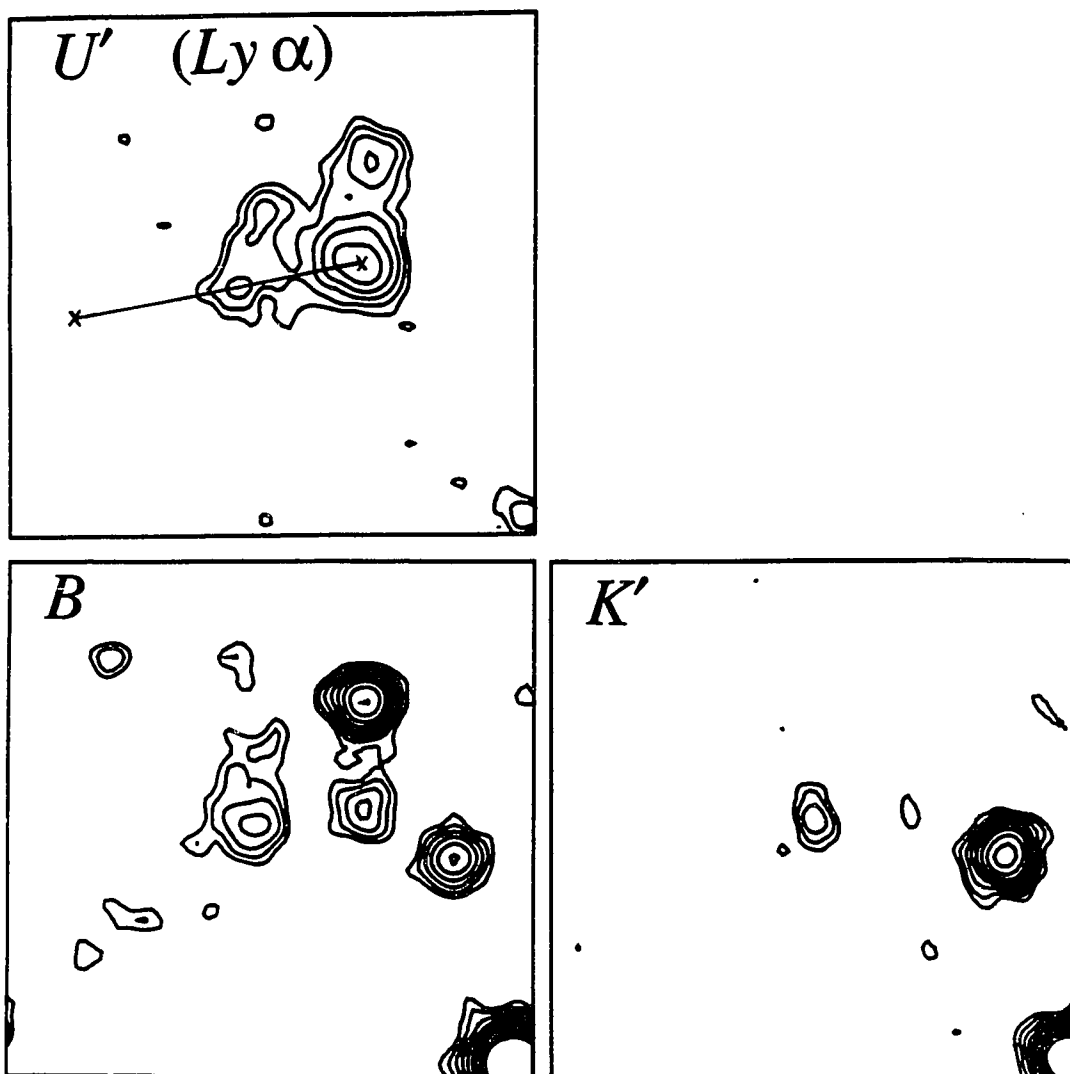


**Figure 5.3**—A montage of the unsmoothed multicolor images of 3C 326.1. The images are 18" square and are accurately coregistered. Orientation is within 1-2° of NSEW, with north at the top and east at the left. Contours are plotted in logarithmic surface brightness (at root 2 intervals in surface brightness). Images are identified by standard filter passbands, except for the U' image, which is an intermediate-band filter centered near the Ly $\alpha$  emission line. The radio jets are sketched on the U' image. The main galaxy component is labeled 'B', the aligned component collocated with the western hotspot is labeled 'C'. The objects 'A' and 'M' are foreground objects.

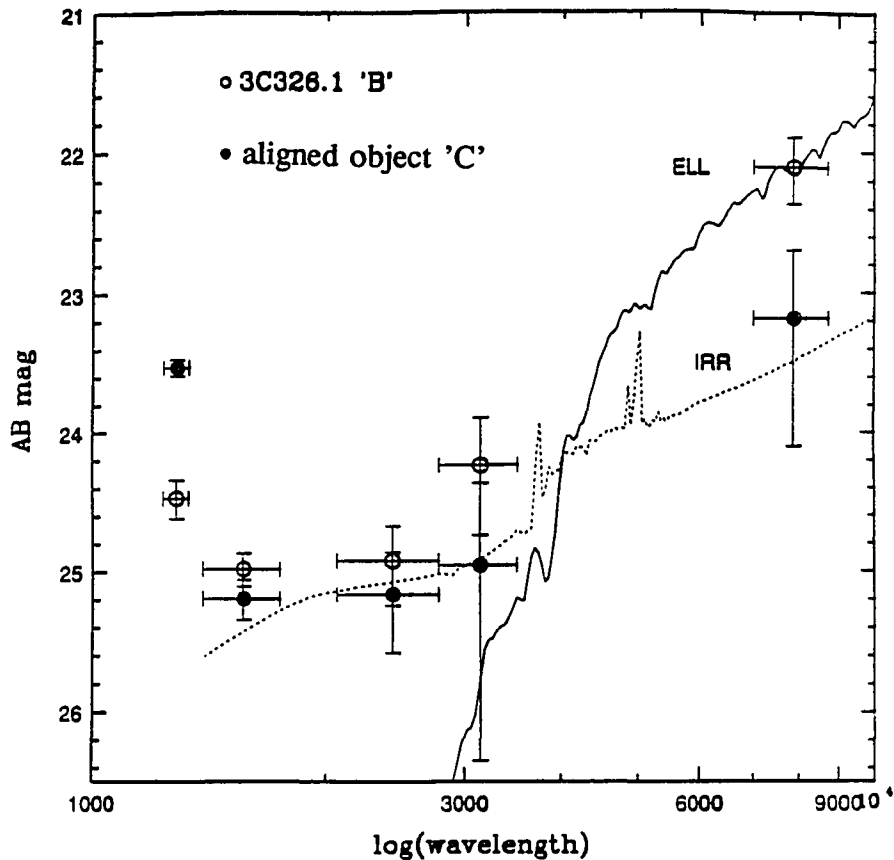


**Figure 5.4**—The small-aperture (2") spectral energy distributions of the main galaxy component of 3C 326.1 at  $z = 1.82$  (*open circles*) and the detached aligned component (*solid circles*), where the horizontal error bars indicate the approximate bandpasses of the filters U', B, R, I and K', and the vertical error bars indicate the photometric uncertainties. Note the presence of Ly $\alpha$  in the U' filter. For comparison, the spectral energy distribution of a gE galaxy (Coleman et al. 1980) is shown passing through the K' point of the main galaxy (*solid line*), and the spectral energy distribution of an irregular galaxy (Coleman et al. 1980) is shown passing through the points of the detached aligned component. The figure shows that the spectral energy distribution of the main galaxy component of 3C 326.1 is similar to those of other high-redshift radio galaxies, and the detached component has roughly the same spectral energy distribution as the "aligned component" in the  $z \approx 1$  sample. This suggests that the conclusions drawn from the analysis of the  $z = 1$  sample may extend to higher redshifts. Detached aligned components such as this offer attractive targets for future studies of the alignment effect.

## CHAPTER 6: CONCLUSIONS AND FUTURE WORK

### 6.1 Summary of Results

Qualitative and quantitative analysis of a homogeneous set of multicolor line and continuum images of a complete sample of 3C radio galaxies at  $0.8 < z < 1.3$ , as well as selected galaxies at higher redshifts, has led us to the following conclusions:

#### 6.1.1 Decomposition into Symmetric and Aligned Components

The infrared morphologies of the  $z \approx 1$  sample are much more symmetric than those at optical wavelengths. Although several of the infrared images are aligned with the radio axes, quantitative measures of the asymmetry show a progressive *reduction* as one goes from rest-frame  $2500 \text{ \AA}$  to  $1 \mu m$ , as is expected if the morphology of each galaxy is the superposition of two distinct morphological components: (1) a symmetric component which dominates at infrared wavelengths, and (2) an aligned "active" component dominant at UV-optical wavelengths. This result is consistent with the "old galaxy hypothesis" for these galaxies, whereby the small scatter in the  $K-z$  relation is produced by a homogeneous population of mature host galaxies which are currently undergoing varying degrees of activity associated with their radio sources. Typically, about 10% of the rest-frame  $1 \mu m$  light is produced by the active component, with the more active objects have larger contributions. This modest degree of contamination is consistent with the small scatter of the  $K-z$

relation. As expected, the most aligned objects are the ones with the bluest overall colors. The angular sizes of the infrared images of the radio galaxies are roughly consistent with the known sizes of the giant elliptical galaxies associated with powerful radio sources at low redshifts for reasonable cosmologies, i.e.,  $0.05 < q_o < 0.5$ . However, the accuracy of this measurement is generally limited by the presence of contamination due to an active component.

### **6.1.2 Spectral Energy Distribution of the Symmetric Component**

For the  $z \approx 1$  sample, a spectral decomposition based on these quantitative morphological parameters suggests that the "symmetric" component has a red spectral energy distribution similar to that of a gE galaxy, although the spectral decomposition is not unique.

### **6.1.3 Spectral Energy Distribution of the Aligned Component**

For the  $z \approx 1$  sample, a spectral decomposition based on the quantitative morphological parameters suggests that the "active" component, which dominates in the ultraviolet wave band and is usually roughly aligned with the radio source axis, has a spectral energy distribution with  $f_\nu \approx -0$  to  $-1$ , between  $2500 \text{ \AA}$  and  $1 \mu m$ . This form of the spectral energy distribution is consistent with various thermal and non-thermal models for the alignment effect.

### 6.1.4 Properties of the Most Quiescent Systems

The reddest member of the  $z \approx 1$  sample, 3C 65, which is the one expected to be least contaminated by an "active" component, shows a strikingly normal infrared morphology with a surface brightness profile that is well-fit by a deVaucouleurs  $r^{1/4}$  law. A model surface fitting routine yields characteristic photometric parameters that are comparable to those of BCM's and low-redshift radio galaxies for standard cosmologies. Similar results were obtained for another red galaxy, 3C 437 ( $z = 1.480$ ). The small displacement of these galaxies from low-redshift BCMs and radio galaxies on the  $\mu_e$ - $\log r_e$  plane suggests that little or no stellar evolution is required in a cosmology with  $q_0 = 0.5$  ( $\Lambda = 0$ ), while a modest degree of stellar evolution is implied in a model with  $q_0 = 0$  ( $\Lambda = 0$ ), or models with  $\Lambda > 0$ . The data appear to be inconsistent with a non-expanding cosmology.

### 6.1.5 Detached Aligned Regions of Emission

The morphologies of the active components display a great deal of variation from galaxy to galaxy, including examples of diffuse, centrally peaked emission extending along the radio axis, and examples of detached regions of emission lying along the radio axis. The latter may offer a unique opportunity to study the alignment effect in operation without contamination by the main galaxy. Examples of detached alignment morphology are provided by 3C 326.1 ( $z = 1.8$ ) and possibly by 3C 65 ( $z = 1.17$ ). The fields of these galaxies each show a nearby object lying

directly on the radio axis, having a spectral energy distribution with a slope of  $f_{\nu} \approx -1$ . This spectral energy distribution is consistent with theoretical models for the alignment effect, and is similar to the that of the aligned component in the  $z \approx 1$  sample. This suggests that mechanisms operating in the detached aligned regions of emission are not atypical of the alignment effect.

### 6.1.6 Red Companions

A significant fraction (5/13) of the radio galaxies in the  $z \approx 1$  sample are accompanied by nearby red objects that are prominent on the infrared images and which are likely to be companion galaxies. These are 1-2 mag fainter than the main galaxy, but are usually redder in overall color and usually have little or no associated [O II] emission. The presence of these possible red companions suggests that "conventional" triggers for the radio sources are still operating at  $z > 1$ , and that, regardless of the evolutionary state of the radio galaxy, at least some old galaxies exist around the central object.

## 6.2 Future Work

The research described above, the ongoing work of others in the field (see e.g., for key developments, Spinrad 1986; Lilly 1989; Bithel & Rees 1990; Chambers & Charlot 1990; Daly, R.A. 1990 & 1991; De Young 1989; Chambers & McCarthy 1990; di Seregho Allighieri, et al. 1989; Scarrot et al. 1990; Jannuzi & Elston 1991; Eisenhardt & Dickson 1992; Rawlings et al 1991; McCarthy et al 1992) has

prompted several issues, including: (a) Does the "old galaxy" interpretation of the  $K-z$  relationship extend to  $z \gg 1$ ? (b) Can a large number of relatively quiescent radio galaxies be found, particularly at redshifts  $z \gg 1$ , which look like gEs, and if so, can they be used to constrain cosmology and galaxy evolution? (c) What are the mechanisms for producing the aligned components, and are they best studied in systems showing detached regions of alignment? and (d) What is happening in the immediate environments of radio sources, particularly with regards to red companions, and how are the environments changing with redshift? These issues are discussed in turn below.

### **6.2.1 Extending to Higher Redshifts**

A key question for the future is whether the quantitative analysis of infrared morphologies will continue to support the "old galaxy hypothesis" at higher redshifts, where the cosmogonic issues become more acute. The  $K-z$  relation shows small scatter out to at least  $z = 2$  (see, e.g., Lilly 1991) and possibly out to  $z > 3$ . Work along these lines is being undertaken by other groups, and we have begun a program to carry out multicolor observations on samples of objects at these higher redshifts.

In the meantime, three cautionary comments are warranted: First, at higher redshifts, the infrared passbands are redshifted to shorter wavelengths and, within the framework of the "old galaxy hypothesis," asymmetries are expected to become more apparent as the aligned component contributes a greater fraction of the flux density. The small dispersion in the  $K-z$  relation persists to redshifts as high as  $z = 2$  and

beyond, and could be preserved even in a sample in which the average contamination approaches 40%, by which point the most extreme objects may have contaminations as high as 70%. As has been demonstrated, dramatic alignments can be produced by even by components that contribute much less than this. Second, at higher redshifts, various prominent emission lines such as [OIII]  $\lambda$ 5007 and H $\alpha$   $\lambda$ 6563 will be present within the standard bandpasses, which could introduce a contaminating aligned component. Indeed, there is a growing body of evidence, based on near infrared spectroscopy, that the broad-band near infrared flux of  $z \gg 1$  radio galaxies can include a substantial emission line contribution (10 to 80%; e.g., Eisenhardt & Dickson 1992; Rawlings et al 1991; McCarthy et al 1992). Third, it should be borne in mind that most of the galaxies that have had redshifts measured at  $z > 2$  have been selected on account of their "ultrasteep" radio spectra (e.g., Chambers et al 1988b; Chambers et al 1990; McCarthy et al 1991). There appears to be a correlation between the steepness of the radio spectral index and the strength of the active component (Lilly 1989), and hence one might expect that these objects are unusually active, and therefore more aligned than more typical radio galaxies. For these reasons, care must be taken to not over-interpret optical and infrared morphologies as necessarily implying young ages for all high-redshift radio galaxies.

### 6.2.2 Quiescent Radio Galaxies

The results of this dissertation generally support the "old galaxy hypothesis", in which essentially all radio galaxies have mature underlying stellar populations pro-

ducing the small scatter in the  $K-z$  relation. In this scenario, the reddest objects in any sample are expected to appear in the infrared as gEs in the sense that they will be most free from the emission causing the alignment effect. This prediction has been born out by the morphological analysis of the two quiescent radio galaxies 3C 65 (the reddest in the  $z \approx 1$  sample) and 3C 437, which shows their infrared morphologies to be consistent *in detail* with gE galaxies. There exists controversy as to whether the radio galaxies currently known at  $z \gg 1$  represent a uniform population of old galaxies, or if they include a number of forming protogalaxies in addition to older galaxies (the "range of ages" model), perhaps being exclusively protogalaxies at  $z > 3$ . Regardless, there is general agreement that the reddest objects in a sample at a given redshift are the oldest. For these reasons, the reddest objects offer the most promising targets for studies of high-redshift elliptical galaxies designed to provide cosmological and cosmogonical constraints.

Several candidates for high-redshift gEs are to be found in the 1 Jansky sample. The 1 Jansky sample is fainter than the 3C sample and extends to higher redshifts. More importantly, the 1 Jansky's are almost unique in the search for high-redshift systems in that they *were not selected on the basis of the steepness of radio index*, a criterion which (as mentioned above) introduces a bias towards the bluest, most active objects. Indeed, photometry of 1 Jansky "empty field" sources (Lilly 1989) has turned up six extremely red objects with  $1 < z < 2$ . These sources are ideal candidates for gE-like galaxies.

If these objects do turn out to be gE-like, it could be interesting to obtain infrared spectra of their  $4000 \text{ \AA}$  break features in order to constrain their ages. The

4000 Å break lies in the J-band for the three objects in the subsample with  $z \approx 1.8$ . The feature is sensitive to the elapsed time since the last major episode of star formation over a range of  $\approx 8$  Gyrs and is known to have undergone (at most) a modest change in red ellipticals between  $z = 0$  and  $z = 1$  (Hamilton 1985; Spinrad 1986; Dressler & Schectman 1987). At  $z \approx 2$ , the Universe is itself only 1.3 Gyr ( $q_o = 0.5$  and  $H_o = 100$ ) to 7 Gyr ( $q_o = 0$  and  $H_o = 50$ ) old. Age dating these galaxies might therefore provide powerful constraints on cosmology and galaxy evolution.

We note that the ages of the red companions of high-redshift radio galaxies are also of great interest. The advantages of studying them are threefold: First, for a sample at a given redshift, there are only a few quiescent (i.e, uncontaminated) radio galaxies suitable for study, whereas a significant fraction of any sample are expected have uncontaminated red companions. Secondly, these companions are generally fainter than the radio galaxies, having roughly  $L^*$  luminosities on the basis of their infrared magnitudes, and are therefore more representative of normal systems. Thirdly, selection effects associated with companions might be less important than for radio galaxies, since they are being selected merely because they are *in the vicinity* of a powerful radio galaxy.

### 6.2.3 Future Studies of the Alignment Effect

The mechanism responsible for the alignment effect is currently unknown. Different processes may be occurring in different galaxies, or even within a given galaxy. Hitherto, an important problem has been that data on the aligned com-

ponents has often included either the entire galaxy. Examples of detached, isolated regions of aligned emission are known, however, which offer the potential to avoid contamination by various components in the main galaxy. This dissertation included an analysis of the spectral energy distributions of two such examples, 3C 65 and 3C 326.1, and concluded that the processes operating in the detached regions are probably not atypical examples of the alignment effect. These types of objects are therefore extremely attractive targets for the future study of the alignment effect.

#### **6.2.4 The Environments of High-Redshift Radio Galaxies**

The immediate environment of high-redshift radio galaxies holds important implications for the connections between AGN's and high-redshift clusters. These systems tend to be morphologically complex, with extended optical continua and extended gaseous halos which often show dynamical structure (e.g., Spinrad 1989). Objects with a variety of colors are often present in the nearby fields of these systems. In the course of my research, the analysis of a multi-wavelength set of images allowed the interpretation of various morphological features such as red companions, isolated regions of aligned emission and foreground objects (e.g., as in the case of the M star in the foreground of 3C368; Rigler et al. 1991).

The morphology of the red component is sensitive to the presence and dynamical state of the old stellar populations, and is likely to be revealing activity in the inner few 100 kpc of a cluster or a forming cluster, such as tidal interactions, merging and cannibalism. Furthermore, there might be a trend toward increasing

morphological complexity with redshift, which may be indicative of a change in radio galaxy environments either through cluster evolution or through the operation of the radio galaxy selection process. Others have noted a possibly related trend toward increasing clumpiness of the intergalactic medium with redshift based on the rotation measure and depolarization distributions of the radio emission and the clumpiness of the Ly $\alpha$  emission (see, e.g., Pedelty et al. 1989; Spinrad 1989).

It is reasonable to expect that significant changes are occurring in the environments of powerful radio galaxies between  $z = 1$  and  $2$ , and for these changes to be related to the strong evolution observed in the radio luminosity function between these redshifts. Indeed, the co-moving density is peaked at  $z \approx 2$ . It is very unlikely that an epoch of major galaxy formation is responsible because of the evidence that all powerful radio galaxies formed at much earlier epochs. Rather, it may be an indication that the cluster or sub-cluster environment becomes conducive to the turn-on of radio sources around  $z = 2$ , and that further cluster evolution gradually results in a less hospitable environment. The cluster environment changes through processes such as the merging of subclusters, the cooling of intracluster gas and the relaxation of the potential well. Theoretical work indicates that AGN's require time to assemble and a source of fuel. The fuel may be supplied, for example, by cooling gas, which is later disrupted by the merging of sub-clusters (Fabian & Crawford 1991).

Changes in environments have been observed for low- to moderate-redshift radio sources. Powerful radio galaxies tend to inhabit rich environments at  $z < 1$ ,

and the environmental richness of radio galaxies and quasars has decreased since  $z = 0.5$  (Hill & Lilly 1990; Yee & Green 1987). Clusters themselves have evolved between  $z = 1$  and the present (e.g., see Gunn 1990). This trend implies that cluster evolution may play a fundamental role in the evolution of distant radio galaxies and it would be fascinating to investigate their environments over the range  $1 < z < 2$  where there is strong evolution in the radio luminosity function.

It is important, therefore, to study the immediate environments of radio galaxies with  $z \gg 1$  for four basic reasons: (a) to relate radio galaxies to each other and the general population at different redshifts through a comparison of their environments, (b) to explore the connections between AGN's and their environment over a critical part of the radio luminosity function, (c) to study the relationship between the environment and alignment effect processes, and (d) to investigate cluster evolution.

## References for Chapter 6

- Bithel, M., & Rees, M. 1990, MNRAS, **242**, 1P
- Chambers, K.C. & Charlot, S. 1990 ApJ, **348**, L1
- Chambers, K.C., McCarthy, P.J. 1990, ApJ, **354**, L9
- Chambers, K.C., Miley, G., & Joyce, R.R. 1988, ApJ, **329**, L75
- Chambers, K.C., Miley, G., & van Breugel, W. 1990, ApJ, **363**, 21
- Daly, R.A. 1990, ApJ, **355**, 416
- Daly, R.A. 1992, ApJ, in press
- De Young, D.S. 1989, ApJ, **342**, L59
- Dressler, A., & Schectman, S.A. 1987, AJ, **94**, 899
- Eisenhardt, P. & Dickson, M. 1992, ApJ, in press
- Fabian, A.C., & Crawford, C.S. 1991, MNRAS, **247**, 439
- Gunn, J.E. 1989, in NATO ASI series vol. 264, The Epoch of Galaxy Formation, Ed. C. Frenk et al. (Kluwer: Dordrecht), 167
- Hamilton, D. 1985, ApJ, **297**, 371
- Hill, G.J., & Lilly, S.J. 1990, ApJ, **367**, 1
- Jannuzi, B.T., & Elston, R. 1991, ApJ, **366**, L69
- Lilly S.J., 1989, ApJ, **340**, 77
- McCarthy, P.J., Elston, R., Eisenhardt, P. 1992, ApJ, in press
- McCarthy, P.J., van Breugel, W., Kapahi, V.K., & Subrahmanya, C.R. 1991, ApJ, **371**, 478
- Pedely, J.A., Rudnick, L., McCarthy, P.J., & Spinrad, H. 1989, A.J., **97**, 647
- Rawlings, S., Eales, S., & Lacey, M. 1991, MNRAS, **251**, 17P

Rigler, M.A., Lilly, S.J., Stockton, A.N., Hammer, F., Le Fèvre, O. 1991, ApJ, **385**, 61

Scarrot, S.M., Rolph, C.D., & Tadhunter, C.N. 1990, MNRAS, **243**, 5P

di Seregho Alligheri, S., Fosbury, R.A.E., Quinn, P.J., & Tadhunter, C.N. 1989, Nature, **341**, 307

Spinrad, H., 1986, PASP, **98**, 269

Spinrad, H. 1989, in NATO ASI series vol. 264, The Epoch of Galaxy Formation, Ed. C. Frenk et al. (Kluwer: Dordrecht), 39

Yee, H.C.K., & Green, R.F. 1987, ApJ, **319**, 28